

John J. Berlin
John Berlin
305
Ridge Road
Austin, Texas 78746

FFA

FLYGTEKNISKA FÖRSÖKSANSTALTEN

THE AERONAUTICAL RESEARCH INSTITUTE OF SWEDEN

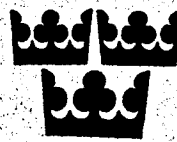
MEDDELANDE 115

REPORT 115

ANOMALOUS HEAT TRANSFER AND PRESSURE DISTRIBUTIONS ON BLUNT BODIES AT HYPERSONIC SPEEDS IN THE PRESENCE OF AN IMPINGING SHOCK

BY

Barry Edney



STOCKHOLM 1968

FLYGTEKNISKA FÖRSÖKSANSTALTEN
THE AERONAUTICAL RESEARCH INSTITUTE OF SWEDEN

MEDDELANDE 115

REPORT 115

**ANOMALOUS HEAT TRANSFER AND PRESSURE DISTRIBUTIONS
ON BLUNT BODIES AT HYPERSONIC SPEEDS IN THE PRESENCE
OF AN IMPINGING SHOCK**

by

Barry Edney

SUMMARY

An extraneous shock impinging on a blunt body in hypersonic flow is observed to alter the flow around the body and increase both the local heat-transfer rate and pressure near the impingement point. Novel, quasi-static techniques are developed to study this phenomenon. Glass models, equipped with platinum thin-film thermometers, are injected into a hypersonic tunnel through a slot in a variable-incidence flat plate which generates the extraneous shock. Analogue networks provide graphs of the heat-transfer rates at various points on the model as a function of the model's position relative to the extraneous shock. Peaks in local heat-transfer rates upto 10 times the local, unperturbed, free-stream values are recorded as the model traverses the shock. A similar technique is used to measure the peak pressure.

The intense heating and high pressures are shown to occur over a narrow region where a disturbance, originating at the intersection of the bow shock and the impinging shock, meets the model surface. This disturbance may take the form of a free shear layer, a supersonic jet or a shock depending on the shape of the model and its position relative to the impinging shock. The exact form of this disturbance and the overall shock interference pattern may be predicted theoretically. Six different types of interference are shown to exist. The effect of varying the free-stream Mach number, the strength of the impinging shock and the ratio of specific heats on both the peak pressure and the peak heat-transfer rate are also accounted for, in excellent agreement with experiment.

Stockholm, February 1968

This investigation was sponsored by the Royal Swedish Air Force Board under contract INKS/Br 41748.

EINFLUSS EINES FREMDEN STOSSES AUF WÄRMEÜBERGANG
UND DRUCKVERTEILUNG AN STUMPFEN KÖRPERN IN
HYPERSCHALLSTRÖMUNG

von

Barry Edney

ZUSAMMENFASSUNG

Wenn ein fremder Stoss einen stumpfen Körper in Hyperschallströmung trifft, so beeinflusst er die Strömung und erhöht Wärmezufuhr und Druck in der Nähe des Auftreffpunktes. Mit einer neuen quasistationären Methode wurde diese Erscheinung untersucht. Glasmodelle die mit dünnen Platin-filmthermometern instrumentiert waren, wurden plötzlich in den Strahl eines Hyperschallkanals eingeschoben. Eine ebene Platte mit einem Anstellwinkel erzeugte den fremden Stoss. Die Wärmezufuhr wurde mit einer elektrischen Analogie aus der gemessenen Oberflächentemperatur bestimmt. Da sich das Modell relativ zum fremden Stoss bewegte, konnten in einem Versuch sämtliche Stosslagen durchgemessen werden. Die höchsten gemessenen Wärmezufuhren waren 10 mal grösser als die Werte ohne fremden Stoss. Mit einer ähnlichen Technik wurde auch die Druckverteilung gemessen.

Es wird gezeigt, dass die hohen Wärmezufuhren und Drücke dort auftreten, wo die Störung, die vom Schnittpunkt des fremden Stoßes mit der Bugwelle ausgeht, die Körperoberfläche trifft. Die Störung kann eine Wirbelschicht, ein Stoss oder ein Überschallstrahl sein. Ihre Art hängt von der Körperform und von der relativen Lage zwischen fremdem Stoss und Bugwelle ab. Die Form von Störung und Stosskonfiguration kann theoretisch vorausgesagt werden. Es wird gezeigt, dass 6 verschiedene Konfigurationen bestehen können. Der Einfluss der Machzahl, der Stärke des fremden Stoßes und des Verhältnisses der spezifischen Wärmes kann berücksichtigt werden. Die Übereinstimmung mit den Experimenten ist sehr gut.

TRANSMISSION DE CHALEUR ET DISTRIBUTION DE PRESSION
SUR UN CORPS OBTUS À DES VITESSES HYPERSONIQUES EN
PRÉSENCE D'UNE ONDE DE CHOC ÉTRANGÈRE

par

Barry Edney

RÉSUMÉ

Quand une onde de choc étrangère interfère avec un corps obtus dans un écoulement hypersonique, celle-ci influence l'écoulement et augmente la transmission de chaleur ainsi que la pression au voisinage de son point d'impact avec la surface du corps. Ce phénomène est étudié avec de nouvelles techniques quasistationnaires. On introduit brusquement dans un écoulement hypersonique des modèles en verre pourvus de thermomètres à fines lamelles de platine. Une plaque plane, avec un angle d'incidence, donne naissance à l'onde de choc étrangère. La transmission de chaleur a été déterminée à l'aide d'une analogie électrique en mesurant la température du corps en différents points de la surface du modèle. Vu que le modèle en verre se mouvait par rapport à l'onde de choc étrangère, il a été possible lors d'une seule expérience d'effectuer les mesures pour toutes les positions de l'onde de choc étrangère relativement au modèle. Les mesures de la plus grande transmission de chaleur donnèrent des valeurs dix fois supérieures à celles observées dans onde de choc étrangère. La répartition de la pression a été déterminée d'une manière analogue.

On a pu montrer que les hautes valeurs de la transmission de chaleur et les hautes pressions se trouvaient à l'endroit où la perturbation, provenant de la rencontre de l'onde de choc étrangère et de l'onde de choc propre au corps, touche la surface du corps. Cette perturbation peut être une couche de tourbillons, une onde de choc, ou un jet supersonique. Sa nature dépend de la forme du corps et de la position relative entre l'onde de choc étrangère et l'onde de choc propre au corps. La forme de la perturbation et la configuration du choc peuvent être déterminées par le calcul. On montre que six configurations différentes sont possibles. L'influence du nombre de Mach, de l'intensité de l'onde de choc étrangère ainsi que du rapport des chaleurs spécifiques peuvent être considérés. La concordance avec les expériences est très bonne.

CONTENTS

1. INTRODUCTION	5
2. REVIEW OF PREVIOUS SHOCK-IMPINGEMENT STUDIES	7
2.1. Experimental studies	7
2.2. Theoretical studies	11
3. DESCRIPTION OF THE TEST FACILITY	13
4. HEAT-TRANSFER RATE MEASUREMENTS	13
4.1. Description of technique	13
4.2. Experimental results	18
5. PRESSURE MEASUREMENTS	21
5.1. Measurements using conventional techniques	21
5.2. Measurements using quasi-static injection technique	23
6. PREDICTION OF INTERFERENCE PATTERNS	27
6.1. Heart diagram method	27
6.2. Numerical methods	38
7. PREDICTION OF PRESSURE VARIATIONS IN VICINITY OF SHOCK- IMPINGEMENT POINT	41
7.1. Types I, II and V interference. Shock/boundary-layer interactions	41
7.2. Type III interference. The attaching shear layer	43
7.3. Type IV interference. The supersonic impinging jet	45
8. PREDICTION OF HEAT-TRANSFER VARIATIONS IN VICINITY OF SHOCK- IMPINGEMENT POINT	48
8.1. Heating attributable to shock/boundary-layer interactions	48
8.2. Heating attributable to an attaching shear layer	53
8.3. Heating attributable to a supersonic impinging jet	60
9. SUPPLEMENTARY TESTS	63
9.1. Oil-spot flow visualization tests	63
9.2. Heat-transfer visualization tests	65
9.3. Tests in a hypersonic gun tunnel	66
10. CONCLUSIONS	66
ACKNOWLEDGEMENTS	69
SYMBOLS	69
APPENDIX	
Construction and calibration of thin-film gauges and analogue networks	70
REFERENCES	73
FIGURES 5.2, 5.3, 5.4, 5.5, 5.6, 5.9, 6.1, 6.2, 6.3, 6.4, 6.6, 6.8, 6.11, 6.14, 6.16, 6.18 and 8.12 .	77

ANOMALOUS HEAT TRANSFER AND PRESSURE DISTRIBUTIONS ON BLUNT BODIES AT HYPERSONIC SPEEDS IN THE PRESENCE OF AN IMPINGING SHOCK

by

Barry Edney

1. INTRODUCTION

In December, 1964, a series of experiments were carried out in FFA's Hyp 200 tunnel, at $M = 4.6$, to evaluate platinum thin-film gauges and associated analogue networks, which were designed to measure the stagnation-point heat transfer to a pyrex hemisphere [1]. To avoid damaging the model from overheating and to better approximate a step input in the heat-transfer rate, q , the cold model was injected directly into the hot core of the tunnel from behind a shield and splitter plate (Fig. 1.1). The resulting surface temperature and heat-

transfer record is shown in Fig. 1.2. It is seen that a reasonably good step input for q was achieved, except for a spike some 50 % above the steady level. Subsequent tests showed that this occurred as the model passed through a weak shock generated at the tip of the splitter plate (Fig. 1.3); the increased heating occurring over a very narrow region on the model, near the intersection of the bow shock ahead of the model and the extraneous shock from the splitter plate.

This was a surprising result. Firstly the extraneous shock was weak, and secondly

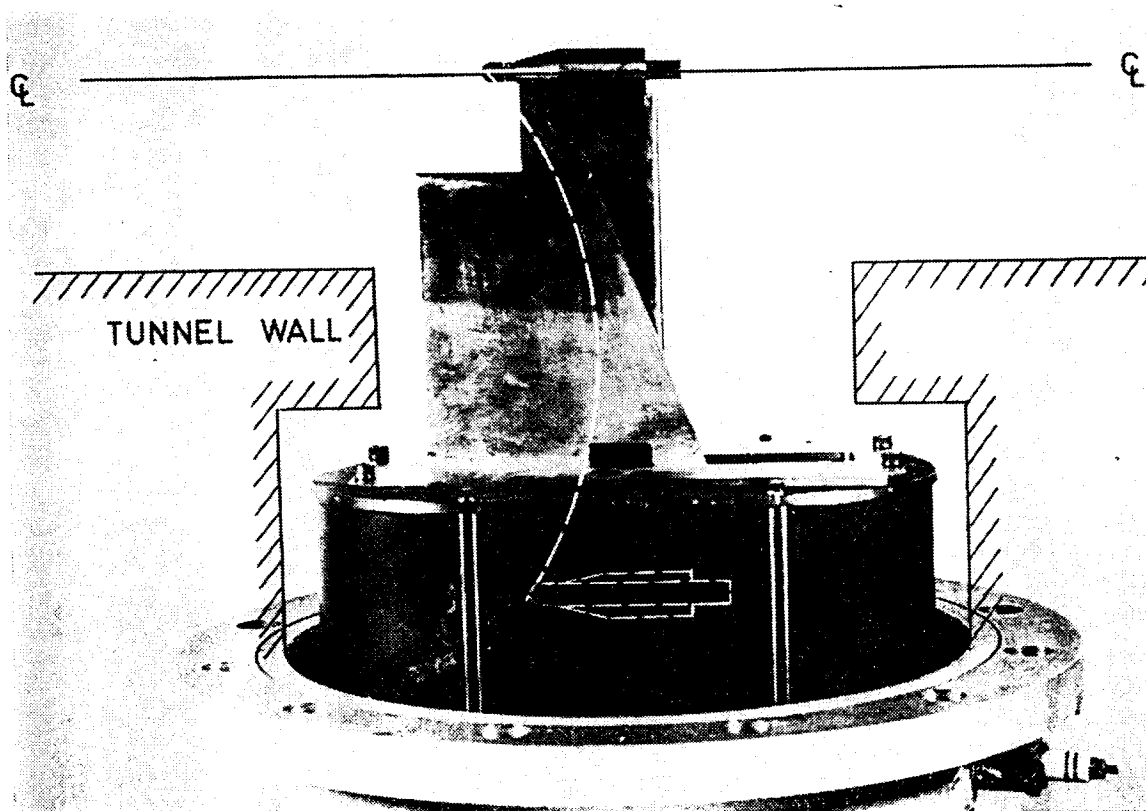


Fig. 1.1. Arrangement for injection of heat-transfer model showing shield, splitter plate and injection path.

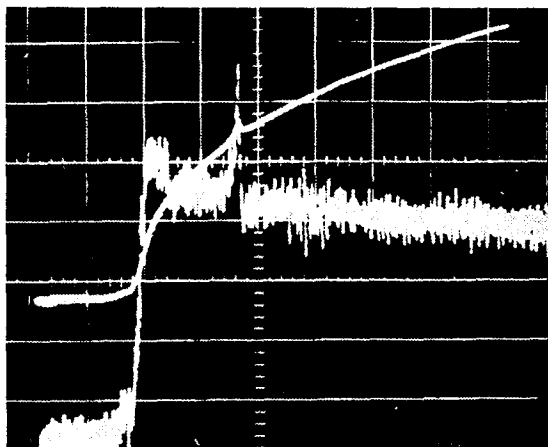


Fig. 1.2. Wall temperature (upper trace) and heat-transfer rate (lower trace) as model is injected into tunnel.

one might feel intuitively that the heat-transfer rate should be highest when the model is completely submerged in the shock layer on the splitter plate, on account of the higher pressure level there, decreasing monotonically to some steady level as the model passes through the shock into the free stream.

A literature search carried out at that time revealed no published work on the subject of shock impingement, which could explain this anomaly. Again, this is rather surprising since one can think of many examples of practical and immediate interest where an oblique shock impinges on a stronger, nearly normal shock. Some of these are illustrated in Fig. 1.4. Fig. 1.4 *a* represents a ram-jet inlet with the shocks impinging on the cowl lip, Fig. 1.4 *b* the bow shock produced by an aircraft fuselage



Fig. 1.3. Model passing through weak shock generated by splitter plate.

impinging on a wing or fin leading edge and Fig. 1.4 *c* the bow shock from the main body of a missile impinging on a side-strapped booster or fuel tank.

In view of the apparent absence of work in this field and yet its obvious practical significance, it was decided to carry out a study of the effects of shock impingement on axi-symmetric and 2-dimensional blunt bodies and blunt fins. Work started at FFA in January, 1965. About that time a copy of a report by Siler and Deskins [7] was obtained and this led to the discovery of the earlier work described in Refs. [2-6].

In April, 1965, advantage was taken of the ESRO-ELDO Documentation Service—a computer-based subject-searching service—to try and obtain further information on previous work relating to shock impingement. This proved fruitless—probably due to difficulties in programming the search—but underlined the paucity of published work on shock impingement at that time.

However, in the last two years, upto 1967, a number of reports [8-13] on shock impingement have appeared. All of these deal with tests involving shocks impinging on cylindrical fins. In addition, the work of Deveikis and Sawyer [14, 15] on the aerodynamics of tension shell shapes (possible shapes for reentry vehicles) should be mentioned since it is relevant to the problem of shock impingement. Fig. 1.5 shows the type of shock-interference pattern which can be produced by such shapes. We can formulate tension shell interference as a shock-impingement problem if we think of the nose shock impinging on the stronger shock generated by the skirt.

Finally, in October 1967, came the first in-flight confirmation of the severity of shock-impingement heating when the NASA X-15A-2 experimental rocket-driven aircraft suffered severe damage to its ventral fin, during a high-altitude flight at $M = 6.7$ [16]. The ventral fin, which supported a ram-jet test model (Fig. 1.6), was burned completely through in several places and the model tore loose. The extent of the damage is evident from Figs. 1.7 and 1.8. The

shock generated by the ram-jet model has burned gaping holes in the fin and removed four probes. It is interesting to compare this damage with that at the fin/fuselage junction, due to an interaction between the normal shock ahead of the fin and the boundary layer on the fuselage (Fig. 1.8). In the latter case only the ablative coating has been burned through.

Severe heating on the leading edges of the wings of the X-15A-2, due to the fuselage bow shock, and on the cockpit canopy, due to the shock from a pitot tube on the fuselage, was also evident. Fortunately, the ablative coating was sufficiently thick to prevent damage to the aircraft at these points.

The FFA study described in this report

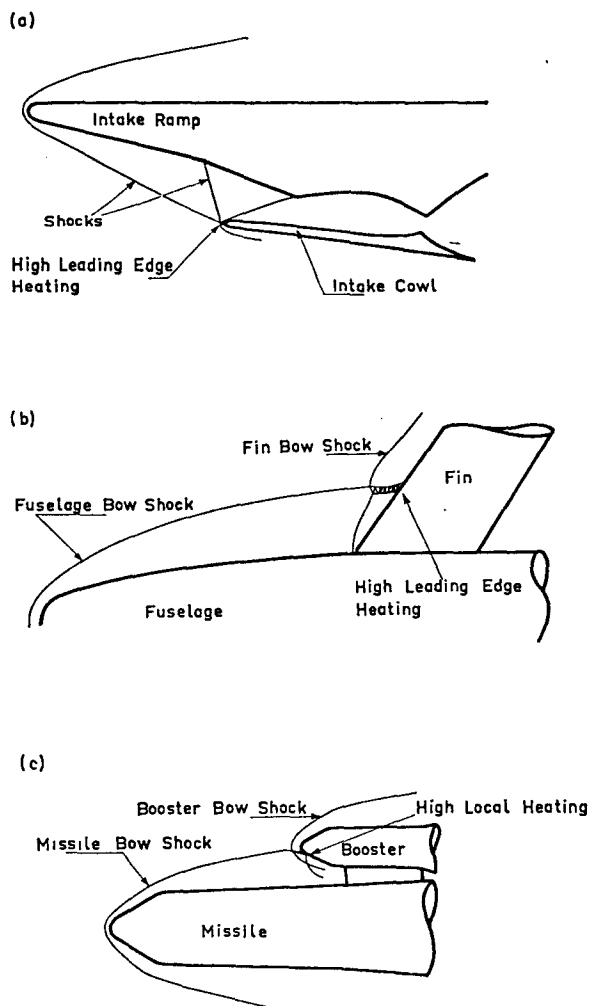


Fig. 1.4. Practical examples of shock impingement heating.

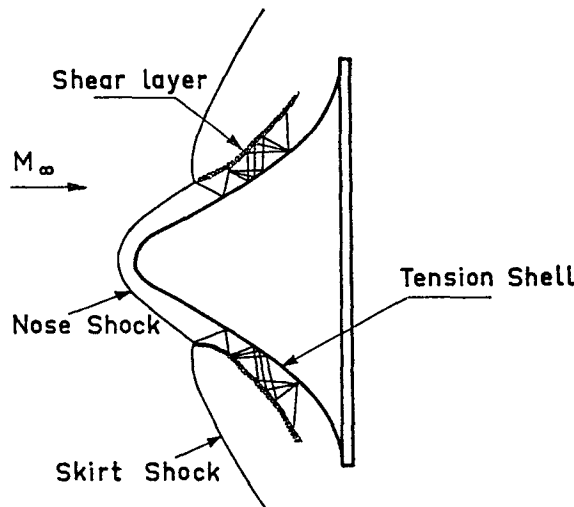


Fig. 1.5. Interference pattern produced by tension shell shape.

represents a fresh approach to the problem of shock impingement. Not only have novel experimental techniques been developed to study the very localized peak heating and pressure variations on the model, but also the way in which the problem has been tackled theoretically differs radically from that of other workers.

It is convenient to begin with a brief review of these previous shock-impingement studies.

2. REVIEW OF PREVIOUS SHOCK IMPINGEMENT STUDIES

2.1. Experimental studies

Previous experimental studies were confined almost exclusively to wedge/cylindrical-fin configurations. The only exceptions were Carter & Carr [3] and Francis [4, 10]. Carter and Carr carried out free-flight tests with a 'hammer-head' model mounted on a rocket test vehicle. The extraneous shock in this case was generated by a hemisphere-cylinder forebody and impinged on cylindrical fins which were unswept. In addition to measurements on a wedge/cylindrical-fin combination, Francis made tests on wedge-shaped fins as well as tests using a conical shock generator instead of a wedge.

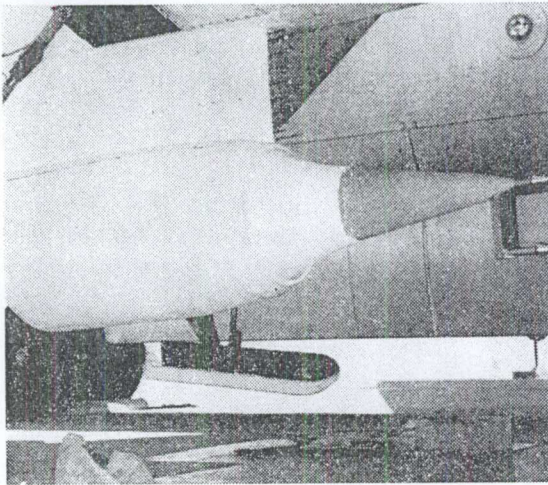


Fig. 1.6. Ram jet model mounted on ventral fin of X-15A-2 aircraft prior to test flight. (Photo courtesy of NASA.)

A typical model and the possible flow around it is sketched in Fig. 2.1.

The experiments of Newlander [2] are least like the rest since the wedge and cylinder were mounted on a large, flat plate. In one case the whole of the wedge and a large part of the cylinder were immersed in the boundary layer on the plate. The result was that the shock generated by the wedge did not impinge on the cylinder but passed

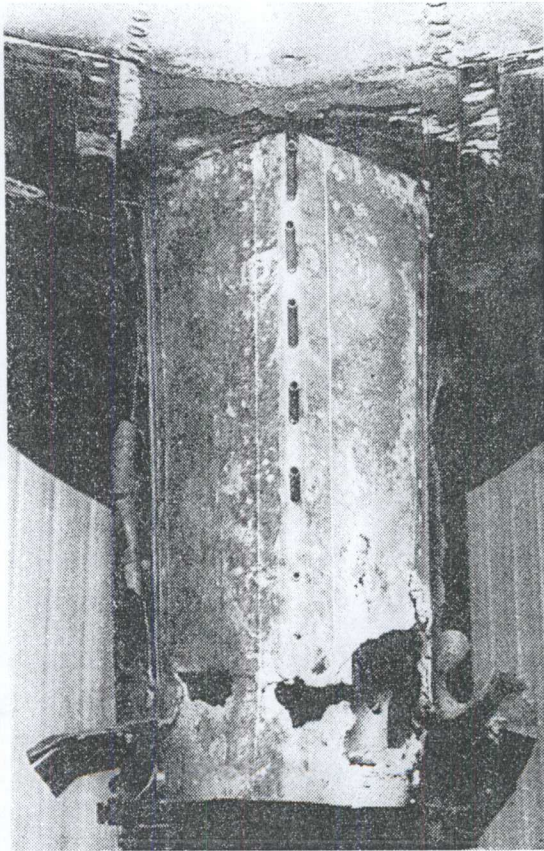


Fig. 1.8. Front view of ventral fin showing damage due to shock impingement. (Photo courtesy of NASA.)

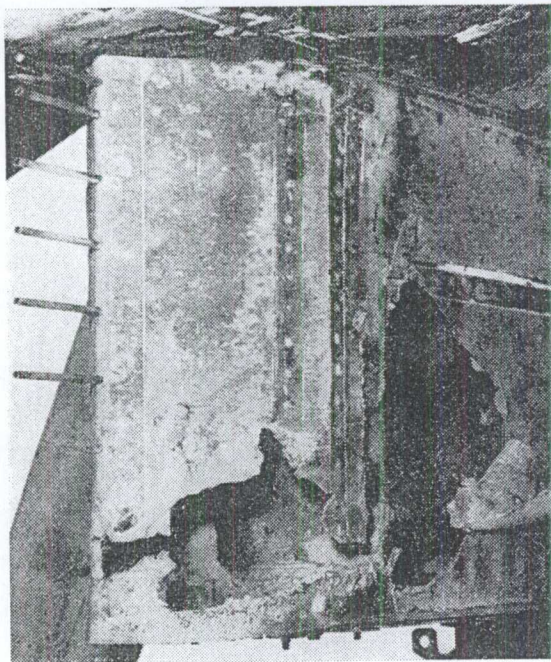


Fig. 1.7. Side view of ventral fin showing damage due to shock impingement. (Photo courtesy of NASA.)

outboard of it. Consequently, the title is rather misleading and the results should be approached with caution.

Taken together, these various experiments cover a wide range of Mach numbers, from 2 to 19. In addition, the experiments were carried out in a variety of tunnels, including a shock tunnel [13], and an arc-driven tunnel [7, 11]. There was even one free-flight test [3].

Since most of the investigators expected boundary-layer transition near the impingement point to be the most probable cause of increased heating, they have focussed their attention almost exclusively on the Reynolds number. This varied from 8×10^3 per inch to 3.6×10^6 per inch.

Real gas effects—in particular the variation of γ —can be expected to have a very large influence on the peak pressure and hence the peak heating near the impingement point,

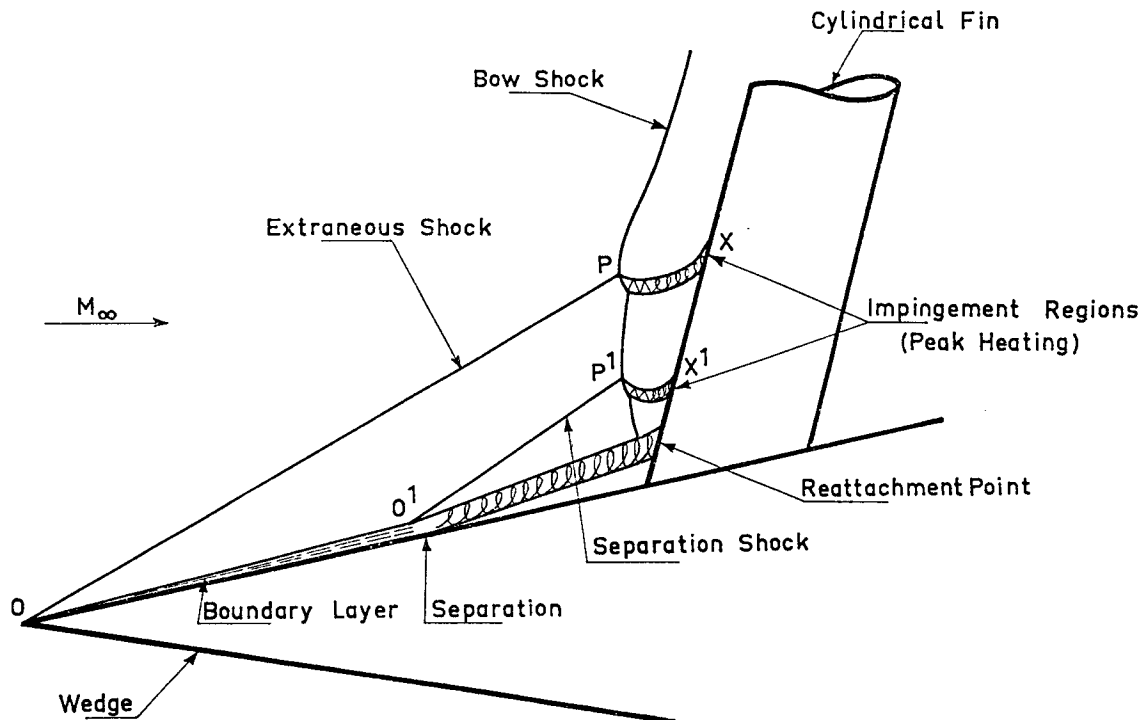


Fig. 2.1. A typical wedge/fin model and the flow pattern set up.

as we shall see later. However, it is probable that only the shock-tunnel experiments of Hiers & Loubsky [13] would be of any significance in this respect. Certainly none of the investigators mentions the importance of simulating real gas effects.

The accompanying table represents a summary of the operating conditions for each test and the measurements carried out. In most cases the wedge angle ξ and the fin sweep angle Λ could be varied independently, but the choice of angles appears to have been quite arbitrary. One investigator, Jones [6], even examined the effects of yaw.

Pressure taps and thermocouples were placed at regular intervals, Δx , along the leading edge of the fin. The ratio $\Delta x/d$, where d is the diameter of the leading edge, varied from $\frac{1}{6}$ [13] to 2 [5]. This is an important parameter since it determines how well the peak heating may be resolved. Fig. 10 of Ref. [13] shows an extraordinary photograph—in colour—of a fin after one run in the NASA Ames combustion driven shock tunnel. Burn marks about $\frac{1}{16}$ of the leading edge diameter illustrate how loca-

lized the peak heating can be. We conclude, therefore, that only Hiers & Loubsky, who had the smallest $\Delta x/d = \frac{1}{6}$, measured anywhere near the true peak heating.

Reduction of data to arrive at heat-transfer rates from thermocouple outputs followed the simple equation

$$q = \rho c a \frac{dT}{dt} \quad (2.1)$$

ignoring corrections for cross conduction in the model skin,

where q = heat-transfer rate

ρ = density of skin material

c = specific heat of skin material

T = skin temperature

t = time

Only Hiers & Loubsky [13] consider how accurately their measured values represent the true aerodynamic heating, taking into account the finite spacing of the thermocouples and the finite thickness of the model skin. By dividing the skin into a lattice and assuming an aerodynamic heating input of the form

TABLE 1. Summary of experiments by other workers

Ref.	M_∞	$(Re_\infty/\text{in}) \times 10^{-6}$	d''	ξ°	Λ°	p	q	$\Delta x''$	Schl. Oil	q_{\max}/q_{20}	Remarks
[2]	2.65 3.51 4.44	0.11–0.38	2.8	16.25	0			×	0.25– 1.0	1.8 2.0 3.1	Wedge & fin mounted on flat plate. Partially immersed in boundary layer
[3]	2.0 2.65 4.44		0.75	†	0				×		† Not applicable. Shock generated by hemisphere/cylinder forebody
[3]	2.53– 5.5	1.33–2.5	0.75	†	0		×	0.15		0.1–0.5 ($M < 3$) 1.5–2 ($M > 4$)	Free flight to 10,500 ft. altitude
[4, 10]	9	0.0145–0.096	1.0	6.34* ± 20	0 ± 20		×	0.25	×	1–4	*Cone & wedge with one cylindrical and one wedge fin, both fixed
[5]	4.15	1.44–3.6	1.115	0 8	20 20 & 60	×	×	2.0*	×	2.5	* Variable location. Fin could be slid in and out relative to wedge.
[6]	6	0.06–0.73	1.06	0	60	×*	×	1.0	×	1–3	* Only at $Re_\infty = 0.73 \times 10^6$. Model yawed upto 30°.
[7]	19	0.024	2.0	0–40	0–60	×	×	0.5	×	2.5–5	
[9]	6 8* 10	0.048–0.30	2.0	0–60	0–60	×	×	0.5	×	2.5–5	* Data not presented for $M_\infty = 8$
[11]	19	0.025	2.0	0–40	0–50	×	×	0.5	×	2–6	
[12]	8	0.077–0.087	1.0	12	45 & 60	×	×	0.25	×	3–5	
[13]	14	0.008	1.0	0–15	0.22 ₁ 45		×	0.15	×	10	Luminous photos supplement schlieren photos

 d = diameter of fin leading edge ξ = flow deflection on wedge Λ = fin sweep angle p = pressure measurement q = heat transfer measurement Δx = thermocouple spacing

Schl. = Schlieren photography

Oil = Oil flow visualization

$$q(x) = 0.332 \frac{\mu_{av}}{\sigma_{av}^{\frac{1}{2}}} \frac{Re^{\frac{1}{2}}}{x^{\frac{1}{2}}} (h_0 - h_w) \quad (2.2)$$

where x = distance from impingement point

μ_{av} = viscosity averaged over boundary layer

σ_{av} = Prandtl number averaged over boundary layer

Re = Reynolds number per cm

h_0 = reservoir specific enthalpy

h_w = specific enthalpy at wall,

they calculate the heating rate that would be measured by the thermocouples on the inner surface of the skin. This rate is then compared with the experimentally observed

rate and is shown to be in quite good agreement. However, they do not examine the effects of truncating the theoretically infinite heating at $x = 0$, since, although large, it must be finite. Consequently, since theirs is essentially an inverse method, we do not know how much we can alter the shape of the input without producing any appreciable change in the heating measured on the inner surface.

The values of q_{\max}/q_{20} , where q_{20} is the value in the absence of the shock, which were obtained by the various investigators are presented in the table. However, it is fairly certain that these measurements underestimate the maximum aerodynamic heating.

It is difficult to draw any conclusions regarding the effect of Mach number or strength of the impinging shock on the peak heating from these results. However, the effects of fin sweep angle, Λ , emerge fairly clearly. Ray & Palko [9] show that the peak heating is severest for unswept fins, decreasing monotonically as Λ increases.

As is evident from the table, nearly everyone took schlieren pictures. For the sake of coherence we shall postpone discussion of these in detail until Chapter 6 when we have established what one might be expected to see. Although boundary-layer separation ahead of the fin/wedge junction is clearly visible on many of the photographs, the effect of its subsequent reattachment in creating a local hot spot on the fin is often ignored when discussing the results. Consequently, heating attributed to shock impingement in some cases may in fact have been caused by boundary-layer separation instead. The difficulty of separating these two effects is readily apparent from Fig. 2.1. None of the investigators indicates the reattachment point on their graphs and few the shock impingement point. An exception to this criticism, however, is Beckwith [5], who observes the effect of separation for $\Lambda = 20^\circ$ and notes that at $\Lambda = 60^\circ$, when there was no separation on the wedge, the boundary layer on the fin was turbulent and that this accounted for the increased heating.

2.2. Theoretical studies

2.2.1. The acoustic disturbance model. The first piece of theoretical work to appear in the open literature was that of Fontenot [8], in which he attempts to predict the width of the zone of increased heating on a swept fin. Fontenot postulates that the disturbance created by the interaction of the extraneous shock and the bow shock can be treated as an acoustic-like disturbance. This disturbance propagates into the region behind the bow shock as a spherical wave at the local acoustic velocity. Fontenot obtains expressions for x_{out} and x_{in} , the outboard and in-

board limits of the zone of increased heating, of the form

$$x/\delta = -\frac{D}{KE} \left[\ln \left(\tanh \frac{E}{2} \right) \right] \times \left[\frac{(T_2/T_\infty)^{\frac{1}{2}} \pm M_\infty \sin \Lambda}{M_\infty \cos \Lambda} \right] \quad (2.3)$$

where the plus sign gives x_{out} and the minus sign x_{in} , and

$$\begin{aligned} \delta &= \text{shock stand-off distance} \\ \Lambda &= \text{fin sweep angle} \\ T_2/T_\infty &= \text{temperature ratio across the bow shock} \\ M_\infty &= \text{free-stream Mach number} \\ K &= 2 \rho_\infty / (\rho_2 + \rho_{20}) \quad (2.4) \\ D &= 1 - K / \{K(2 - K)\}^{\frac{1}{2}} \quad (2.5) \\ \text{and } E &= \sinh^{-1} D \quad (2.6) \end{aligned}$$

For $\Lambda = 30^\circ$, the width of the zone, $(x_{\text{in}} + x_{\text{out}})$, turns out to be the order of one leading edge diameter for a wide range of M_∞ . Unfortunately, this is at variance with experiment, the width of the zone being $0.1 d$ or less. However, the failure of Fontenot's theory should not come as any surprise! The physical model is clearly unrealistic, as we shall see in Chapter 6. For $\Lambda = 30^\circ$ the disturbance from the impingement point propagates, not as a spherical wave, but as a shock and the width of the zone of increased heating depends on the interaction between the shock and the boundary layer on the fin. This will vary with the strength of the impinging shock, not accounted for by Fontenot's theory. Finally Fontenot, pointing the way for refinements of his theory, states that at very high altitudes a correction for the finite thickness of the impinging shock should be applied. Certainly this is true, but in view of the inherent deficiencies of the acoustic disturbance model such a correction would be of doubtful value.

2.2.2. The shock-induced vorticity model. This method leads to correlations between the peak heating—normalized with respect to either the heating outboard or inboard of the impingement point—and the pressure ratio across the jet (or region of high vorticity,

as Francis called it) originating at the impingement point. The approach is, strictly speaking, an empirical one and was first proposed by Francis in 1962 [4] but did not appear in the open literature until 1965 [10].

By drawing an analogy between shock-generated vorticity at low Reynolds numbers and the vorticity generated at the impingement point in the present case, Francis makes use of an earlier result obtained by Hoshizaki [17], who derived an approximate solution, in closed form, for the effect of shock-generated vorticity on three-dimensional stagnation heating in terms of quantities evaluated at the wall and immediately behind the shock wave. This has the form

$$Nu_\xi \approx Nu_0 [1 - r_s \zeta_s / r_w \zeta_w]^{-1} \quad (2.7)$$

where Nu = Nusselt number

r = radius of curvature

ζ = vorticity

and the suffixes

ξ = with vorticity

0 = without vorticity

s = at the shock

w = at the wall.

Further, calculations of vorticity profiles in the shock layer indicate that as ζ_s becomes arbitrarily large, ζ_w is not only very large but proportional to ζ_s so that the ratio Nu_ξ/Nu_0 is approximately constant. An order of magnitude calculation gives $Nu_\xi/Nu_0 \approx 5$. Starting from Crocco's theorem for vorticity, viz.

$$\zeta = [T/u] [dS/dn] \quad (2.8)$$

where T = temperature

u = velocity

dS/dn = entropy gradient normal to streamline

and using some simplifying assumptions Francis arrives at the result

$$\zeta \sim \ln(P_{t_i}/P_{t_o}) \quad (2.9)$$

where P_{t_i} and P_{t_o} are the total pressures inboard and outboard of the jet. This suggests a correlation between q_ξ/q_0 and $\ln(P_{t_i}/P_{t_o})$. A best straight-line fit through

experimental data obtained by Francis and supplemented by the experimental data obtained by Newlander [2] has the form

$$\frac{q_\xi}{q_0} = 1 + 2 \ln\left(\frac{P_{t_i}}{P_{t_o}}\right). \quad (2.10)$$

The scatter about this line is large, however, and reflects, no doubt, the difficulty of locating the peak heating along the fin leading edge. Thus any measurement we carry out will underestimate q_ξ/q_0 for a given P_{t_i}/P_{t_o} , to a greater or lesser degree. This in turn suggests that not only would the scatter be reduced but that the whole body of data would be displaced towards larger values of q_ξ/q_0 , if really accurate localized measurements were feasible.

Francis also presents a plot of q_ξ/q_i versus $\ln(P_{t_i}/P_{t_o})$. This shows q_ξ/q_i to be approximately constant, where the average scatter is within the range

$$1.4 < q_\xi/q_i < 2.0. \quad (2.11)$$

Finally we note that the limiting value for $Nu_\xi/Nu_0 \sim 5$, mentioned above, is exceeded in practice by at least a factor of two. In addition, experiments at FFA demonstrate that by varying the position of the impingement point relative to the fin, q_ξ/q_0 can be made to vary without varying P_{t_i}/P_{t_o} .

Although this model gives a poor correlation of experimental data, some of the basic ideas are sound and might possibly be developed to account for the increased heating due to a fully turbulent jet as opposed to a laminar jet. The jet referred to here is that originating at the impingement point, which we shall describe in Chapter 6.

2.2.3. The divided flow model. This is the model proposed by Hiers and Loubsky [13] and is shown in Fig. 2.2. We shall show later in Chapter 6 that there are a number of discrepancies in this model, but nevertheless the essential feature, namely the upward and downward deflected flows on either side of the vortex sheet, is correct and hence the treatment that follows is not invalidated on that account.

What, then, they do is to assume that the

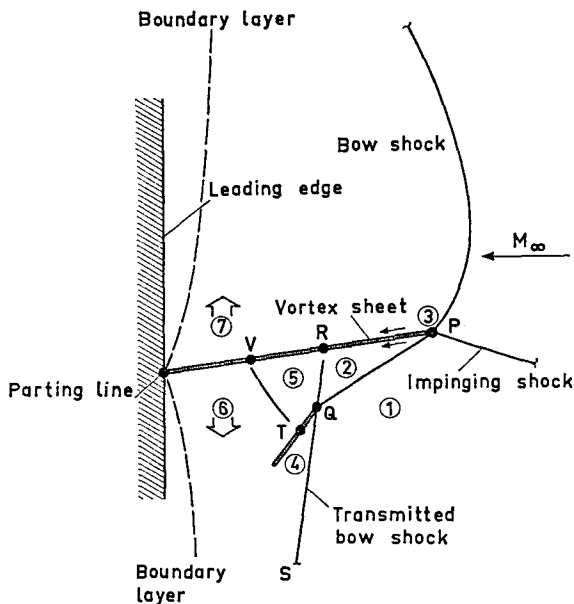


Fig. 2.2. Hiers & Loubsky's model for shock impingement (Ref. [13]).

boundary layer on either side of the attachment point is the same as that on a flat plate with its leading edge at the attachment point and free-stream conditions corresponding to the conditions in regions 6 and 7. The heat-transfer rate is then of the form

$$q(x) = 0.332 \frac{\mu_{av}}{\sigma_{av}^{\frac{1}{2}}} \frac{Re^{\frac{1}{2}}}{x^{\frac{1}{2}}} (h_0 - h_w) \quad (2.2)$$

Its weakness lies in that it assumes zero boundary-layer thickness at the attachment point and, consequently, it always predicts an infinite heat-transfer rate at that point—even for a vanishingly weak impinging shock! Although such an assumption is shown to be a reasonable approximation for the heat transfer at some distance from the attachment point, it is clearly untenable when we are attempting to predict the heat-transfer rate right at the attachment point.

Nevertheless, this approach does have some merit and could provide an outer solution in a more sophisticated model. The inner solution could probably be obtained by appealing to the analogy between the subsonic region at the impact point of a supersonic jet and that ahead of a supersonic blunt body of the same width as the jet.

3. DESCRIPTION OF THE TEST FACILITY

All tests were carried out in the FFA small hypersonic tunnel Hyp 200. This tunnel has a test-section diameter of 20 cm and may be operated at $M = 4.6$ or 7 by means of interchangeable, axisymmetric nozzles. The maximum tunnel stagnation temperature is 350°C and the maximum stagnation pressure 17 atm. Both the stagnation temperature and pressure can be accurately measured to within $\frac{1}{2}\%$. Temperatures can be held within $\pm 5^\circ\text{C}$ from run to run and the pressure to within $\pm \frac{1}{2}\%$. This means that very good repeatability can be obtained when carrying out heat-transfer studies. Reynolds numbers can be varied from $4.05 \times 10^4/\text{cm}$ to $4.75 \times 10^5/\text{cm}$ at $M = 4.6$ and from $1.11 \times 10^4/\text{cm}$ to $7.65 \times 10^4/\text{cm}$ at $M = 7$.

The test flow is also clean, which is of importance when using thin-film gauges, since these are easily eroded by dust particles, giving erroneous readings.

The tunnel is equipped with a pneumatically operated model injection device specifically designed for heat-transfer tests and a high quality schlieren system.

4. HEAT-TRANSFER RATE MEASUREMENTS

4.1. Description of technique

The prime objective of the present tests was to study the variation of the heat-transfer distribution around the model, as its position relative to the impinging shock was varied. In other words, what was wanted was a plot of the heat-transfer rate $q(x/r)$ at some point x on the model as a function of y , the height of the model above or below the shock.

If calorimeter gauges are used this entails making a large number of runs at different heights of the model above the plate generating the shock. Thus, in preliminary tests using a hemispherical-shell calorimeter model about 10 runs were necessary for a given

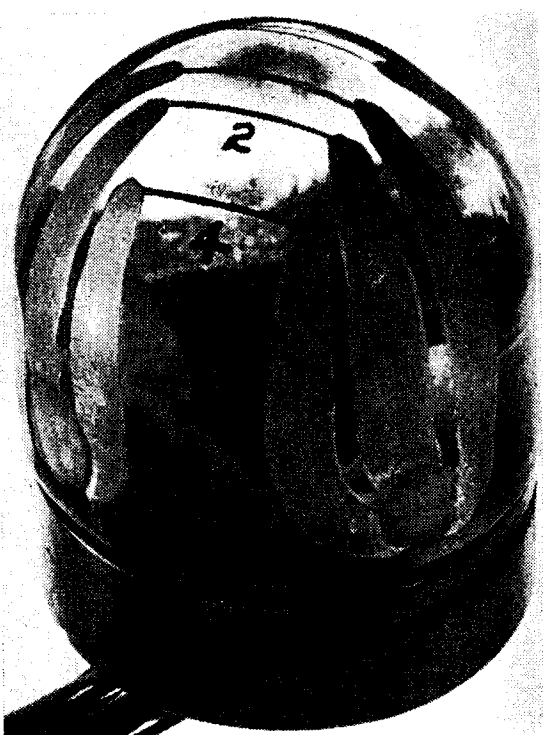


Fig. 4.1. A typical glass model equipped with thin-film gauges.

plate angle and Mach number. This was both time consuming and costly, involving numerical data reduction which could only be performed on a computer. Even so, the spatial resolution, because of the relatively large sensing area of the thermocouple, and the accuracy, because of the difficulties in allowing for conduction losses and variations in the model temperature, T_w , were far from optimum. This is always a problem when the heat input around the model is highly non-uniform, and one not satisfactorily overcome by previous investigators.

A significant departure from conventional methods of calorimetry was evidently called for. This was accomplished by the use of solid glass models equipped with platinum thin-film gauges. Such gauges find a wide application in shock tunnels and similar short-duration facilities but have not been used in continuous tunnels hitherto. Used in conjunction with analogue networks these give essentially instantaneous readout of surface temperature, T_w , and heat-transfer

rate, q — even if this varies rapidly with time.

Three basic models were tested. These were:

- a. 30 mm diameter hemisphere/cylinder.
- b. 30 mm diameter flat-faced cylinder.
- c. 30 mm diameter blunted cone/cylinder. 5 mm nose radius. 30° half angle.

Fig. 4.1 shows the hemispherical model.

Six platinum thin-film gauges approximately 0.4 mm wide were drawn on each model at roughly equal intervals of x/r from the stagnation point. By rotating a model, measurements at 11 different points could be made—the stagnation-point measurement on the axis of the model being repeated. Measurements were made along the centre line of each model with the thin films parallel to the intersection of the impinging shock and the bow shock ahead of the model, i.e. parallel to the leading edge of the shock generator.

T -section analogue networks, similar to the type developed by Meyer [18], were used to reduce surface temperatures to heat-transfer rates directly. A suitable compromise between response time (100 μ sec), testing time (100 msec) and signal level (~ 1 mV), allowing the output to be recorded directly on a Tektronix 502a oscilloscope, without preamplification, was achieved.

The construction and calibration of both the models and the analogue networks is described in the appendix.

The models were injected into the test

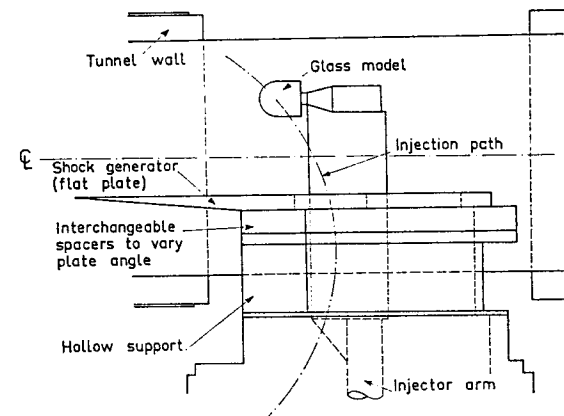


Fig. 4.2. Experimental arrangement for injection of glass models.

section through a hollow sting supporting the shock generator (a flat plate 98 mm wide and upto 350 mm long). The incidence of the shock generator could be set at -3° , 0° , 5° , 10° and 15° by means of interchangeable sting sections. This arrangement is shown in Figs. 4.2 and 4.3.

At $+10^\circ$ and $+15^\circ$, shorter plates together with other modifications to get the tunnel to start were necessary. These are shown in Figs. 4.4 and 4.5. The $+15^\circ$ tests were only possible at $M = 4.6$, however.

It should also be mentioned that the tunnel would start with the model retracted and continue to run when the model was injected, whereas it was often impossible to start the tunnel with the model in the test section from the beginning. Advantage was taken of this fact to make models larger than would otherwise have been possible. The long plates were necessary to make the distance between the shock and the boundary layer as large as possible. A separation

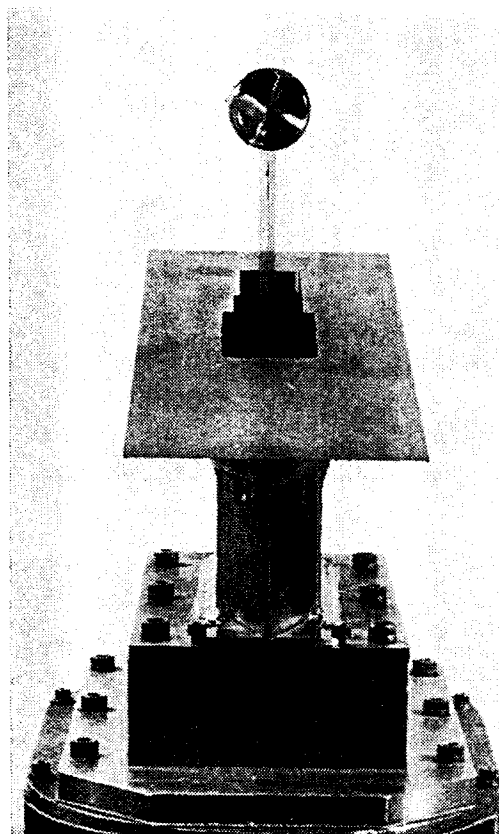


Fig. 4.3. Glass model in raised position. Front view.

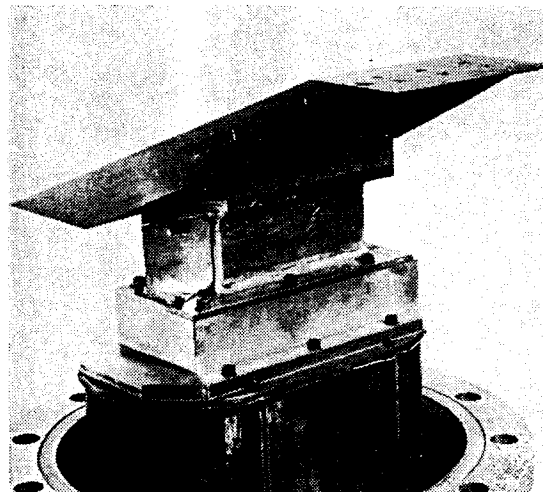


Fig. 4.4. Shorter plate and afterbody "fix" for $\xi = 10^\circ$.

greater than one model diameter was aimed for.

As a check on the flow along the plate an oil-drop visualization technique was employed. Fig. 4.6 shows the result of these tests. It is seen that the flow appears sensibly two-dimensional over 80 % of the width of the plate ahead of the slot.

Using thin-film techniques we may make a complete traverse of the shock layer on the plate, continuing through the shock into the undisturbed free stream, during a single run. Furthermore, if the speed of the traverse, V , is constant, a plot of q as a function of time, t , is equivalent to a plot of q as a function of distance, y . Thus, all we need to do is to record the output of the analogue network, which is directly proportional to q , on an oscilloscope, choosing a suitable

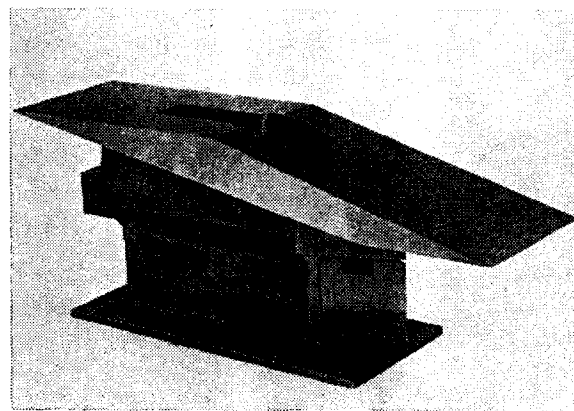


Fig. 4.5. Double wedge for $\xi = 15^\circ$.

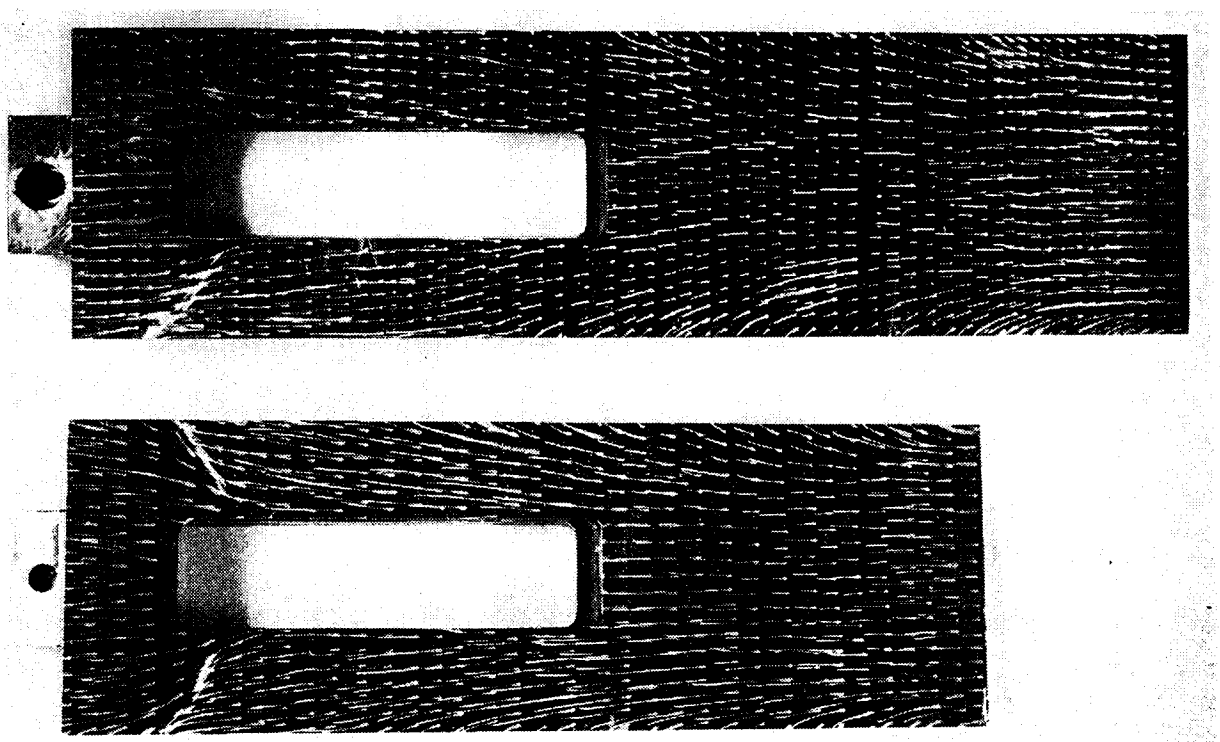


Fig. 4.6. Oil flow patterns on shock generators. $\xi = 5^\circ$ (upper) and $\xi = 10^\circ$ (lower). $M = 4.6$. Model raised.

sweep rate, and we have the graph we require less than a minute after making the run. Fig. 4.7 shows typical oscilloscope records obtained using this technique. We shall discuss these records in detail later.

There are several distinct advantages in making the traverse as quickly as possible (total time 1 sec or less), namely:

- Nearly the whole of the available running time (2–5 min) may be allocated to fine adjustment of P_0 and T_0 to the exact levels desired.
- Heat losses due to radiation and conduction can be ignored since the model does not have time to warm up appreciably.
- Only small changes in P_0 , T_0 , T_w and hence T_w/T_0 and $(T_w - T_0)$ occur during the traverse.
- Corrections for variations in the temperature-dependent thermal properties of the glass can be ignored (see the appendix).

The choice of the injection speed and the design of the instrumentation is dependent upon the following considerations.

- To ensure quasi-static testing condi-

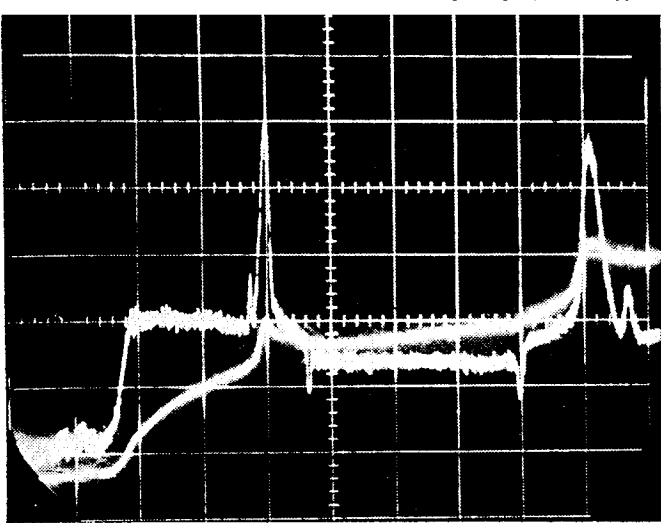
tions the injection speed, V , must be much less than the tunnel speed U , i.e.

$$V \ll U \quad (4.1)$$

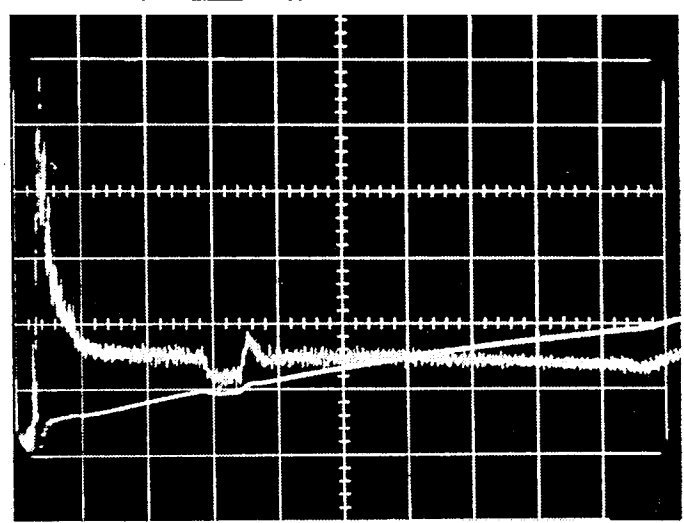
As an additional check that this condition had been met, ciné schlieren films were run at 80 f.p.s. to study the injection process. These showed that the model traversed the shock layer at constant speed (upto 2 m.sec^{-1}) and that the flow around the model under these conditions was identical with the flow around the model under steady state conditions. (At the end of its travel the injector bounces and the model may pass back through the shock again under certain circumstances. This partial traverse, at somewhat slower speed, although not intentional, affords us a number of cross checks on the measurements. The calibration of the injector is shown in Fig. 4.8.)

b. The width of the thin film, δ , and the response time of the analogue network, τ , must satisfy the condition

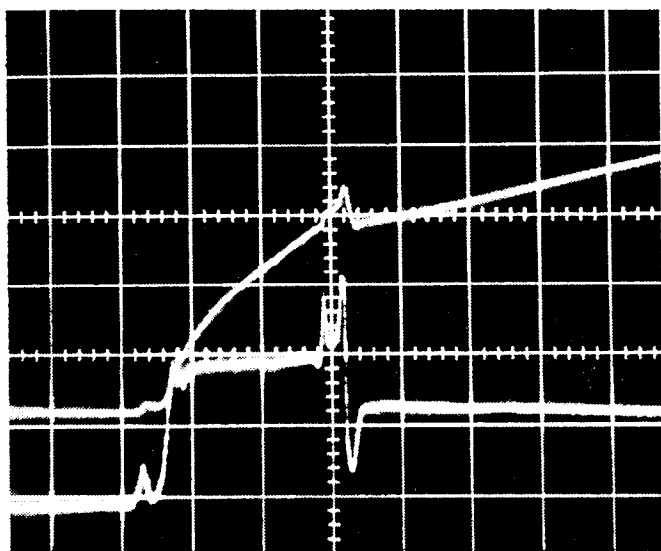
$$\tau < \delta/V \quad (4.2)$$



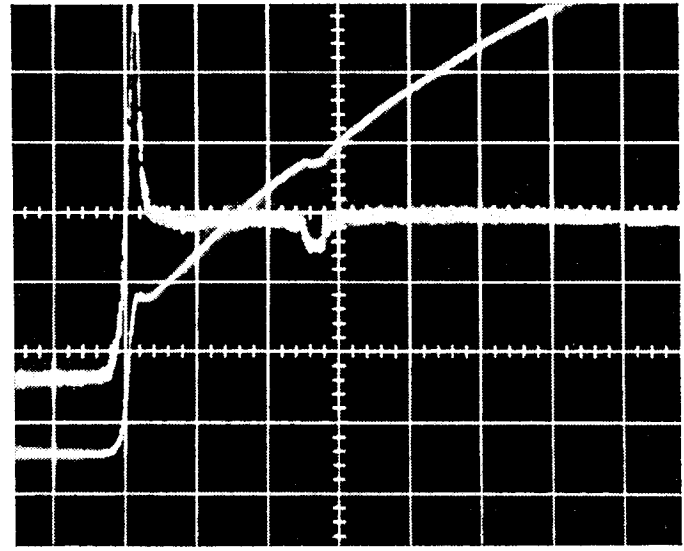
(a) Hemisphere $X/r = 0.965$
on underside



(b) Hemisphere $X/r = 0.965$
on upside



(c) Blunted Cone $X/r = 0.653$
on underside



(d) Blunted Cone $X/r = 0.653$
on upside

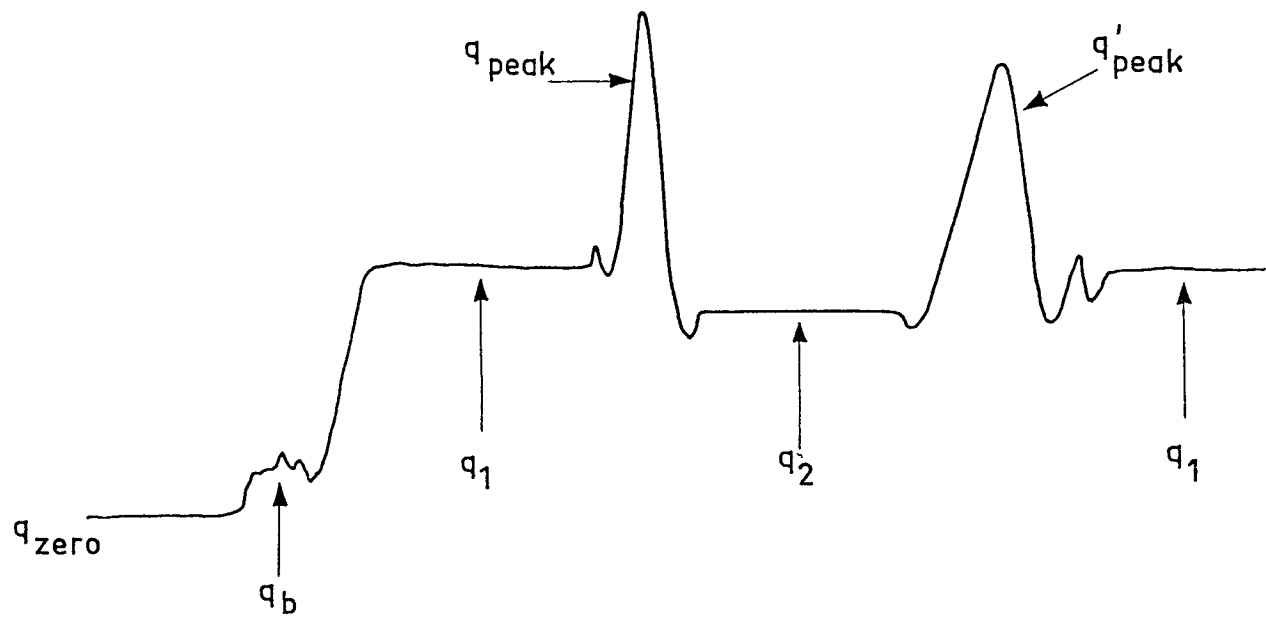


Fig. 4.7. Typical surface temperature and heat-transfer rate records. $M = 4.6$, $\xi = 5^\circ$.

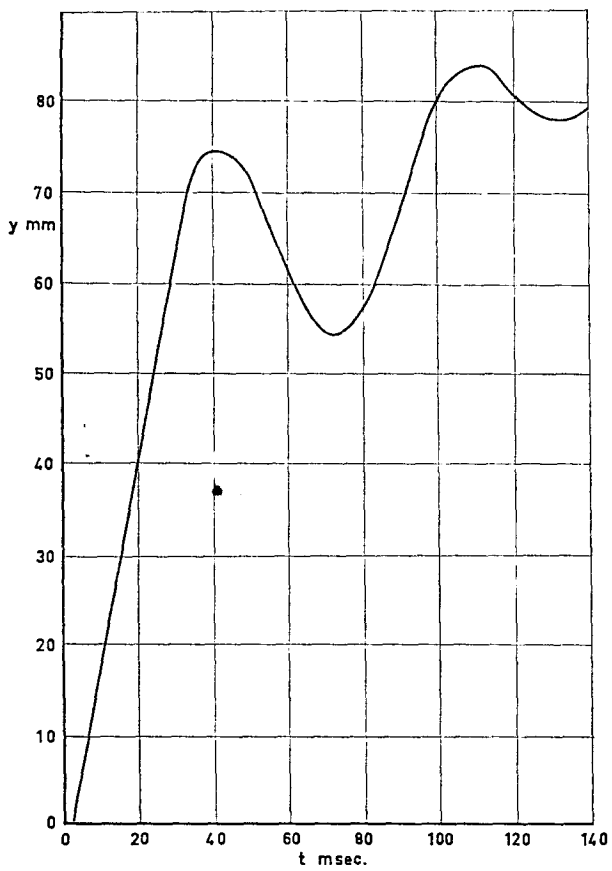


Fig. 4.8. Calibration of pneumatic injector showing bounce at end of travel.

c. The available analogue testing time t_R must satisfy the condition

$$t_R > y_{\max}/V \quad (4.3)$$

where y_{\max} is the total travel of the model beyond the plate, here about 100 mm.

d. The response time cannot be reduced without a sacrifice in signal level since

$$V_q \propto \tau^{\frac{1}{2}} \quad (4.4)$$

For $V = 2$ m.sec $^{-1}$ and $\delta = 0.4$ mm a suitable compromise was arrived at by taking $\tau = 100 \mu\text{sec}$ and $t_R = 100$ msec.

4.2. Experimental results

Tests were carried out at both $M = 4.6$ and 7 at plate angles $\xi = 0^\circ, 5^\circ$ and 10° . The 15° plate was run only at $M = 4.6$.

Fig. 4.7 showed typical records obtained at $M = 4.6$ with $\xi = 5^\circ$. The oscilloscopes were triggered when the model was about

5 mm under the level of the plate. Injection rates were 2 m.sec $^{-1}$.

The common features of these records may be summarized as follows.

1. Zero heat transfer as the model travels upwards inside the hollow sting supporting the shock generator.
2. A large, irregular spike, q_b , as the model passes through the boundary layer on the plate. Note that this is only recorded by gauges on the upper side of the model. This behaviour is consistent with the heating measured on protuberances in a hypersonic boundary layer (see for example Refs. [44, 45]).
3. A steady level, q_1 , as the model traverses the shock layer on the plate. The absolute heat-transfer rate measured at the local stagnation point on the hemisphere (about 6° below the axis of the model at this time) was found to be in reasonable agreement ($\pm 10\%$) with the theoretical stagnation-point heat-transfer rate predicted by Reshotko and Cohen [19], viz.

$$q_{10} = \frac{k_w(T_0 - T_w)}{\sqrt{v_w}} \left(\frac{Nu}{\sqrt{Re_w}} \right) \sqrt{C} \quad (4.5)$$

where $Nu/\sqrt{Re_w} = 0.64$ for $T_w/T_0 = 0.5$ and $\sigma = 0.7$ and

$$C = \frac{1}{r} \sqrt{\frac{2P_{10}}{q_{10}}} \quad (4.6)$$

Fig. 4.9 shows the distribution of q_1 as a function of x/r for the hemispherical model. The theoretical curve is the simplified expression derived by Werle [20], viz.

$$\begin{aligned} \frac{q(\bar{x})}{q_{10}} = & \left(\frac{\gamma}{\gamma-1} \right)^{\frac{1}{2}} \left[\bar{P}_{\infty} + (1-\bar{x})^2 \right] \\ & \times \left[\frac{1 - [\bar{P}_{\infty} + (1-\bar{x})^2]^{\frac{\gamma-1}{\gamma}}}{1 - (1-\bar{x})^2} \right]^{\frac{1}{\gamma}} \end{aligned} \quad (4.7)$$

where $\bar{x} = x/r$

\bar{P}_{∞} = inverse of pressure ratio across normal bow shock

γ = ratio of specific heats

q_{10} = heat-transfer rate at stagnation point.

4. A well defined peak, q_{peak} , as the model passes through the impinging shock. The height and width of this spike depend on the position on the model where the measurement was made. However, for measurements on the upperside of the model there is not always a distinct peak but more often a trough instead (Fig. 4.7 d). The trough is evidently due to a separation on the upperside of the model. Notice that the gauges are able to resolve even small secondary peaks and troughs (Fig. 4.7 a) near the primary peak. These, too, are of importance and will be explained later.

In Fig. 4.10 the ratio q_{peak}/q_{20} for the hemisphere has been plotted as a function of x/r for $M = 4.6$ and $\xi = 5^\circ$, 10° and 15° (q_{20} denotes the stagnation point heat transfer in the free stream). Fig. 4.11 shows a similar plot for $M = 7$ and $\xi = 5^\circ$. The similarity between the $M = 4.6$ and $M = 7$ distributions shown in Figs. 4.10 and 4.11 is striking. The peak heating is seen to be severest on the underside of the model, i.e. the side nearest the plate, reaching a maximum just below the axis of the model. Above this point there is a

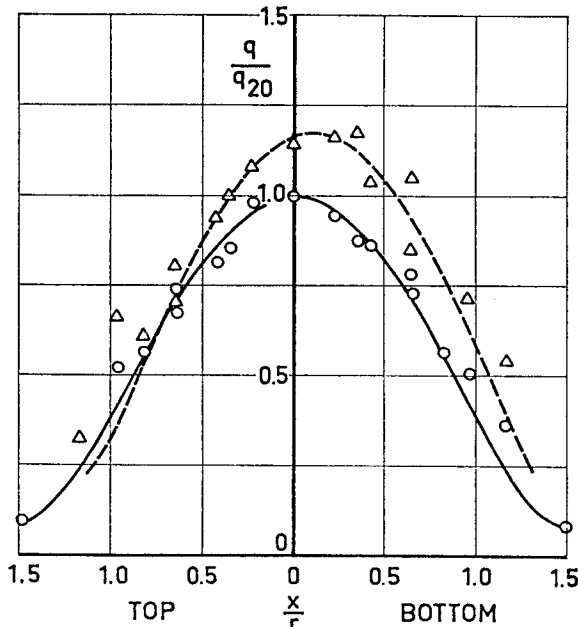


Fig. 4.9. Heat-transfer distribution around hemisphere. $M = 4.6$. $\xi = 5^\circ$. \circ q_2 experiment, — q_2 theory, \triangle q_1 experiment, --- q_1 theory.

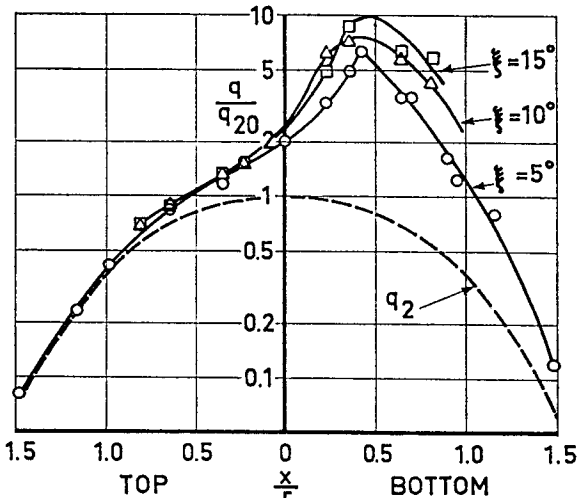


Fig. 4.10. Peak heating as a function of x/r for a hemisphere, showing effect of varying ξ . $M = 4.6$.

sharp fall-off in the intensity of the peak heating. Somewhat similar distributions were obtained with the flat-faced cylinder.* Note that the peak heating at a given point on the model increases with increasing plate angle, i.e. increasing strength of the impinging shock, and increasing Mach number.

Measurements on the blunted cone differ from those on the hemisphere and the flat-faced cylinder in one important respect. On the underside of the cone, away from the nose, two distinct peaks of comparable size are recorded close together (Fig. 4.7 c). These are due to two different types of shock interference being set up in quick succession. (We shall see examples of this when we discuss the pressure measurements in Chapter 5.) Fig. 4.12 shows q_1 , q_2 and q_{peak} for the blunted cone at $M = 4.6$ and $\xi = 5^\circ$. The variation of q_{peak} near the nose is similar to that on the hemisphere. However, on the conical part of the model, on the underside, two peaks appear, both of which are plotted in Fig. 4.12. Fig. 4.13 shows how the second of these peaks also increases with ξ .

* These measurements were incomplete due to damage to three gauges. A separation on the plate upstream of the model at $\xi = 10^\circ$ also made data reduction uncertain. Consequently, these results are not presented.

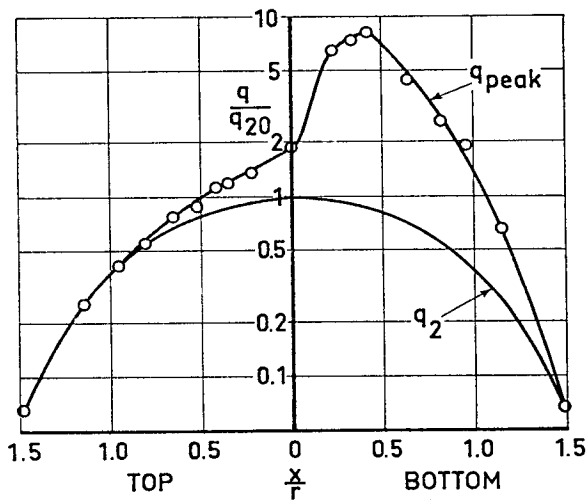


Fig. 4.11. Peak heating as a function of x/r for a hemisphere. $M = 7$. $\xi = 5^\circ$.

5. A second steady level, q_2 , as the model passes into the free stream. Note that q_2 is slightly lower than q_1 (except for large x/r on the upper side of the model) on account of the lower pressure level behind the bow shock on the model compared to when it is submerged in the shock

layer on the plate. Measurements of q_2 as a function of x/r for the hemisphere are also compared with the theoretical distribution in Fig. 4.9. The discrepancy between the measured and predicted stagnation-point heat-transfer rate is about 5 %. This must be regarded as very good since such measurements are notoriously sensitive to free-stream turbulence [21-23].

6. A second peak (Fig. 4.7a only) as the injector bounces and draws the model down through the shock again. This peak is broader than the first, on account of the slower speed at which the model is travelling, and slightly lower on account of the increased wall temperature, T_w , which means that $q \propto (T_0 - T_w)$ is lower. This again affords us a useful cross check on our measurements.

We can, of course, reproduce the whole record in reverse by quickly retracting the model from the tunnel and at a different speed if desired since the injection and retraction speeds may be varied independently. However, the starting

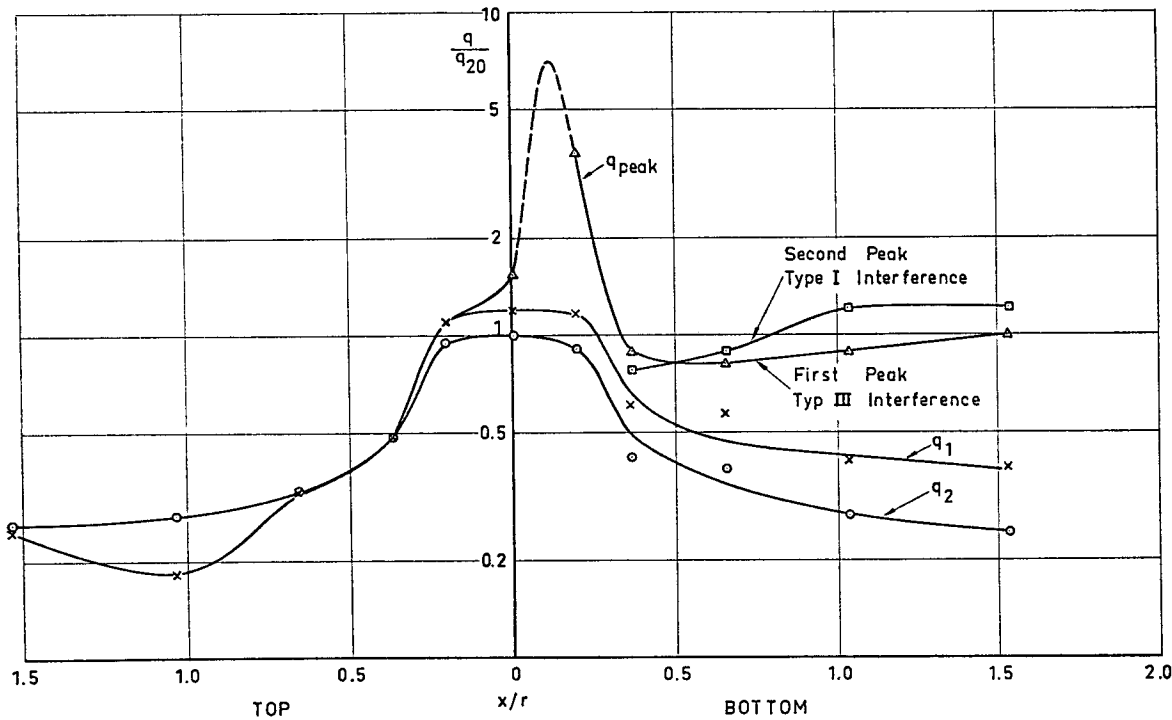


Fig. 4.12. q_1 , q_2 and q_{peak} as a function of x/r for a blunted cone. $M = 4.6$. $\xi = 5^\circ$.

conditions are less easily defined and there is the practical difficulty that although the models are robust it is advisable not to expose the films too long to the tunnel flow, since a chance hit from a solid particle could damage a gauge. Since both the injection speed and the position of the shock are accurately known, it is possible to determine when the peak heating occurs at a particular point on the model. It in fact occurs near the point where the impinging shock intersects the bow shock on the model. However, it is also evident from the experimental records that the peak heating is very localized, the width of the peak being a measure of the width of the region over which increased heating occurs on the model. Thus, if Δx is the width of this region, then we find for the case of the hemisphere that $\Delta x/r$ is the order of 0.1 to 0.3, being a minimum near the point where q_{peak} is a maximum.

In order to pinpoint exactly where a peak occurred, the output of the analogue network was taken via a D.C. amplifier and variable-level, variable-delay triggering network to a spark generator. The triggering level was adjusted so that a spark picture could be taken to coincide with the peak heating measured at a chosen point on the model. Coincidence better than 0.25 msec in time or 0.5 mm in model position was achieved; the output from the analogue network and a photocell, which could detect the spark, being monitored on the same oscilloscope. Fig. 4.14 shows the result of this experiment for a hemisphere at $M = 7$ and $\xi = 10^\circ$. (Here $q_{\text{peak}}/q_{20} \approx 10$.) Clearly, the peak heating in this case occurs at the point on the model where a free shear layer, originating at the intersection of the impinging shock and the bow shock, meets the model surface. Peaks at other points on the model could be variously attributed to attaching shear layers, jets or transmitted shocks.

Similar experiments performed using the blunted cone showed that the first of

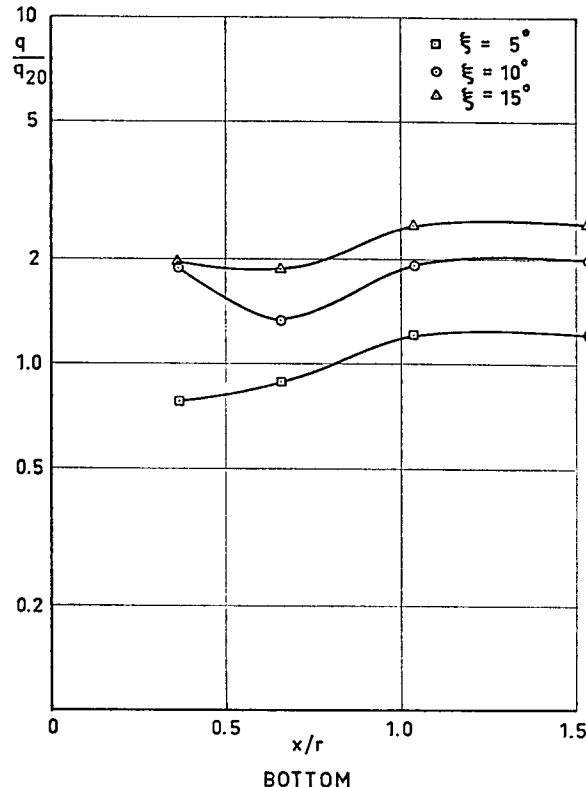


Fig. 4.13. q_{peak} (Type I interference) as a function of x/r for a blunted cone showing effect of varying ξ . $M = 4.6$.

the two peaks, measured on the underside of the model, was due to a free-shear layer meeting the surface of the model and the second a transmitted shock.

5. PRESSURE MEASUREMENTS

Pressure measurements were carried out using both conventional pressure-plotting techniques and a quasi-static technique similar to that developed for the heat-transfer measurements.

5.1. Measurements using conventional techniques

These measurements were carried out with the model at various fixed heights relative to the impinging shock, pressures being measured using mercury manometers. Nevertheless it was still necessary to have the model out of the test section before a run,

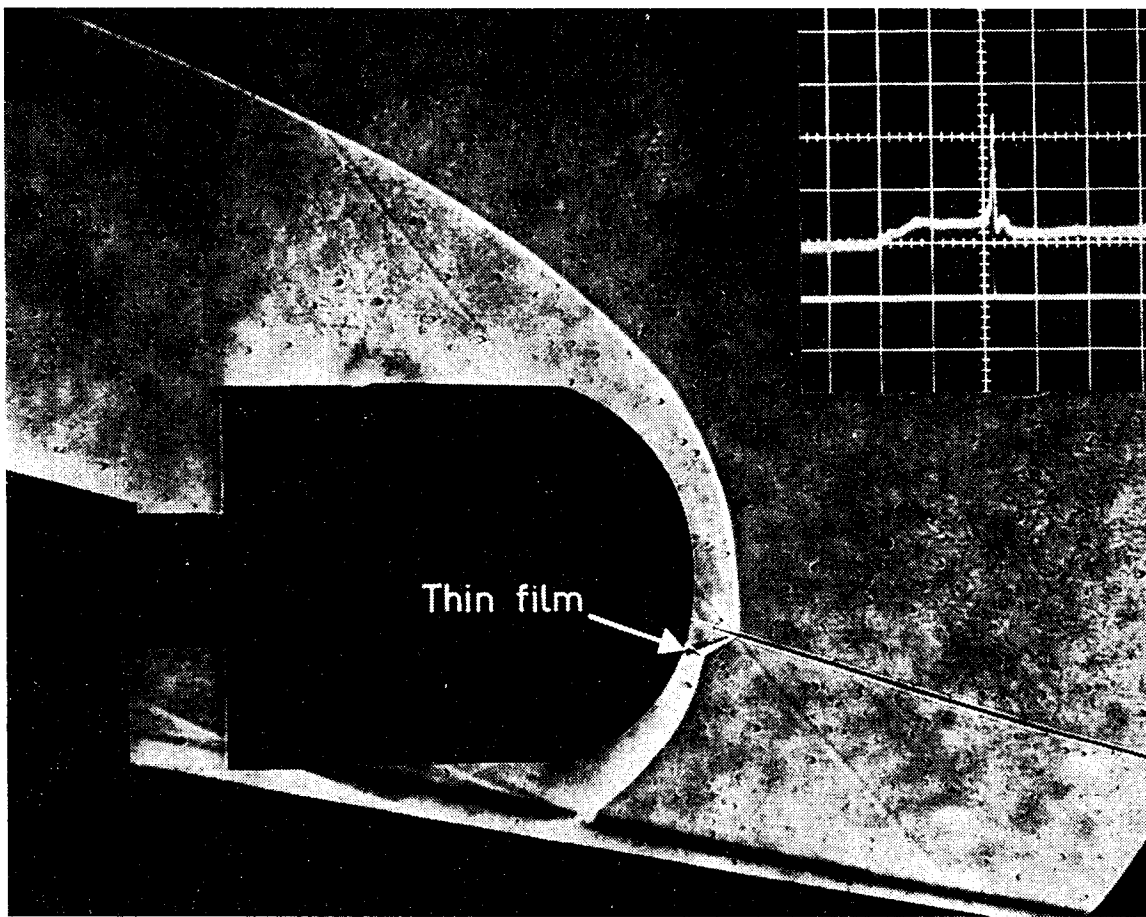


Fig. 4.14. Spark photograph taken at instance peak heating is recorded. Oscilloscope monitors heat-transfer rate and spark discharge. $M = 7$. $\xi = 10^\circ$.

in order for the tunnel to start. Consequently, the model was mounted on the injector, as before, but raised and lowered manually. Fig. 5.1 shows the three models used for these tests—a hemisphere/cylinder, a flat-faced cylinder and a blunted cone/cylinder. The models were 30 mm diameter, of similar geometry to the glass models used for the heat-transfer tests. Each model had 19 pressure tappings. The arrangement of the holes is evident from Fig. 5.1 and the pressure records, Figs. 5.2–5.6. The asymmetric arrangement of holes about the centre line, on the flat-faced cylinder and the blunted cone/cylinder, was designed to give a closer spacing of holes on the side of the model nearest the plate, since it was anticipated that the pressure variations in this region would be most abrupt. Unfortunately, the flat-faced

cylinder was mounted into its holder upside-down and the error not discovered until the brass pressure tubes had been bent and brazed into the sting. Since rebuilding the model would have disrupted the tunnel schedule, it was run in this condition, resulting in slightly poorer resolution around the lower lip of the model than had been desired. Fortunately, the results are still acceptable.

Tests were carried out at $M = 4.6$ for plate angles $\xi = 5^\circ$ and 10° . At $M = 7$ an unsteady separation on the plate, caused by the thicker sting necessary to take out the pressure tubes, resulted in an oscillation of the impinging shock with an amplitude of about 1–2 mm. The $M = 7$ series of tests were therefore abandoned. Also it was impossible to obtain a complete set of runs

with the blunted cone at $M = 4.6$ and $\xi = 10^\circ$ over all positions of the model relative to the shock, again due to problems with boundary-layer separation on the plate. Consequently, these are not presented.

Spark-illuminated schlieren photographs were taken for each run to establish the exact position of the model relative to the shock. These are displayed opposite the corresponding pressure distributions in Figs. 5.2-5.6.

In each figure the point at which the disturbance from the impingement point meets the model surface is marked with an arrow. This disturbance can be a shear layer, a jet, a shock or even an expansion as we shall see later. In general this arrow coincides with a pressure peak or a discontinuity depending on the nature of the disturbance.

Figs. 5.6 B and C are particularly interesting since they illustrate how the same point on the underside of the cone can be sensitive to two different types of interference. In Fig. 5.6 C it is the free shear layer originating near the nose of the model and in Fig. 5.6 B it is a transmitted shock which subject the same point to increased heating. This accounts for the two peaks in the heat-transfer rate as the cone model traverses the shock (Fig. 4.7c).

In the case of the hemisphere the exact peak pressure is also indicated, using the results of the quasi-static tests described in Section 5.2 below. We note the excellent agreement between the static and quasi-static measurements especially when the peak coincides with the position of a pressure tapping as shown in Fig. 5.2 D and also in Fig. 5.6 D where the shock impinges on the spherical nose of the cone model.

5.2. Measurements using quasi-static injection technique

Although the measurements described above give an excellent overall picture of the pressure variations on the model, they are lacking insomuch that it is not possible to resolve the peak pressure exactly, on account

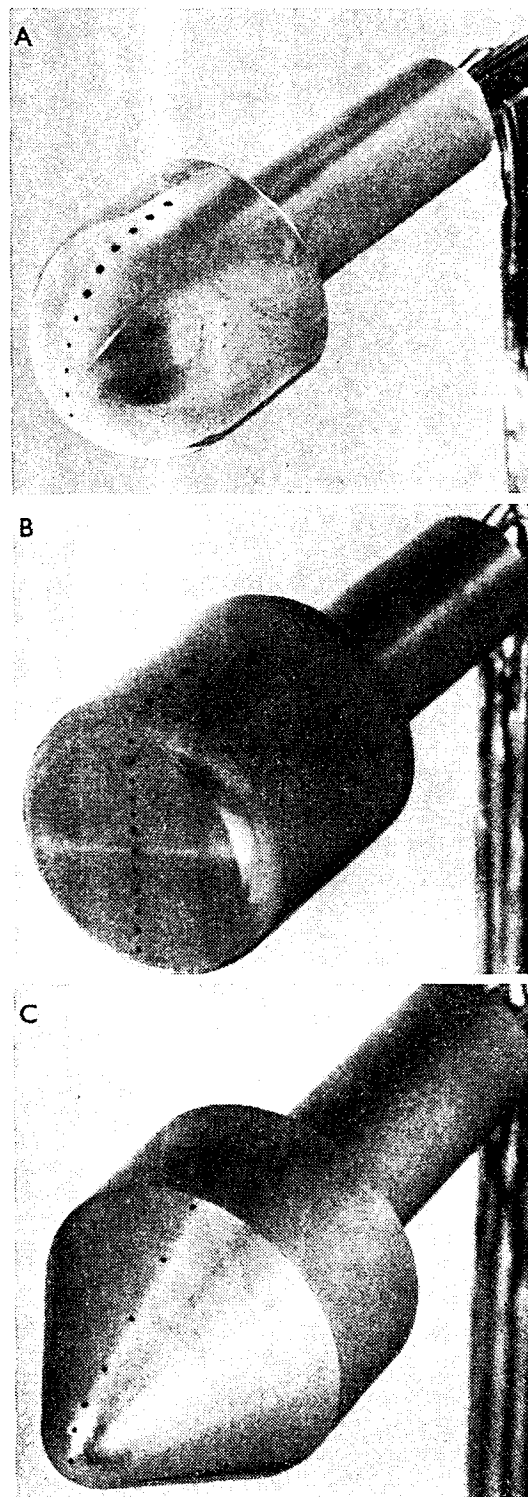


Fig. 5.1. Pressure plotting models. All 30 mm diameter.

of the finite spacing of the pressure tappings. Consequently, it was decided to develop a quasi-static technique analogous to that

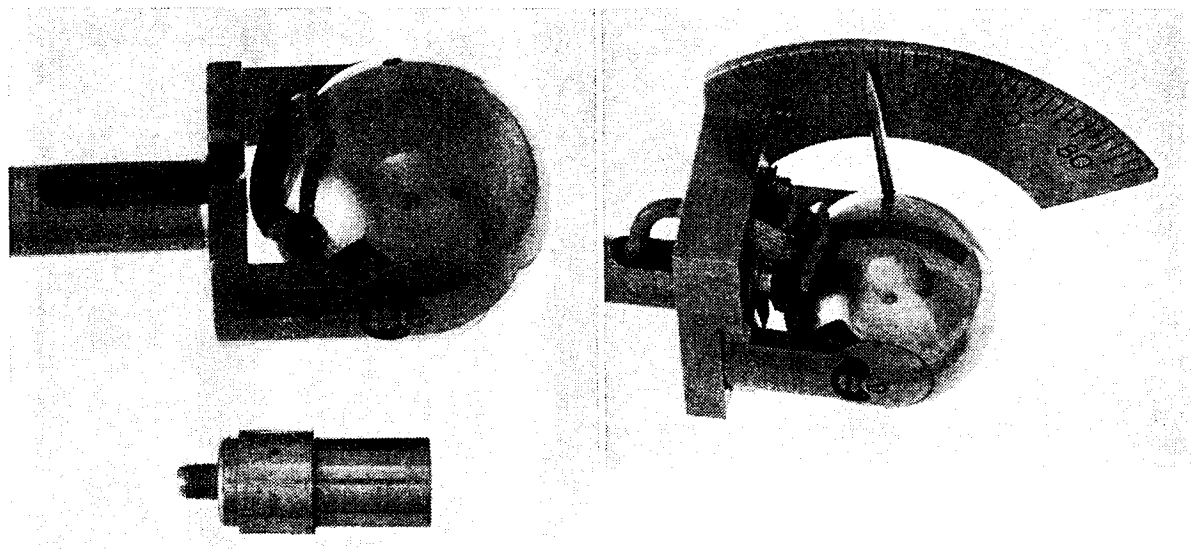


Fig. 5.7. Pressure model used for quasi-static tests. *a*. Model and Kistler 701 transducer. *b*. Pointer and quadrant to measure inclination of pressure orifice on centre line of model.

used for the heat-transfer measurements described in Chapter 4. The pressure was to be measured by a single Kistler 701 pressure transducer mounted inside the model. The large size of the transducer dictated a sphere. With such a shape pressures at various points along the centre line could be measured by simply rotating the sphere about an axis parallel to the leading edge of the plate, the overall geometry being unchanged. A detachable, graduated quadrant and pointer enabled the exact position of the pressure tapping to be determined (Fig.

5.7). Tests were carried out at $M = 4.6$ ($\xi = 5^\circ, 10^\circ$ and 15°) and $M = 7$ ($\xi = 5^\circ$ and 10°).

Typical pressure records are shown in Fig. 5.8. The first peak is due to boundary layer interference. This is then followed by a steady level, p_1 , as the model traverses the shock layer, a second peak, p_{peak} , as the model passes through the shock and finally a second steady level, p_2 , as the model passes out into the free stream. Comparing the pressure records shown in Fig. 5.8 with the heat-transfer records shown in Fig. 4.7, we

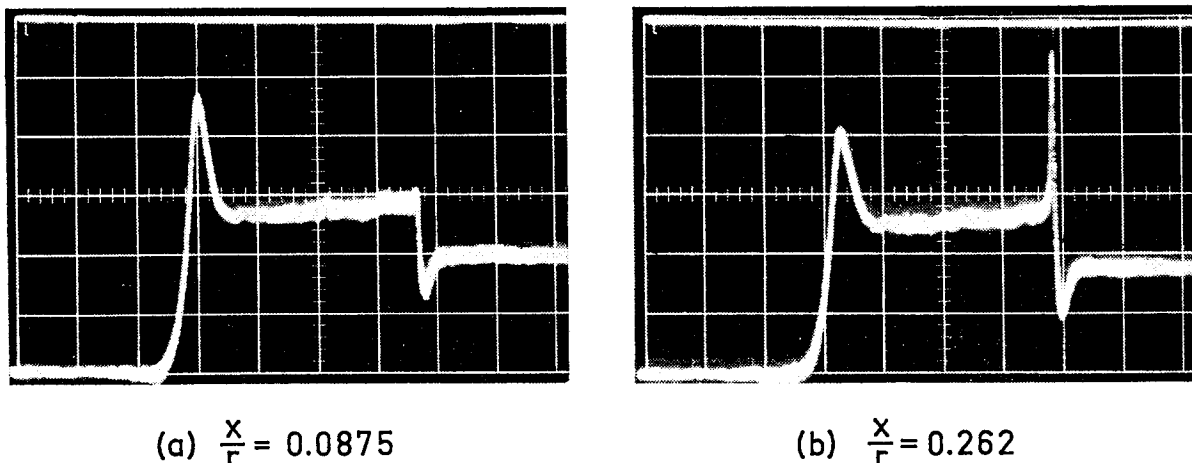


Fig. 5.8. Typical pressure records on underside of sphere. Transducer in sphere. $M = 4.6$. $\xi = 5^\circ$. Sweep rate 25 msec/cm.

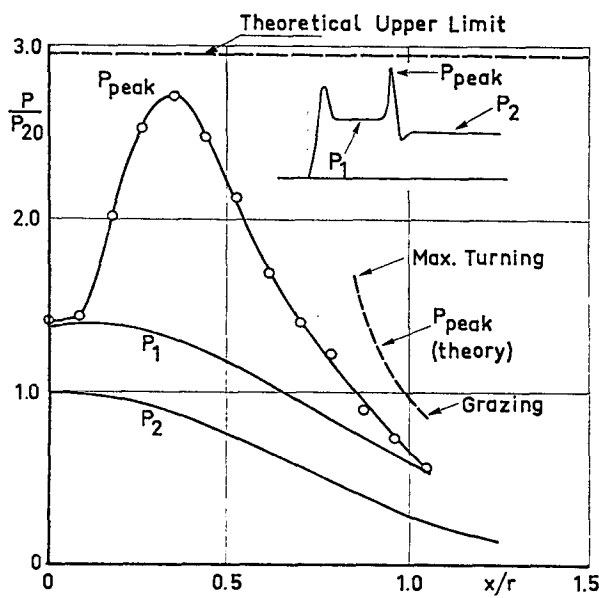


Fig. 5.9. Peak pressure as a function of x/r on underside of sphere. $M = 4.6$. $\xi = 5^\circ$.

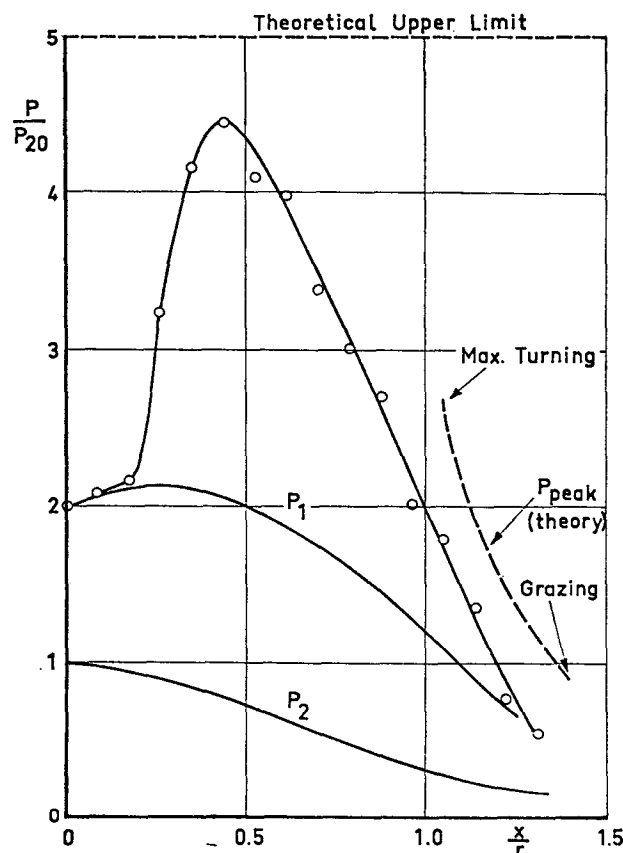


Fig. 5.11. Peak pressure as a function of x/r on underside of sphere. $M = 4.6$. $\xi = 15^\circ$.

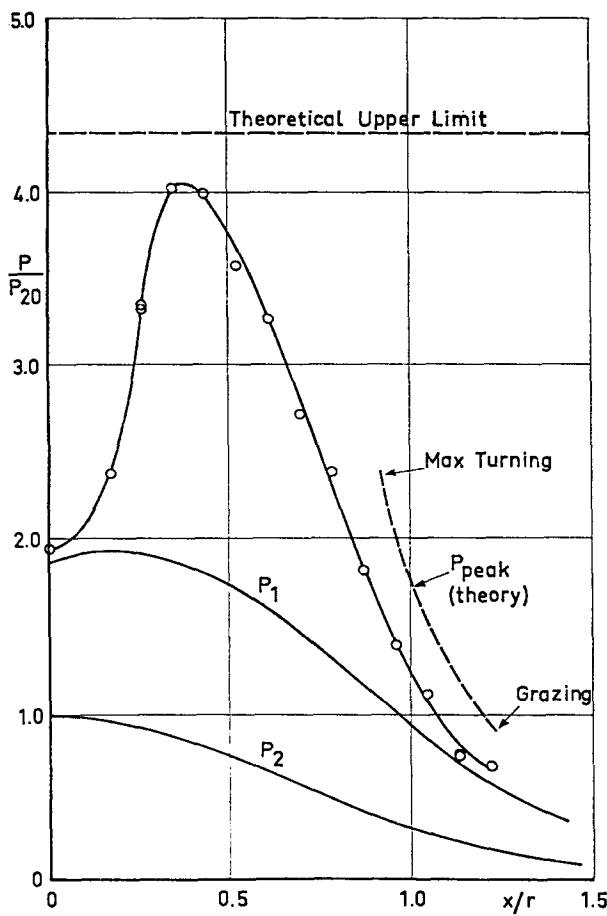


Fig. 5.10. Peak pressure as a function of x/r on underside of sphere. $M = 4.6$. $\xi = 10^\circ$.

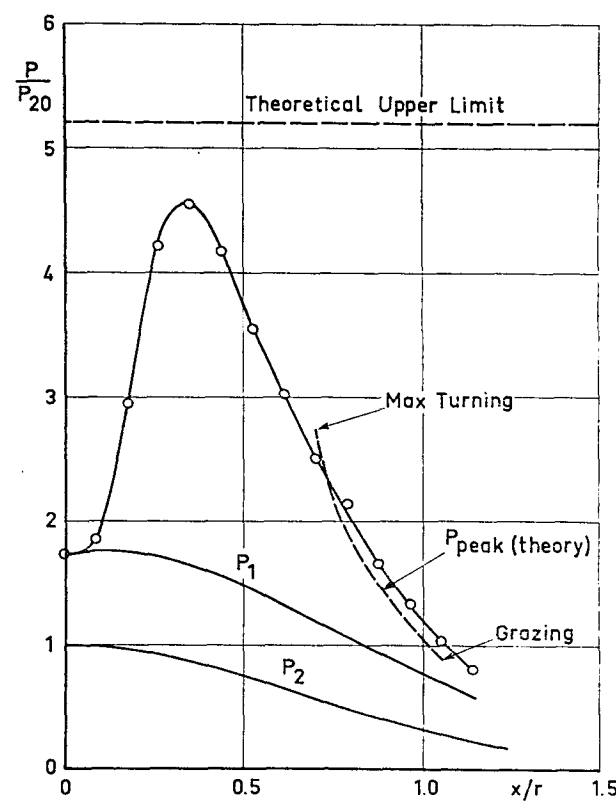


Fig. 5.12. Peak pressure as a function of x/r on underside of sphere. $M = 7$. $\xi = 5^\circ$.

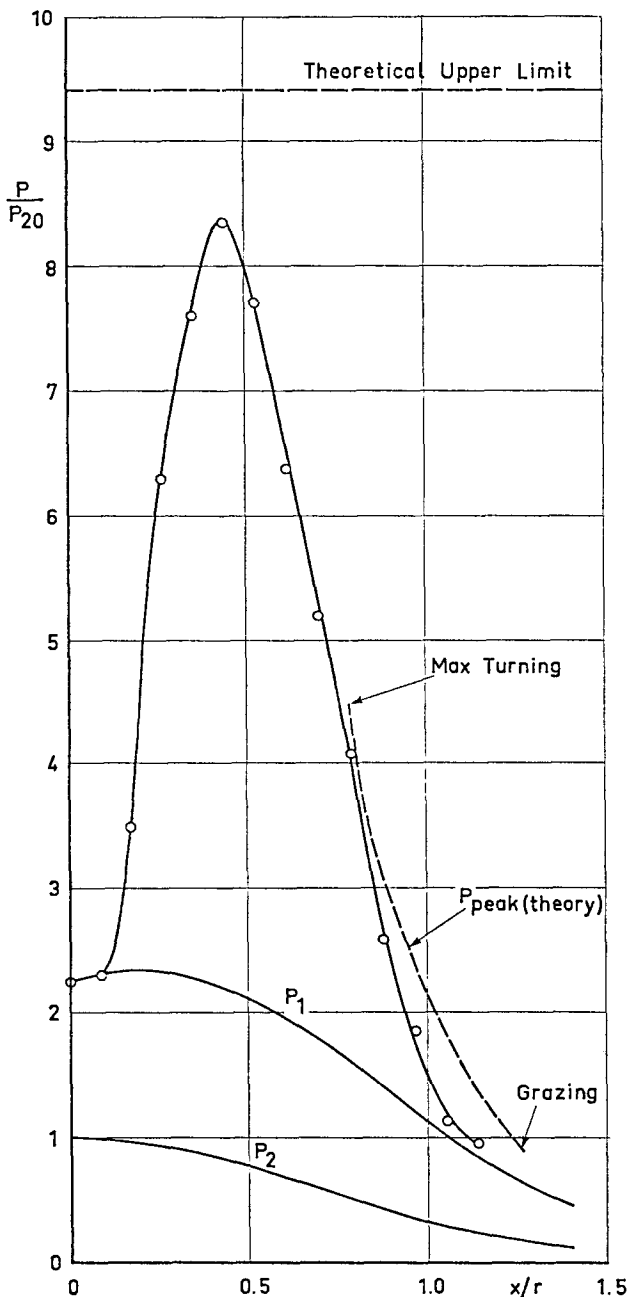


Fig. 5.13. Peak pressure as a function of x/r on underside of sphere. $M = 7$. $\xi = 10^6$.

note a remarkable similarity between the two types of measurements.

This is further emphasized in Figs. 5.9–5.13 where p_{peak} , p_1 and p_2 have been plotted as a function of x/r for the lower half of the model. We see how the peak pressure reaches a maximum just below the

axis of the model, falling off rapidly above this point. This is exactly the same variation exhibited by the peak heating shown in Figs. 4.10 and 4.11. Moreover, the dependence on the strength of the impinging shock and free-stream Mach number is similar in both cases, increasing both with the strength of the impinging shock and the Mach number.

The technique of spark schlieren photographs, triggered in this case by the peak pressure, was again employed to determine exactly where the peak pressure occurred on the model. As expected from the static measurements, described above, and the heat-transfer measurements presented in Chapter 4, it occurred where a jet, free shear layer or shock impinged on the surface of the model.

Since the response time of the pressure transducer was longer than that of thin-film gauges it was necessary to reduce the injection speed. The injection speed was determined by systematically reducing it from a maximum until the peak pressure, p_{peak} , showed no further increase. At $M = 4.6$ the injection speed arrived at was 0.5 m/sec and at $M = 7$ 0.25 m/sec.

Problems with thermal drift in the transducer output were eliminated by running at as low a stagnation temperature as possible, sufficient to avoid condensation, and at as high an injection speed as possible, consistent with the need to accurately reproduce the full peak pressure.

The pressure transducer was calibrated in the model by measuring the stagnation-point pressure (i.e. at $x/r = 0$) in the free stream and comparing it with the pressure measured using the hemisphere under similar conditions as described in Section 5.1 above. A comparison of p_1 and p_2 as a function of x/r , using both the conventional and quasi-static techniques showed excellent agreement, as indeed one would expect.

We shall return to the results of the pressure measurements in Chapter 7 when they will be compared with the theoretically predicted variations.

6. PREDICTION OF INTERFERENCE PATTERNS

A first step in understanding the effects of shock impingement is to determine the interference pattern set up when two oblique shocks of different strengths intersect. What we particularly want to find out here is how this pattern varies with the strength of the extraneous shock and the geometry of the body, on which the extraneous shock impinges. Knowing this, it is then possible to predict—or at least make an intelligent guess—what effects this interference will have on the pressure distribution and flow around the body and hence the effect on the heat transfer around the body. Although in hindsight such an approach may appear the most obvious and straight-forward one, it has nevertheless been overlooked by all other workers studying shock impingement and must account in some measure for their singular lack of success in understanding this phenomenon.

When two shocks of unequal strength intersect, the streamline through the intersection point divides the flow into two portions, which experience different changes in crossing the shock-wave system. The net result must be such that the two portions have the same pressure and the same flow direction immediately down-stream of the intersection point. However, the magnitude of the velocity, together with the temperature and density, are different on either side of this dividing streamline, which is in fact a shear layer or contact surface. Given the strengths of the two intersecting shocks it is generally quite simple to determine the resulting shock intersection pattern and flow variables.

Unfortunately, in the present investigation the strength of only one of the shocks is known, that of the impinging shock. The strength of the bow shock ahead of the model is in general unknown, depending not only on the shape of the model but also on the strength and position of the impinging shock. This is demonstrated most clearly in Figs. 6.1, 6.2 and 6.3. Each figure

represents a series of spark photographs taken at the same Mach number ($M_\infty = 4.6$) and plate angle ($\xi = 5^\circ$) but at different positions of the model relative to the impinging shock. It is evident that only small changes in the position of the model relative to the shock are necessary to produce quite marked changes in the flow around the model.

For the purpose of the present discussion we shall need to divide up these interference patterns into six distinct types. Two different methods have been used to predict the various patterns, one a graphical method using pressure, flow-deflection, polar diagrams and the other a numerical method. Since the graphical method gives a better insight into the physics of the problem we shall discuss this first.

6.1. *The heart diagram method*

As we have already stated, two conditions must be fulfilled downstream of the intersection of two oblique shocks, namely that the same pressure and the same flow direction prevail on either side of the dividing streamline. Consequently, this suggests we cast our problem in a form involving the pressure rise and flow deflection through one or more oblique shock waves, relative to some common starting point, i.e. the pressure and flow direction in the free stream, (∞). If, for some given Mach number, we plot the pressure behind an oblique shock as a function of the flow deflection through the shock we obtain a closed, heart-shaped curve. It is this characteristic shape which lends its name to this method. At an arbitrary point, 1 say, on the curve, not only are the pressure and deflection defined but the Mach number, M_1 , and other flow variables behind the shock are also uniquely determined. This point, in turn, may serve as the origin for another heart curve, the shape and size of which is a function of M_1 and p_1 only. In a similar fashion we may construct a third curve from some origin 2, say, and the point in which the two curves intersect defines a pressure and flow deflection which may be arrived at by traversing two separate shock systems in different

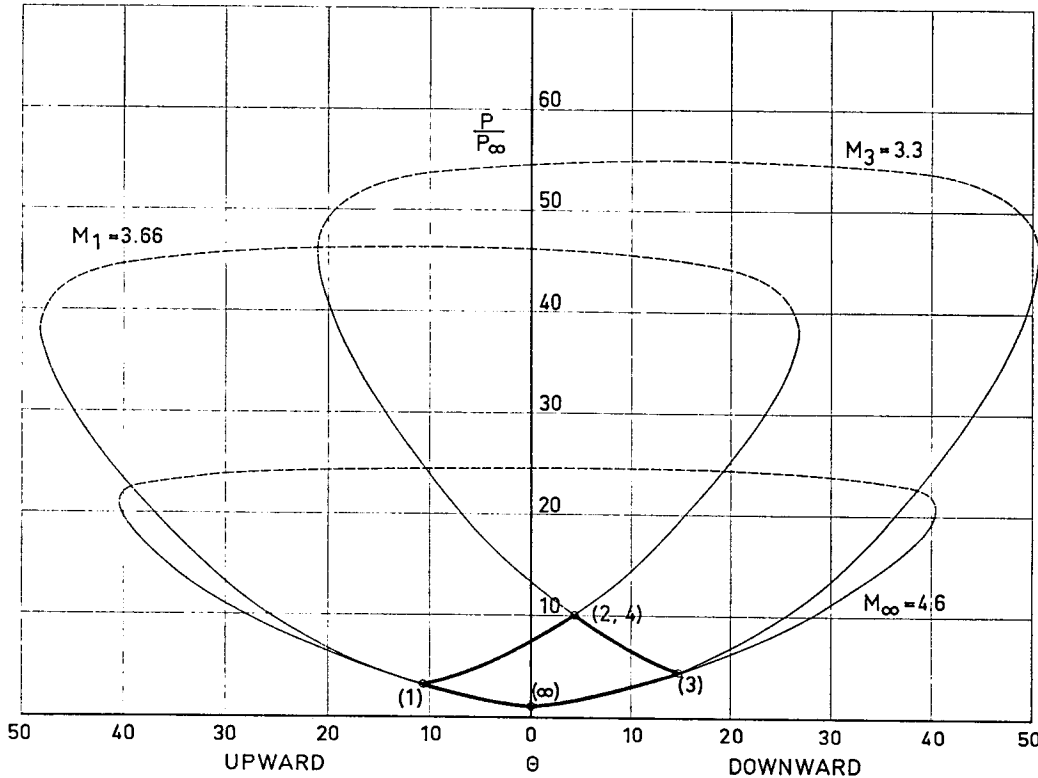


Fig. 6.5. Heart diagram for Type I interference.

ways. We shall see more clearly how this works if we proceed directly to a discussion of our six interference types.

Type I interference. This occurs when the extraneous shock meets the bow shock well below the lower sonic line. Fig. 6.4 illustrates this type of interference on models of varying geometry. In this case the strength of the bow shock at the impingement point is known, at least in principle, since that part of it above the impingement point is unaltered from its shape in the undisturbed free stream. Fig. 6.5 illustrates the use of the heart-diagram method to predict the strength of the transmitted shocks PR and PS . Let us suppose that the free-stream Mach number, M_∞ , is 4.6 and that the deflection through the extraneous shock is 10.6° . This defines the conditions in region 1, Fig. 6.5, with $M_1 = 3.66$. Starting from an origin at 1 we construct the $M_1 = 3.66$ curve. Similarly we assume that the deflection through the bow shock immediately above the impingement point is known, say

14.8° . This defines conditions in region 3, with $M_3 = 3.3$. The point in which the $M_3 = 3.3$ curve intersects the $M_1 = 3.66$ curve then gives the pressure and flow deflection in regions 2 and 4 and hence the strength and inclination of the shocks PR and PS .

The reader will also observe a second intersection of the $M_3 = 3.3$ and $M_1 = 3.66$ curves and ask why this, too, does not give a second, strong-shock solution. The reason is two-fold. First, since the potential energy of the system is lower for the weak-shock solution, it occurs in preference to the strong-shock solution wherever possible. This we are familiar with in, say, supersonic flow over slender wedges where only the weak-shock solution is physically realizable. Secondly, the strong-shock solution, in this case, would demand a net upward deflection of the subsonic stream in region 2, behind the shock PS , and hence is sensitive to the presence of the model. Thus we cannot arbitrarily fix the position of any point

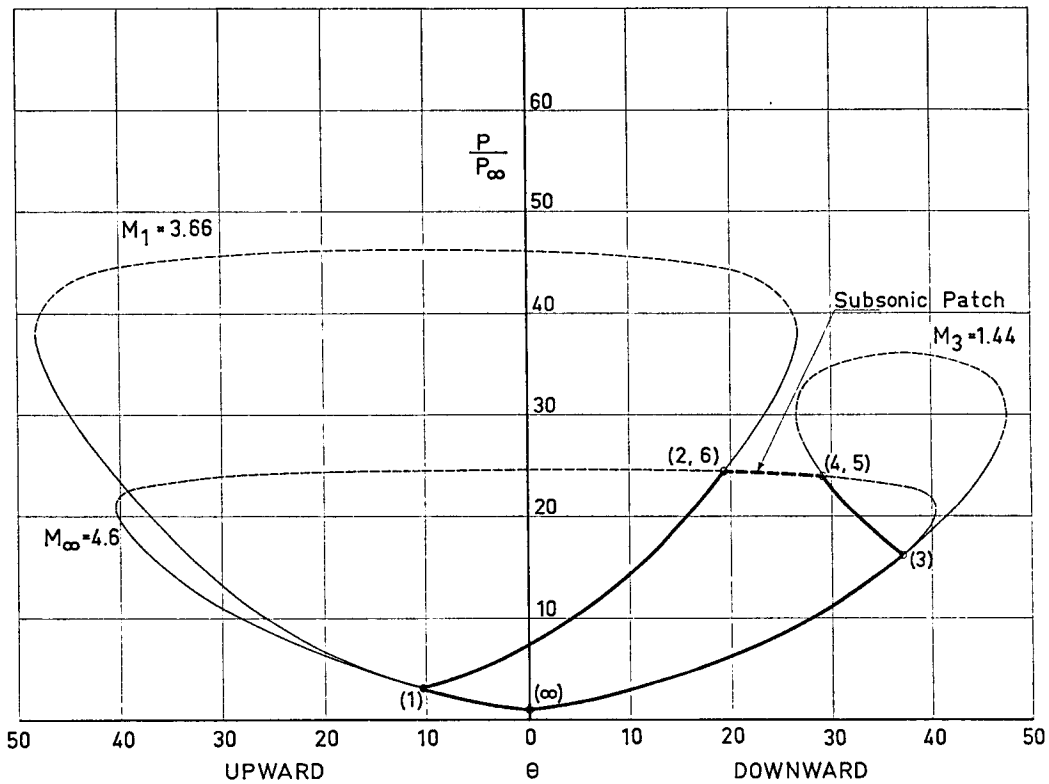


Fig. 6.7. Heart diagram for Type II interference.

of the shock PS relative to the model, in particular the impingement point, P , as we have done.

Assuming, therefore, the weak shock solution, with supersonic flow down-stream of the impingement point, we can quite easily calculate the entire flow field and the shape of the transmitted bow shock, using the method of characteristics.

The shear layer originating at the impingement point does not meet the surface of the model and, consequently, there is no local increase in heating on this account. However, the shock PR can impinge on the surface of the model and may be sufficiently strong to promote separation of the boundary layer on the model ahead of the impingement point and/or transition to turbulence, as is shown clearly in Figs. 6.4b and 6.4c. Shock/boundary layer interactions of this type have received considerable attention by several authors over a number of years now and although much progress has been made in calculating laminar inter-

actions (see for example Holden [35]) our present state of knowledge is far from complete. However, this is only a small part in the overall study of shock impingement and we shall merely assume that criteria are available to predict whether separation and transition will occur, knowing the flow conditions in region 3 and the strength of the shock PR . The important point is that there will be a large increase in the heat-transfer rate through the interaction region. In addition we can calculate the heat transfer to the model downstream of the impingement point, assuming either a laminar or a turbulent boundary layer, and knowing the flow conditions in regions 3 and 4 adjacent to the boundary layer.

Type II interference. This occurs when the extraneous shock meets the bow shock just below the lower sonic line. This is illustrated in Fig. 6.6 for models of various geometry. In this case the curves with origins at points 1 and 3, Fig. 6.7, lack an intersection point and no Type I solution exists. Again by way of

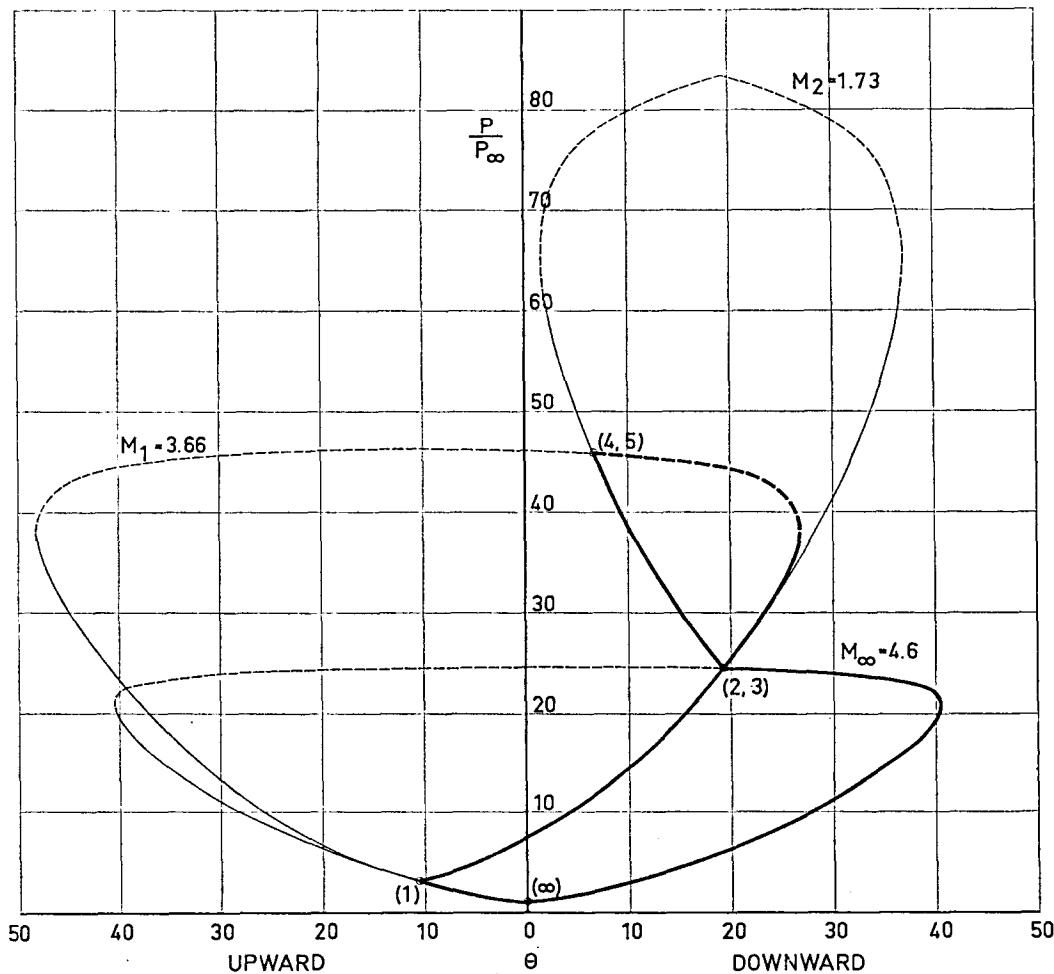


Fig. 6.9. Heart diagram for Type III and Type IV interference.

illustration we have chosen $M_\infty = 4.6$ and the same strength for the extraneous shock as in Fig. 6.5, but the strength of the bow shock above the impingement point has now been increased resulting in a lower $M_3 = 1.44$. We see that the $M_1 = 3.66$ and the $M_3 = 1.44$ curves can only be joined by a subsonic patch along the $M_\infty = 4.6$ curve. This patch is represented by the curved shock QP in Fig. 6.6. The intersection of the $M_1 = 3.66$ and the $M_\infty = 4.6$ curves gives the conditions in regions 2 and 6 and the intersection of the $M_3 = 1.44$ and $M_\infty = 4.6$ curves gives the conditions in regions 4 and 5.

However, this solution is not unique for the following reasons.

Although the conditions in regions 2 and 6 are uniquely determined and are func-

tions of the free-stream Mach number and the strength of the impinging shock only, this is not true of the conditions in regions 4 and 5. This is a result of the fact that the width of the subsonic region QP is dependent on the geometry of the body. Thus we cannot a priori fix the position of Q and hence determine M_3 . All we can say is that Q lies somewhere between the impingement point P and the lower sonic line and that the part of the bow shock above the point Q is unaltered from its shape in the undisturbed free stream.

However, supposing we could fix Q and the shape of the patch QP , then the entire flow field may be calculated as before. An inverse method may be used to calculate the subsonic flow field behind QP until the

flow becomes sonic. We note that the dividing streamlines originating at Q and P converge, a necessary condition for the subsonic flow to accelerate. The method of characteristics would be used for the supersonic regions.

The differences in flow variables—velocity, Mach number, density, etc.—across the shear layer originating at a Q are generally small and the effect on the local heat transfer, if it meets the surface of the model, is small. The shear layer originating at P , however, can cause a large increase in the local heating if it meets the model surface. We shall have more to say about this when we discuss Type III interference, since the conditions are identical.

The shock QR also interacts with the boundary layer on the model, resulting in separation or transition. This is seen clearly in Fig. 6.6 b. The same remarks concerning shock/boundary layer interaction and prediction of the heating through and downstream of the interaction, made when discussing Type I interference, apply here, too.

We see that there is a natural transition from Type I to Type II interference at the point where Q collapses onto P , that is to say the M_1 and M_3 heart curves touch. As the impingement point moves upwards on the model and Q approaches the sonic line the shock QR first strengthens and then progressively weakens again. When Q reaches the sonic line the shock QR vanishes, marking the transition to Type III interference.

Type III interference. This occurs when the extraneous shock meets the bow shock within the subsonic region ahead of the model. Again this is illustrated for bodies of various geometry in Fig. 6.8. Assuming the same free-stream Mach number and flow deflection through the impinging shock as before, conditions in regions 2 and 3 are determined by the intersection of the $M_\infty = 4.6$ and $M_1 = 3.66$ curves, as indicated in Fig. 6.9. It is important to note that the conditions in regions 2 and 3 are independent of the shape of the body, providing it is blunt. The flow in region 3 is then subsonic and that in region 2 supersonic. Depending

on the angle the dividing streamline or shear layer PR makes with the tangent to the body surface and providing the Mach number, M_2 , in region 2 is sufficiently high, the shear layer PR is undeflected and attaches to the model surface, the supersonic flow being deflected downwards through an attached oblique shock RQ . The Mach number in region 2 in this example is $M_2 = 1.73$. The heart curve for this Mach number with origin at the point 2 is drawn in Fig. 6.9. This curve then gives the pressure rise for various turning angles through the shock RQ . It also indicates the maximum angle through which it is possible to deflect the supersonic flow in region 2, by means of a single oblique shock.

The pressure rise between the shock and the body in region 3 is small compared with that through the shock RQ since the flow in region 3 is subsonic ($M_3 = 0.46$) and consequently there is a marked pressure rise through the attachment region R . This has the result of thinning the boundary layer and hence increasing the heat transfer near the attachment point R . In addition, the Reynolds number in region 2 may be high enough for transition to occur in the shear layer PR before attachment. This also contributes to an increase in the local heat-transfer rate.

Although the shock configuration in the immediate vicinity of P is easily determined, being a function of the free-stream Mach number and the strength of the impinging shock only, the shock stand-off distance, and hence the length of the shear layer PR , is less easily determined, since it is dependent upon the geometry of the body as well as the position of the impinging shock.

In addition the actual flow picture near the attachment point R and at the shock-intersection point Q is more complicated than we have indicated in Fig. 6.8. A result of a more detailed calculation is shown in Fig. 6.10. In general there is a small pressure rise ahead of the attachment point R , approximately equal to the pressure rise on the subsonic side of the shear layer PR (since R is a stagnation point for the sub-

sonic flow in region 3). This accounts for the shock OM . The length OR is the same order as the width of the shear layer PR near the attachment point but no way of determining this length exactly has yet been established.

The strength of the curved shock RM at the point R is fixed by the inclination of the wall to the flow in region 7. However, near the point M the strengths of the shocks RM and MN are determined by the Mach number M_2 and the strength of the shock OM only, in the same way as we determined the strengths of the shocks KP and PQ . Similarly the conditions in regions 4 and 5 are determined by the intersection of the $M_1 = 3.66$ and $M_2 = 1.73$ heart curves (Fig. 6.9). Thus having fixed the strength of the shock NQ we may calculate the strength of the shock MN near the point N , as before.

The net result is subsonic flow in regions 8 and 9, separated by a free shear layer originating at M , and a supersonic jet, downstream of the shock NQ , which separates the subsonic region 9 from yet another subsonic region 4. We shall say more about such supersonic jets when we come to discuss Type IV interference. The lengths RM , MN and NQ cannot in general be determined, although NQ is usually very small as we see from the schlieren photograph accompanying Fig. 6.10 and the jet is for all practical purposes indistinguishable from a simple free shear layer. Neither this jet nor the shear layer from M meets the surface of the body. Consequently they have no effect on the heat transfer.

Type IV interference. It is clear from Fig. 6.9 that if the inclination of the model surface to the flow direction in region 2 exceeds a certain angle (for the example we have chosen about 18°), then the supersonic flow cannot be deflected downwards through an oblique shock. There follows as a result a dramatic change in the interference pattern. This is illustrated for bodies of various geometry in Fig. 6.11.

A supersonic jet is formed—a sheet in fact—which separates two subsonic regions 3 and 4. The conditions in regions 2, 3, 4

and 5 are determined with the help of the heart curves as in Fig. 6.9. The further development of the jet downstream of RT is determined by the method of characteristics and is compared with the experimentally observed pattern in Fig. 6.12. For the ease of calculation, we have assumed a constant pressure P_3 along the shear layer $PRMO$ and a constant but higher pressure P_4 along the shear layer QTN . This assumption is justified by the very good agreement with experiment. The result of a similar calculation and the corresponding schlieren photograph taken at $M = 7$ are shown in Fig. 6.13.

The jet curls upwards under the pressure differential $(P_4 - P_3)$ impacting the body surface through a detached shock UV (Fig. 6.11). Depending on the inclination of the jet to the body surface at the point of impact, the jet may be divided into two separate upward and downward streams VY and UX or be deflected completely upwards. The impact pressure can be several times the pressure in regions 3 or 4 on account of the already high pressure in region 5 and the fact that $M_5 > 1$ (here 1.26).

We also see quite clearly in Figs. 6.11 and 6.12 the repeated compression/expansion system within the jet and how shock waves are formed between the body and the free shear layer VY .

Unfortunately, one last step remains and it is an extremely difficult one, that of determining the width of the jet. It depends in turn on our being able to calculate the shock stand-off distances at P and Q . Although an approximate solution for a two-dimensional model, say a cylinder, might be forthcoming, it is extremely doubtful if a solution for a body of arbitrary shape could be obtained. At this point we must content ourselves with stating the experimentally observed facts that the width of the jet diminishes, and the jet curls up more and more, as the impingement point moves up the model (Figs. 6.1, 6.2 and 6.3).

Nevertheless once we fix the width of the jet from a schlieren photograph, say, then we can go on and say more about the

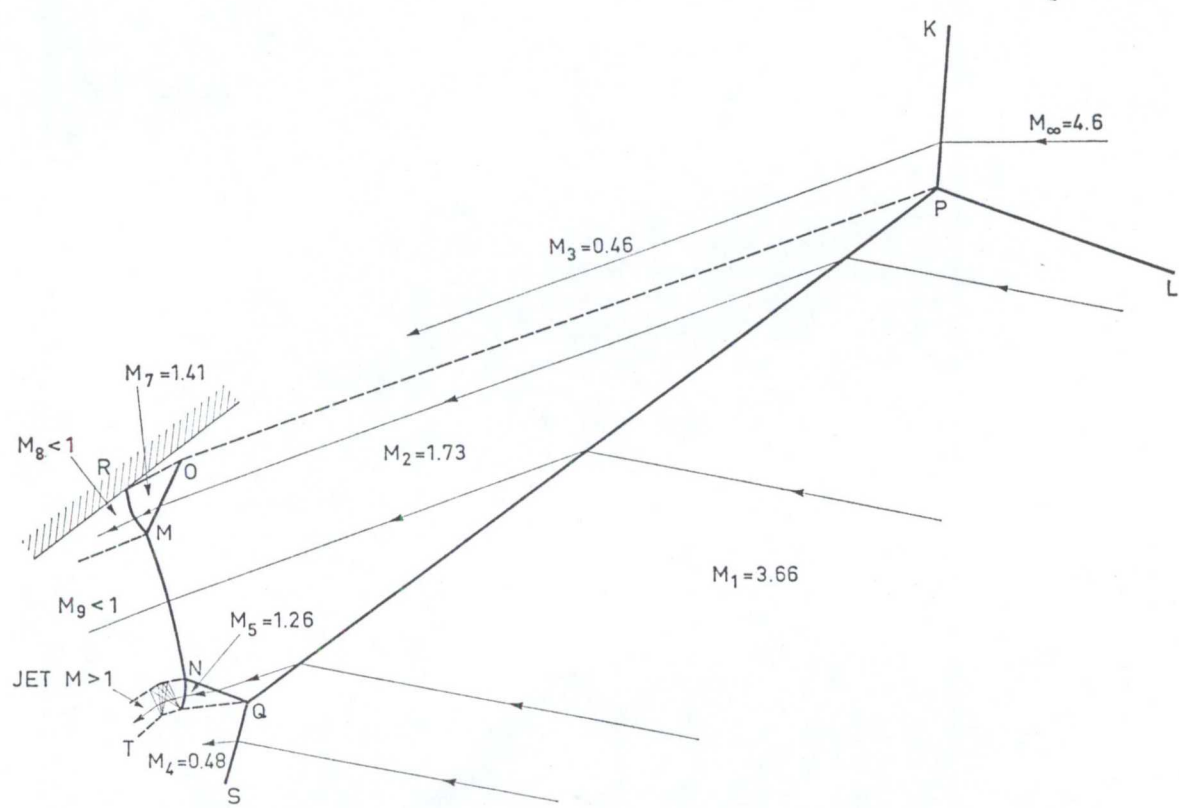
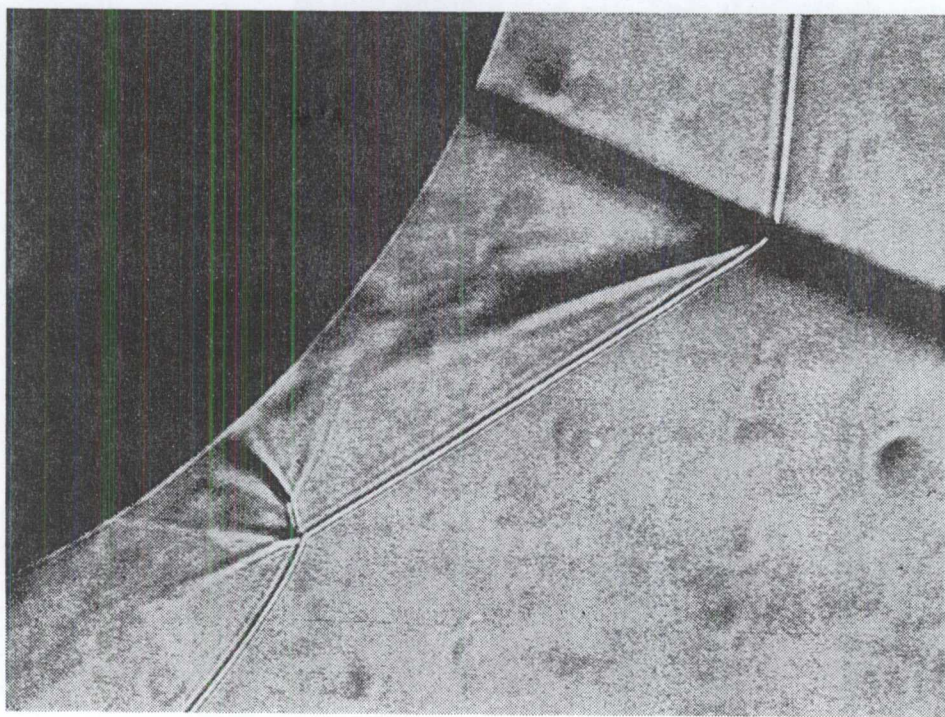


Fig. 6.10. Experimentally and theoretically determined flow patterns. Type III interference. $M_{\infty} = 4.6$, $\xi = 10.6^\circ$.
3 - 682828 Medd. 5

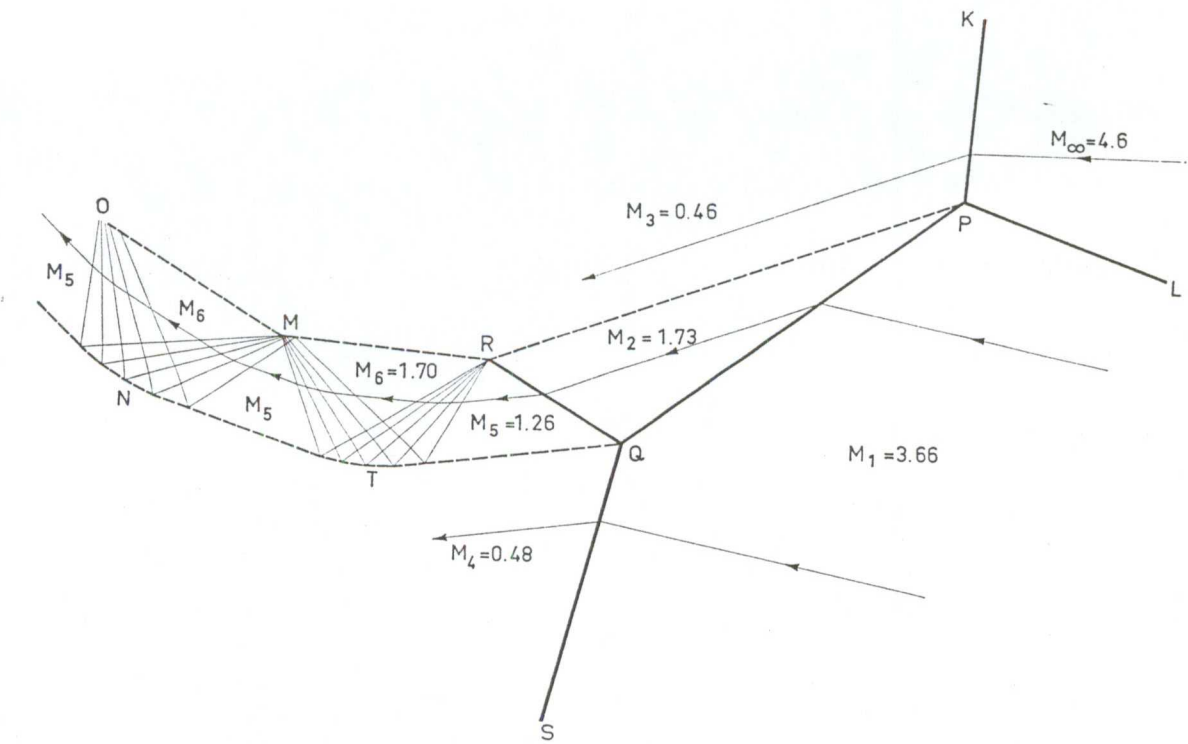
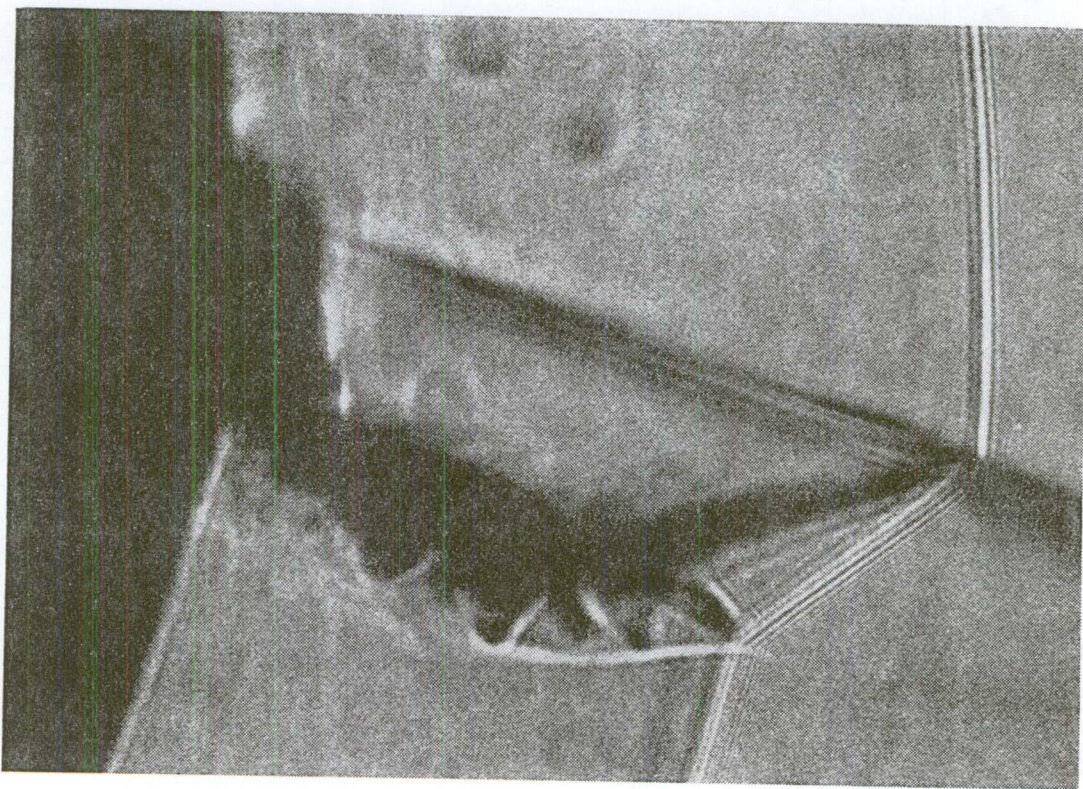


Fig. 6.12. Experimentally and theoretically determined flow patterns for Type IV interference. $M_{\infty} = 4.6$.
 $\xi = 10.6^\circ$.

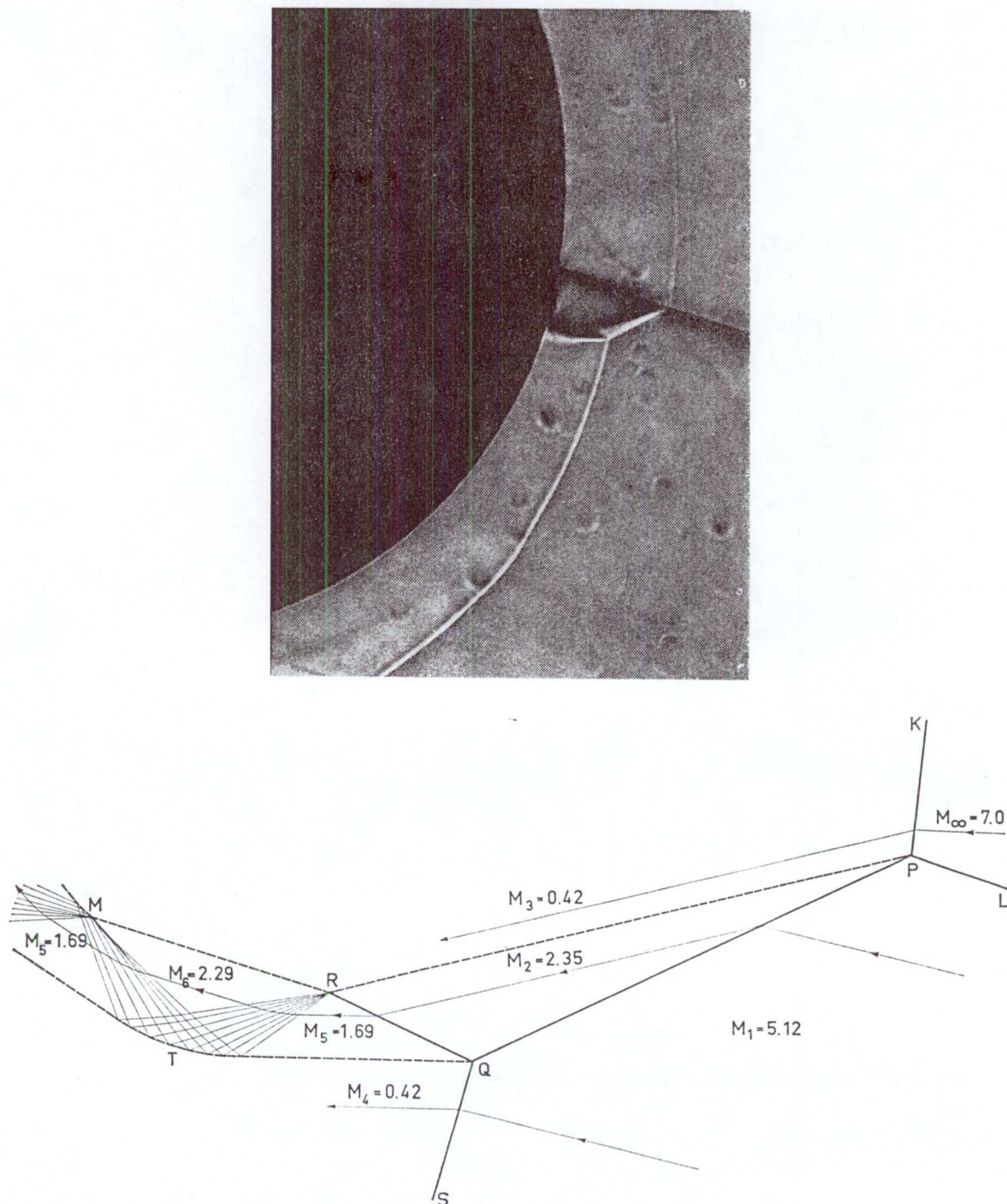


Fig. 6.13. Experimentally and theoretically determined flow patterns for Type IV interference. $M_\infty = 7.0$.
 $\xi = 10.6^\circ$.

heating near the impact point, as we shall see.

Type V interference. This occurs when the extraneous shock meets the bow shock just above the upper sonic line as illus-

trated in Fig. 6.14 for models of various geometry.

It is in fact analogous to Type II interference pattern we have already discussed. We shall therefore only point out the dif-

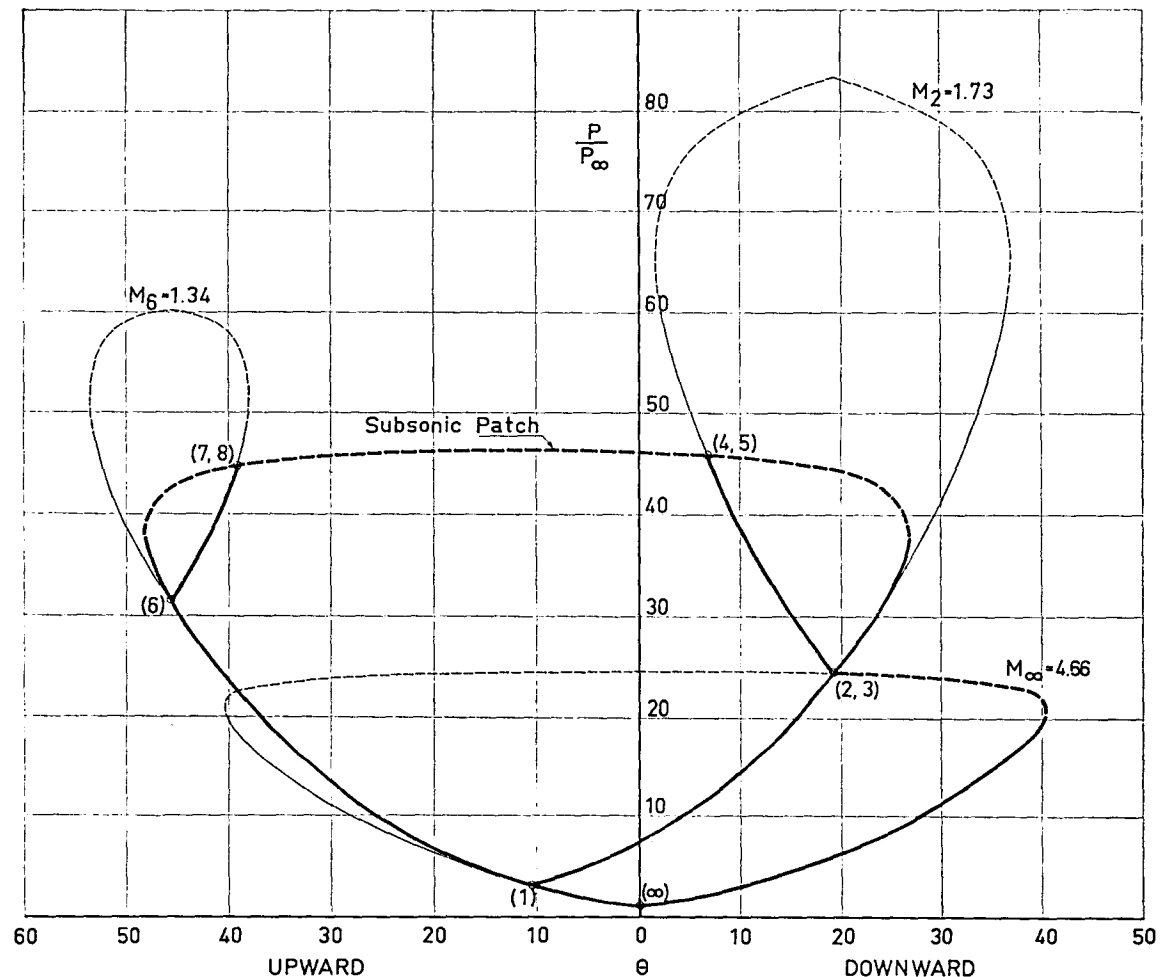


Fig. 6.15. Heart diagram for Type V interference.

ferences. Instead of a simple shear layer originating at the point P a jet is formed. This jet differs from the jet shown in Fig. 6.12 only insomuch that it is very much thinner. However, for all practical purposes it is undistinguishable from a shear layer. We note that the jet and the shear layer originating at Q converge as the subsonic stream downstream of the curved shock PQ accelerates to sonic speed. Both the jet and the shear layer diffuse rapidly meeting the body—if it is, say, a long fin—far outboard of the impingement point. Consequently, the jet and shear layer have much less influence on the heat transfer than for Type IV interference, although it should not be ignored, as we shall see.

The shock QR on the other hand can be

sufficiently strong to promote transition or separation of the boundary layer on the model. As a result it can have a marked effect on the heat transfer outboard of the point R on the model surface.

Finally, in Fig. 6.15 the use of the heart-curve method to predict the conditions in the various regions of this interference pattern is illustrated. It is important to note that, just as in the case of Type II interference, we are unable to determine the exact position of Q . This is because of the subsonic patch. All we can say is that Q lies somewhere between the impingement point and the upper sonic point on the bow shock. Consequently, point 6 in Fig. 6.15 is somewhat arbitrary.

The portion of the bow shock below Q

is identical to that formed ahead of the same body in a uniform free stream, at the same Mach number and flow inclination as in region 1.

As the shock impingement point P moves towards the upper sonic line from above, the shock QR weakens and finally vanishes. Q appears only as an inflection point in the bow shock below P . This marks the transition from Type V to Type IV interference.

Type VI interference. This type of interference occurs when the extraneous shock meets the bow shock well above the upper sonic line, as illustrated in Fig. 6.16.

It differs from all the other interference patterns in that there is an expansion from region 2 to region 4.

The portion of the bow shock below the impingement point P is identical with that in a uniform free stream, at the same Mach number and flow inclination as in region 1. Consequently, the location of the point 2 on the $M_1 = 3.66$ heart curve, Fig. 6.17, is known and the entire flow pattern can be established. Neither the expansion nor the shear layer, assuming they meet the surface of the model, appears to have any appreciable effect on the heat-transfer rate. In this case it is the factors we are more usually familiar with, e.g. Reynolds number, roughness, etc., which dictate where transition will occur and what heating we may expect.

As the impinging shock moves downwards relative to the body, the strength of the bow shock immediately below the impingement point increases. This means that point 2 in Fig. 6.17 moves upwards along the left branch of the $M_1 = 3.66$ curve, finally crossing the $M_\infty = 4.6$ curve. When the point 2 is above the $M_\infty = 4.6$ curve it is no longer possible to find an expansion path joining the $M_1 = 3.66$ and $M = 4.6$ curves as shown in Fig. 6.17. The flow then adopts the type V interference pattern we have already described.

Observations by other workers. Of the six different patterns we have described, only two have been identified previously. These are the two simplest, namely Type I, which appears in most textbooks, and Type VI.

However, this is not to say most of them have not been observed before by other workers.

From the table in Chapter 2 we note that nearly all of the workers who have investigated shock impingement have taken schlieren photographs. Unfortunately, the object of the exercise seems to have been to measure the position of the shock-impingement point along the fin, rather than examine the interference pattern in detail. Admittedly, at high Mach numbers and hence low pressures in the test section this can be very difficult.

Since these workers confined their experiments to wedge/fin combinations, only three of the six interference patterns we have described could have occurred. These are Type IV for fins at zero or small angles of sweep, Type V for angles of sweep around 30° and Type VI for larger sweep angles (Fig. 6.18).

Thus Carter and Carr [3], Francis [4] and Siler and Deskins [7] present photographs which are clearly of Type IV. Ray and Falko [9] present photographs of Type V and Beckwith [5], Jones [6] and Bushnell [12] present photographs of Type VI. Nevertheless, of these nine investigators only one, Bushnell, correctly identifies the type of interference he observes, i.e. the relatively simple Type VI. In addition, the presentation of these photographs is often misleading. For example, the photographs which accompany Fig. 6 in Ref. [9] are both of Type V, whereas it is fairly certain that all three of the possible Types IV, V and VI were encountered, since the tests covered a wide range of sweep angles, from $\Lambda = 0^\circ$ to 60° .

Of the workers who have tackled the problem of shock impingement theoretically, Hiers and Loubsky [13] come nearest to a correct interpretation of the interference pattern ahead of a cylindrical fin at zero angle of sweep. Nevertheless, their analysis contains several errors. The pattern they arrive at is shown in Fig. 2.2. This should be compared with the correct pattern in Fig. 6.11. They start out correctly at P and the necessary boundary conditions equating the

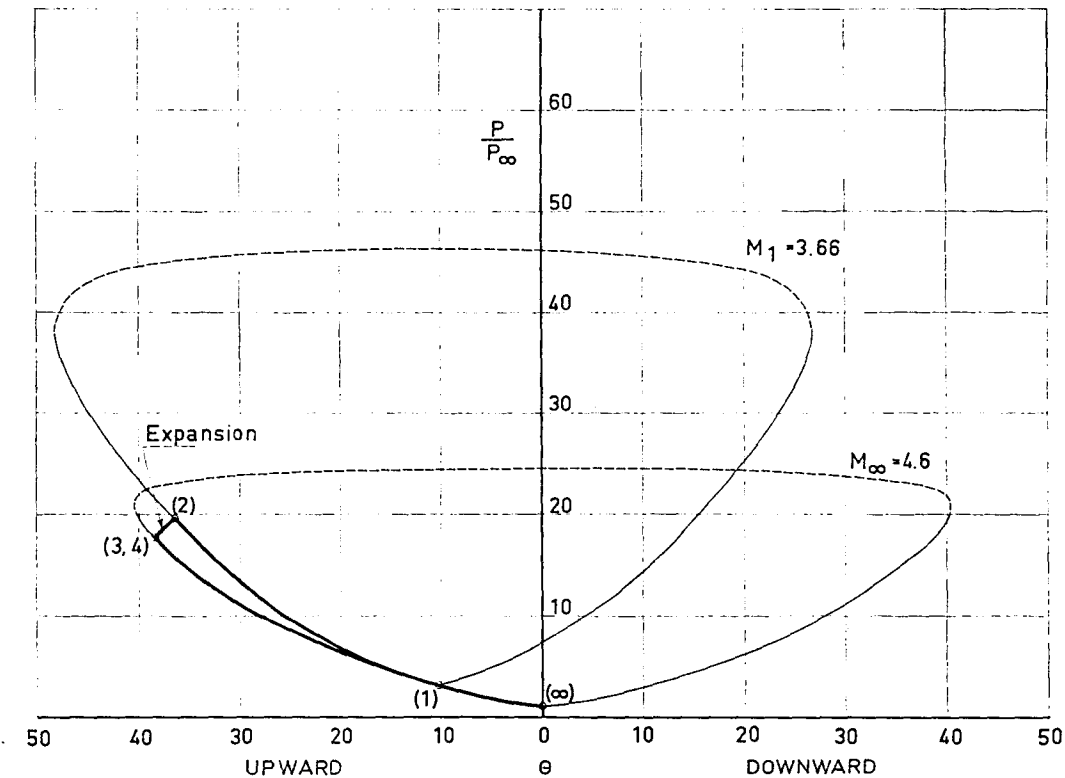


Fig. 6.17. Heart diagram for Type VI interference.

pressure and flow directions in regions 2 and 3 are correctly stated; although, it is not clear whether they carried through the calculations. However, these same boundary conditions must also hold at the points Q , R , T and V but have evidently been forgotten! Thus, the two vortex sheets $PRVY$ and QT are assumed to be straight lines and the shock QR is simply taken as a straight-line continuation of SQ . Not surprisingly, therefore, the flow they arrive at downstream of RQ is incorrect. Hiers and Loubsky also state that an additional shock or expansion can intersect P . Again this is wrong and there is no experimental evidence to support such a hypothesis. Possibly the authors had the Types I and VI interference patterns in mind when they made this remark. It should be pointed out, however, that Hiers' and Loubsky's experimental work was carried out in a high enthalpy shock tunnel at $M = 14$, under which conditions it was well nigh impossible to get printable schlieren photographs.

Fontenot [8] took the easiest way out of all. He simply assumed that the bow shock and the flow conditions within the shock layer are unaffected by the impinging shock. Unfortunately, this is at variance with experiment and consequently his predictions of the width of the zone of increased heating are meaningless.

6.2. Numerical methods

Numerical methods are attractive once it becomes necessary to repeat the same calculation many times, varying, say, the free-stream Mach number or the strength of the impinging shock.

Each of the six patterns described in Section 6.1 may be solved numerically—Types I and VI exactly and the others subject to a certain arbitrariness in fixing absolute lengths, which we have discussed already.

In general we know from the input data which type of interference pattern to expect and need not waste time trying all six possi-

bilities. For impingement below the lower sonic line only Type I or Type II need be considered, for impingement within the subsonic region Type III or Type IV and for impingement above the upper sonic line Type V or Type VI. Often we can find several solutions, one weak pattern (Types I, III and VI) and one or more of the corresponding strong patterns (Types II, IV and V, respectively). In this situation the weak pattern is the most plausible physically. Consequently we always look for a weak pattern first and only if we fail to find a solution of this type do we investigate the possibility of a strong pattern.

As an example we shall consider the calculation of a Type IV interference pattern which was programmed for an IBM 1620 computer.

Calculation of a Type IV interference pattern.

The first step is the calculation of pattern in vicinity of P . Fig. 6.19 shows two possible shock configurations, one with a downward and the other with an upward deflection at P . We shall assume that M_∞ , γ and θ are given.

The pressures in regions 1, 2 and 3 are given by the oblique shock equations as follows (see, for example, Liepmann and Roshko [24] pp. 85-88):

$$P_1 = P_\infty \left[1 + \left(\frac{2\gamma}{\gamma+1} \right) (M_\infty^2 \sin^2 \theta - 1) \right] \quad (6.1)$$

$$= P_\infty g(M_\infty, \gamma, \theta) \quad (6.2)$$

$$P_2 = P_1 g(M_1, \gamma, \beta) \quad (6.3)$$

$$P_3 = P_\infty g(M_\infty, \gamma, \phi). \quad (6.4)$$

Now the first condition that must be satisfied is that the pressure is the same on either side of the shear layer PR , i.e.

$$P_2 = P_3$$

Hence

$$g(M_\infty, \gamma, \phi) = g(M_\infty, \gamma, \theta) g(M_1, \gamma, \beta) \quad (6.5)$$

The flow deflections in regions 1, 2 and 3 are given by the following equations:

$$\alpha = \tan^{-1} \left[\tan \theta \frac{(\gamma-1) M_\infty^2 \sin^2 \theta + 2}{(\gamma+1) M_\infty^2 \sin^2 \theta} \right] \quad (6.6)$$

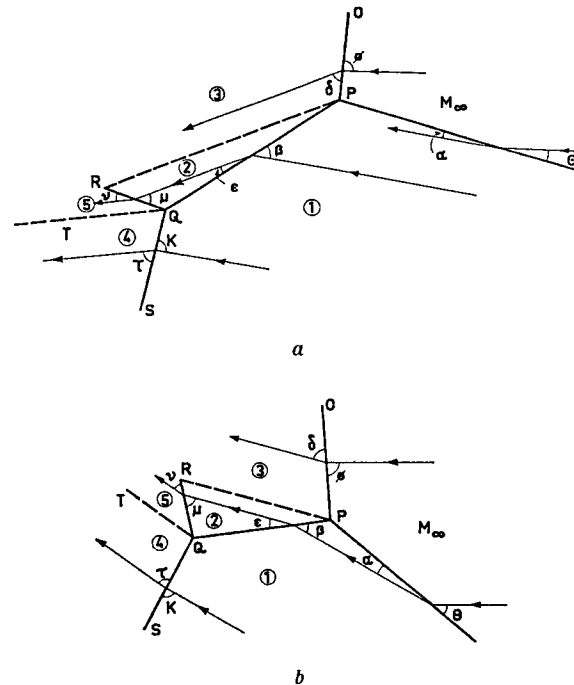


Fig. 6.19. Alternative shock configurations for Type IV interference, allowing for either upward or downward deflection at the impingement point.

$$\alpha = f(M_\infty, \gamma, \theta) \quad (6.7)$$

$$\epsilon = f(M_1, \gamma, \beta) \quad (6.8)$$

$$\delta = f(M_\infty, \gamma, \phi) \quad (6.9)$$

The second condition of parallel flow on either side of PR may be expressed in the form

$$\phi - \delta = \pm [(\beta - \epsilon) - (\theta - \alpha)] \quad (6.10)$$

where the plus sign applies for downward deflections at P (Fig. 6.19 a) and the minus sign to upward deflections at P (Fig. 6.19 b). Thus

$$\phi = \delta \pm [(\beta - \epsilon) - (\theta - \alpha)] \quad (6.11)$$

$$\text{Now } M_1^2 = \frac{1}{\sin^2 \alpha} \cdot \frac{1 + \frac{\gamma-1}{2} M_\infty^2 \sin^2 \theta}{\gamma M_\infty^2 \sin^2 \theta - \frac{\gamma-1}{2}} \quad (6.12)$$

$$\text{or } M_1 = M_1(M_\infty, \gamma, \theta) \quad (6.13)$$

since α is itself a function of M_∞ , γ and θ only (Eq. 6.7).

Similarly, rearranging Eq. (6.5) we get

$$\sin^2 \beta = \frac{1}{M_1^2} \left[1 + \frac{\gamma+1}{2\gamma} \left(\frac{g(M_\infty, \gamma, \phi)}{g(M_\infty, \gamma, \theta)} \right) \right] \quad (6.14)$$

or $\beta = \beta(M_\infty, \gamma, \theta, \phi) \quad (6.15)$

Finally, using Eqs. (6.8), (6.13) and (6.15) we can express ε as a function of M_∞ , γ , θ and ϕ . Thus Eq. (6.11) may be written in the form

$$\begin{aligned} \phi &= f(M_\infty, \gamma, \phi) \pm [\beta(M_\infty, \gamma, \phi, \theta) \\ &- f(M_1(M_\infty, \gamma, \theta), \gamma, \beta) - \theta + f(M_\infty, \gamma, \theta)] \end{aligned} \quad (6.16)$$

or $\phi = F(M_\infty, \gamma, \theta, \phi) \quad (6.17)$

which is the equation we wish to solve.

The existence of a unique shock pattern depends on whether or not Eq. (6.17) has a unique solution for the given M_∞ , γ and θ (ignoring the trivial solution $\phi = \theta$).

The solution is best arrived at by an iteration process. We start by trying to find a solution for a downward deflection at P . If after, say, 20 iterations no solution is found, then we look for a solution involving an upward deflection at P .

The limits for the iteration scheme are easily defined since the shock PO must be at least as strong as the impinging shock and at strongest a normal shock, i.e.

$$\theta < \phi \leq \pi/2 \quad (6.18)$$

The first iteration is then

$$\phi_1 = \frac{1}{2}(\phi_{\text{upper}} + \phi_{\text{lower}}) \equiv \frac{1}{2}(\theta + \pi/2) \quad (6.19)$$

If $\phi_1 < F(M_\infty, \gamma, \theta, \phi_1)$ we reset $\phi_{\text{upper}} = \phi_1$ and if $\phi_1 > F(M_\infty, \gamma, \theta, \phi_1)$ we reset $\phi_{\text{lower}} = \phi_1$.

We then put $\phi_2 = \frac{1}{2}(\phi_{\text{upper}} + \phi_{\text{lower}})$ and the process is repeated until $\phi_n = F(M_\infty, \gamma, \theta, \phi_n)$ within the accuracy required, here $\pm 10^{-4}$ radian. From 10 to 15 iterations were found to be sufficient.

Once ϕ has been found, we may proceed to calculate the shock angles and flow variables in regions 1, 2 and 3 using the oblique shock equations

$$\frac{P_3}{P_\infty} = 1 + \frac{2\gamma}{(\gamma+1)} (M_\infty^2 \sin^2 \phi - 1) \quad (6.20)$$

$$\frac{\rho_3}{\rho_\infty} = \frac{(\gamma+1) M_\infty^2 \sin^2 \phi}{(\gamma-1) M_\infty^2 \sin^2 \phi + 2} \quad (6.21)$$

$$\begin{aligned} \frac{T_3}{T_\infty} &= \left(\frac{a_3}{a_\infty} \right)^2 = 1 + \frac{2(\gamma-1) M_\infty^2 \sin^2 \phi - 1}{(\gamma+1)^2 M_\infty^2 \sin^2 \phi} \\ &\times (\gamma M_\infty^2 \sin^2 \phi + 1) \end{aligned} \quad (6.22)$$

$$M_3^2 = \frac{1}{\sin^2 \delta} \cdot \frac{1 + \frac{\gamma-1}{2} M_\infty^2 \sin^2 \phi}{\gamma M_\infty^2 \sin^2 \phi - \frac{\gamma-1}{2}} \quad (6.23)$$

$$U_3 = M_3 \cdot a_3 \quad (6.24)$$

with similar expressions for regions 1 and 2. These quantities are most conveniently normalized with respect to the corresponding free-stream quantities.

The next step is the calculation of the pattern in the vicinity of Q .

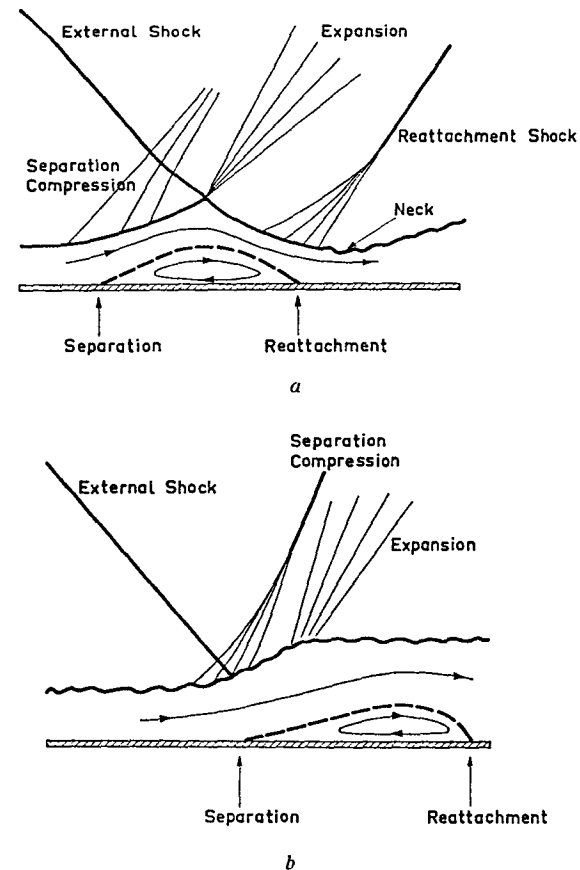


Fig. 7.1. Examples of shock/boundary-layer interactions.
a. Laminar boundary layer b. Turbulent boundary layer.

The above calculation determines M_1 , β and the conditions in regions 1 and 2.

The determination of the shock angles at Q and the flow conditions in regions 4 and 5 is then identical to the procedure described above.

The equation to be solved is now of the form

$$\zeta = F(M_1, \gamma, \beta, \zeta) \quad (6.25)$$

For large values of $\theta \sim 50^\circ\text{--}60^\circ$, depending on M_∞ , M_2 approaches unity and relatively large errors can arise unless the accuracy of the $\zeta_n = F(M_1, \gamma, \beta, \zeta_n)$ test is improved to $\pm 10^{-5}$ radian or better. An arbitrary upper limit for θ was fixed such that the computations were discontinued for $M_2 < 1.1$. If $M_2 < 1$ no Type IV interference solution exists, of course.

Downstream of RQ the further development of the jet is calculated using the method of characteristics. We have already seen the results of two such calculations for $M_\infty = 4.6$ and $M_\infty = 7$ in Figs. 6.12 and 6.13. The excellent agreement with experiment is apparent from both these figures.

7. PREDICTION OF PRESSURE VARIATIONS IN VICINITY OF SHOCK-IMPINGEMENT POINT

7.1. Types I, II and V interference. Shock/boundary-layer interactions

In each of these cases a shock is transmitted through the bow shock layer ahead of the model and impinges on the surface (Figs. 6.4, 6.6 and 6.14). The pressure distribution in the neighbourhood of the impingement point depends not only on the strength of the transmitted shock—which can only be easily predicted for Type I interference—but also on the state of the boundary layer on the model. The essential differences between the interaction of the shock with a laminar or a turbulent boundary layer will be readily apparent from Figs. 7.1 and 7.2.

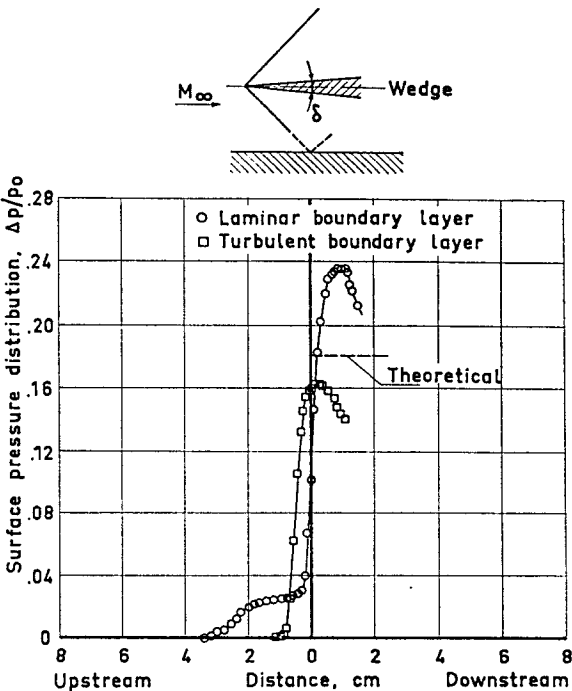


Fig. 7.2. Pressure variation through a shock/boundary-layer interaction, after Liepmann, Roshko and Dhawan [25]. $M_\infty = 1.44$. $\delta = 9^\circ$.

Fig. 7.2 shows typical pressure measurements for turbulent and laminar boundary layers obtained by Liepmann, Roshko and Dhawan [25]. One very striking feature is the extended plateau ahead of the shock in the case of the laminar boundary layer. This pressure rise ahead of the shock will occur whether the boundary layer separates or not. According to Young [26], such pressure diffusion may extend up to 100 boundary-layer thicknesses upstream of the shock when the boundary layer is laminar but only about 10 boundary-layer thicknesses when the boundary layer is turbulent. This is on account of the fact that the subsonic part of the boundary-layer is thinner for a turbulent than for a laminar boundary layer. Another important point to notice is that the pressure rise through the turbulent interaction region is lower than that predicted by inviscid theory (see also Seddon [27] for further evidence of this), whereas the pressure rise through the laminar interaction region exceeds that predicted by inviscid theory.

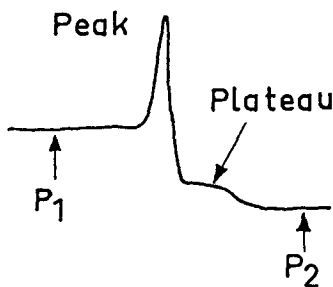
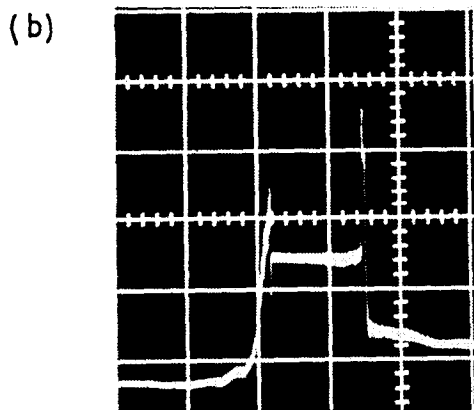
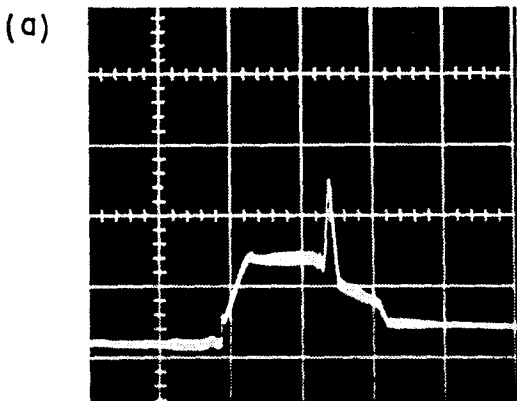


Fig. 7.3. Pressure records showing a brief plateau following the peak pressure. *a.* Plateau probably due to Type II interference. *b.* Plateau due to Type III interference. $M_\infty = 4.6$. $\xi = 15^\circ$.

The static pressure measurements described in Section 5.1 are incapable of resolving any details of the pressure rise through a shock/boundary-layer interaction region

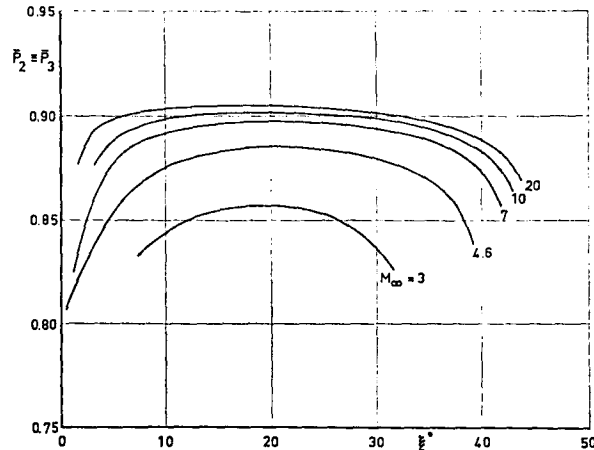


Fig. 7.4. Pressure on either side of free-shear layer (Type III interference) as a function of ξ for various free-stream Mach numbers. $\gamma = 1.4$.

owing to the coarse hole spacing, as we can see from Fig. 5.2F (Type V interference), Fig. 5.5A (Type II interference) and Fig. 5.6B (Type I interference).

Since the flow ahead of the transmitted shock for Types II and V interference is barely supersonic for $M_\infty = 4.6$, the total pressure rise measured on the surface of the model (Figs. 5.2F and 5.5A) is fairly small. Consequently, the criterion for separation of a turbulent boundary layer (pressure ratio across the shock > 1.8 [28]) is not always satisfied for Types II and V interference at this Mach number.

The measurements with the transducer in the sphere (Section 5.2) afford us a better opportunity to examine the effects of pressure diffusion ahead of the shock, since the resolution is much better (~ 1 mm). Providing that the boundary layer is laminar, what we expect to see is a brief pressure plateau following the peak (i.e. on the low pressure side of it). This, then, is a possible explanation of the pressure record shown in Fig. 7.3a.

Of course, we must be wary when interpreting such pressure records since the interference pattern is constantly changing during the traverse. The shock/boundary-layer interaction point is well below the pressure tap at the time the plateau is recorded. For this reason we cannot recon-

struct the exact pressure variation through the interaction region as it would be on a stationary model. Only for small displacements from the interaction region does the pressure record we obtain reflect this variation with any accuracy.

In view of the difficulties of determining the strength of the transmitted shock, no attempt was made to calculate the total pressure rise through the interaction region. It is evident, however, that the peak pressure generated by those types of interference involving shock-boundary interactions is small compared to that generated by either Type III or Type IV interference.

Finally, we note that even Type III interference (Fig. 6.10) involves a shock/boundary-layer interaction at the attachment point. The free-shear layer is turbulent at $M = 4.6$ but it is very much thicker than the boundary layer elsewhere on the model. In addition, the flow in region 3 is subsonic, so a noticeable pressure rise on the subsonic side of the attachment point is to be expected in any case. This is confirmed by pressure records obtained with the transducer in the sphere (Fig. 7.3b). It is also evident in certain of the static pressure measurements on the underside of the cone (Fig. 5.6C) where the attachment angle is very shallow.

7.2. Type III interference. The attaching shear layer

In order to predict the peak pressures associated with Type III interference (see Fig. 6.8), we need to know the pressure P_2 , Mach number M_2 , and flow inclination η in region 2. This in turn gives us the angle the shear layer PR makes with the surface of the model and hence the pressure rise through the attached shock RQ may be calculated.

Fig. 7.4 shows $\bar{P}_2 \equiv \bar{P}_3$ the pressure on either side of the free-shear layer (normalized with respect to the pitot pressure P_{20} in the free stream) as a function of ξ for various free-stream Mach numbers. \bar{P}_2 is virtually constant over a wide range of ξ .

However, the Mach number M_2 (Fig. 7.5)

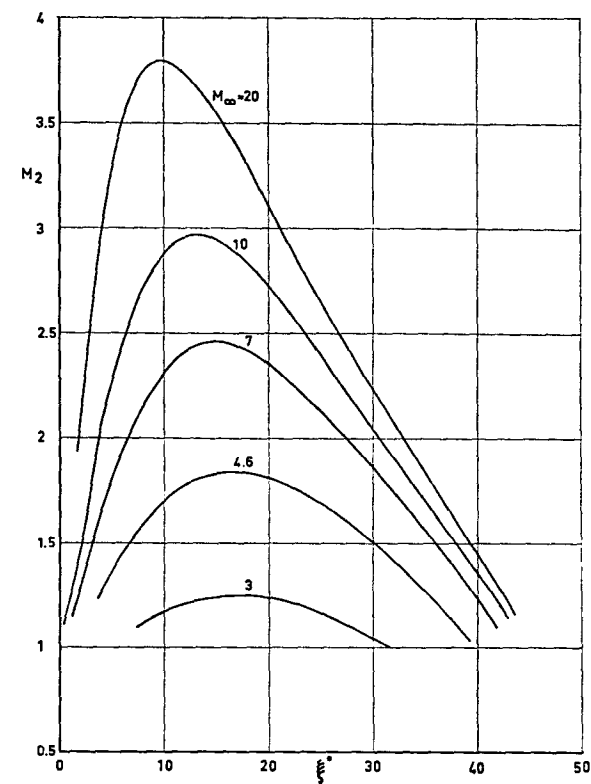


Fig. 7.5. M_2 as a function of ξ for various free-stream Mach numbers. $\gamma = 1.4$ (Type III interference).

and the flow inclination η (Fig. 7.6) are both strongly dependent on ξ . For a given M_∞ and small ξ , both M_2 and the attachment angle (the angle through which the flow must be deflected at the point R) increase with increasing ξ . This means that the peak pressure generated by the attachment shock RQ , at a given point on the model, increases rapidly at first as the strength of the impinging shock (i.e. ξ) increases. The highest peak pressures are generated as M_2 attains a maximum, for ξ between 10° and 18° depending on M_∞ . Any further increase in ξ beyond this point results in a decrease in the peak pressure.

Another point worth noting in Fig. 7.5 is that since M_2 increases with increasing free-stream Mach number, M_∞ , the peak pressure increases monotonically with M_∞ for a given ξ .

In Figs. 5.9–5.13 we are able to compare the theoretical peak pressure variation with x/r , calculated for Type III interference on a

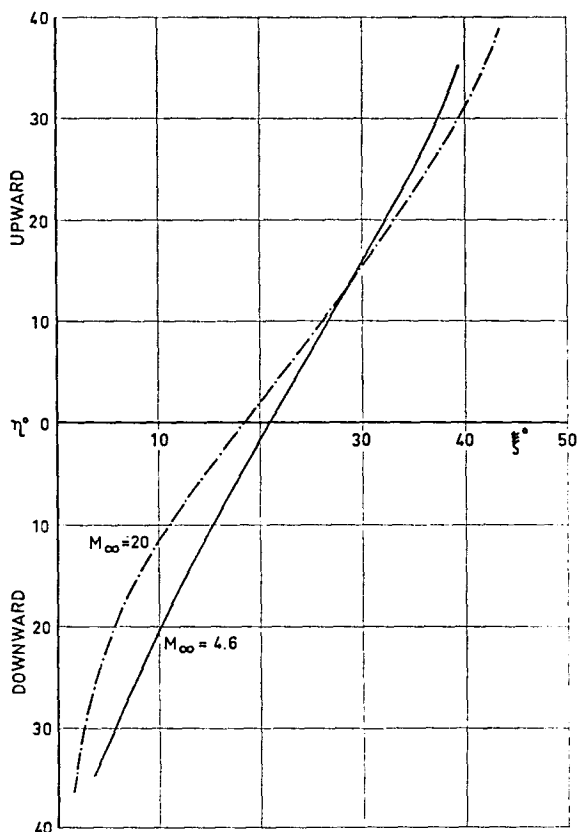


Fig. 7.6. Flow inclination η in region 2 as a function of ξ . $\gamma = 1.4$ (Type III interference).

sphere, with the experimentally observed pressures at $M_\infty = 4.6$ and 7. At $M_\infty = 7$ the agreement is excellent but the measured pressures fall well below the theoretical curves at $M = 4.6$.

What is surprising is not the poor agreement at $M = 4.6$ but rather the excellent agreement at $M_\infty = 7$, since the theory in no way takes into account viscous effects. At $M_\infty = 4.6$ the shear layer is certainly turbulent and hence very thick, as can be seen from Fig. 6.8. The displacement due to the shear layer means that the effective attachment angle is reduced. In this case the discrepancy between the predicted and actual attachment angles is estimated to be about 5° , judging from schlieren photographs. This implies that the pressure rise will also be reduced or the experimental curve displaced towards smaller x/r by an amount ~ 0.1 , as is the case. These conclusions are strongly supported by pressure measure-

ments made by Finley [29], who has examined the reattachment of a turbulent shear layer on a spiked hemisphere (Fig. 8.6d).

It also follows from the discussion of shock/boundary-layer interactions in Section 7.1 that the pressure rise through the attachment shock will be smaller than that indicated by inviscid calculations, if the shear layer is turbulent.

At $M = 7$ the agreement with theory is much better. For $\xi = 5^\circ$ the experimentally measured pressures even exceed the predicted pressures over most of the curve. This may be partly attributable to experimental error but it also suggests that the shear layer is laminar upto the attachment point since this would imply smaller displacement and

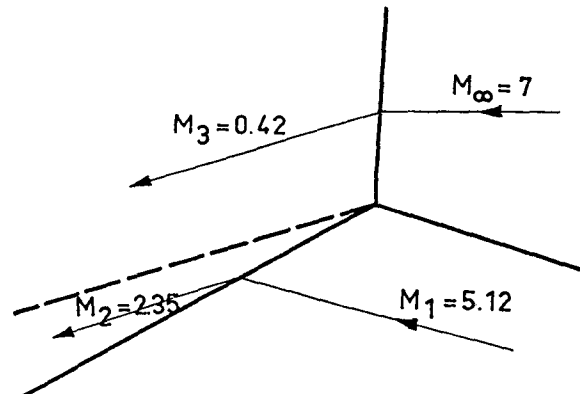
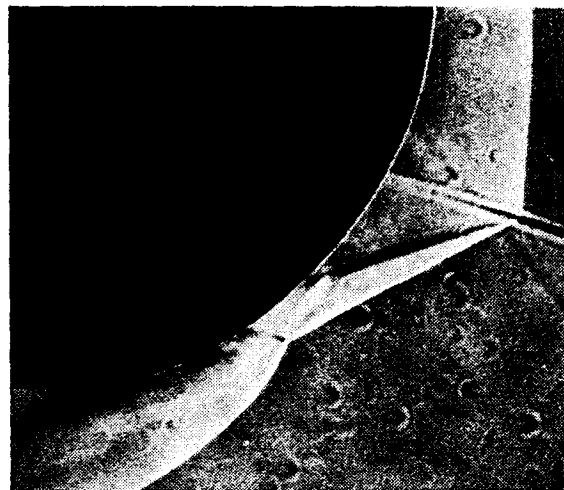


Fig. 7.7. Type III interference at $M = 7$, $\xi = 10^\circ$, compared with predicted pattern. Shear layer appears to be laminar (cf. Fig. 6.10.).

a higher pressure rise through the shock/boundary-layer interaction region. Such a hypothesis is supported by the photograph of Type III interference at $M = 7$ shown in Fig. 7.7.

Finally, in Figs. 5.9–5.13 we are able to compare the severity of the various types of interference on a sphere. The highest pressures are generated by Type IV interference (small x/r) and the lowest by Types I and II (large x/r), with Type III bridging the gap between them.

7.3. Type IV interference. The supersonic impinging jet

It is amply clear from the various pressure measurements that have been presented, that this is the type of interference that generates the highest peak pressures, whatever the shape of the model.

One very interesting result obtained from the numerical calculations described in Chapter 6 is a prediction of the maximum peak pressure that can be generated for a given free-stream Mach number and strength of the impinging shock. We know from experiment that this occurs when a jet is formed and impacts the surface of the model normally. If $M_5 > 1$ we assume that the jet impacts via a normal shock from condition 5 (Fig. 6.11). In other words, the maximum peak pressure is simply assumed to be equal to the pitot pressure P_{60} in region 5, irrespective of whether the flow is supersonic or subsonic. This is a reasonable approximation provided M_5 is not too large. (For $M_\infty < 20$ and $\gamma = 1.4$, calculations show that $M_5 < 2.6$ for all ξ .)

$$P_{60} = P_5 \left(1 + \frac{\gamma - 1}{2} M_5^2 \right)^{\gamma/(\gamma-1)} M_5 < 1 \quad (7.1)$$

$$P_{60} = \frac{P_5 \left(\frac{\gamma + 1}{2} M_5^2 \right)^{\gamma/(\gamma-1)}}{\left(\frac{2\gamma}{\gamma + 1} M_5^2 - \frac{\gamma - 1}{\gamma + 1} \right)^{1/(\gamma-1)}} M_5 > 1. \quad (7.2)$$

Fig. 7.8 shows P_{60}/P_{20} as a function of ξ , the plate angle or deflection through the impinging shock, for $M_\infty = 3, 4.6, 7, 10$ and

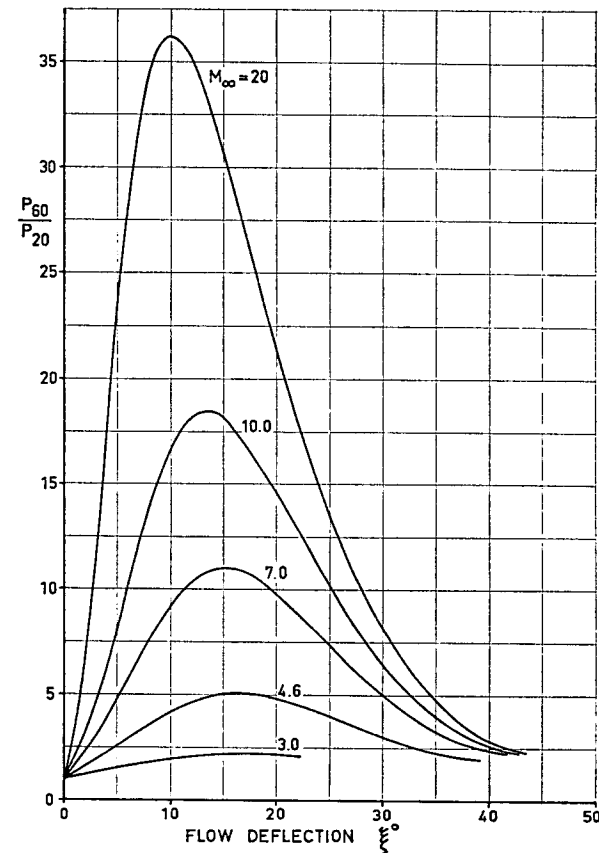


Fig. 7.8. Maximum impact pressure P_{60} generated by jet (Type IV interference) as a function of ξ , for various free-stream Mach numbers. $\gamma = 1.4$.

20 and $\gamma = 1.4$. P_{20} denotes the pitot pressure in the free stream, given by

$$P_{20} = \frac{P_\infty \left(\frac{\gamma + 1}{2} M_\infty^2 \right)^{\gamma/(\gamma-1)}}{\left(\frac{2\gamma}{\gamma + 1} M_\infty^2 - \frac{\gamma - 1}{\gamma + 1} \right)^{1/(\gamma-1)}}. \quad (7.3)$$

We see that P_{60} first increases with ξ , reaching a maximum between $\xi = 10^\circ$ and 20° , depending on M_∞ , and then decreases again. This behaviour is confirmed for ξ upto 15° at $M = 4.6$ and ξ upto 10° at $M = 7$, measurements not being possible beyond this in the present facility. P_{60}/P_{20} also increases with increasing Mach number as we can see in Fig. 7.8. Again this is confirmed experimentally. Note that P_{60}/P_{20} tends to unity for both very weak ($\xi = 0$) and very strong ($\xi \approx 45^\circ$) shocks, as we should expect.

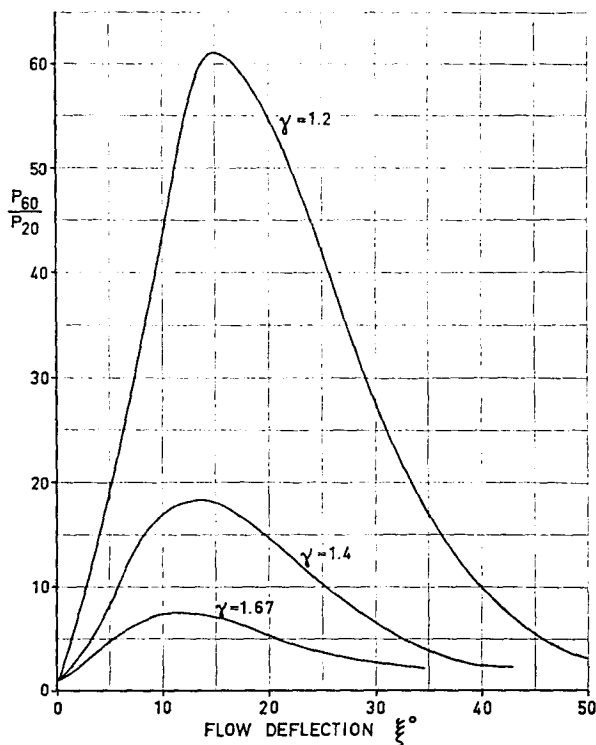


Fig. 7.9. Maximum impact pressure generated by jet (Type IV interference) as a function of ξ , for various γ . $M_\infty = 10$.

In Figs. 5.9–5.13, P_{60}/P_{20} is indicated by a dashed line, which denotes the theoretical upper limit for P_{peak} . We see that the agreement with the experimental results is very good. The discrepancy is the order of 6–10% and is partly attributable to pressure losses in the jet. Anderson and Johns [54] have measured the pressure decay along the axis of a free supersonic jet and their results are in good general agreement with the losses we measure here for $\Delta x/l \sim 5$, where Δx and l are the width and length of the jet, respectively.

At high Mach numbers in air, where real gas effects are of importance, γ will be appreciably different from 1.4. Thus, at Mach 10 at 50,000' altitude the stagnation temperature is approximately 3300°K, which means a γ of about 1.2. Fig. 7.9 illustrates the effect of varying γ , keeping the free-stream Mach number fixed ($M_\infty = 10$). P_{60}/P_{20} is clearly a very strong function of γ .

Unfortunately, it was not possible to

check these predictions experimentally in any of FFA's existing wind tunnels (see Section 8.3). However, it does mean that one must be cautious when comparing results from high enthalpy facilities (shock tunnels, etc.) and 'cold' facilities.

In Fig. 7.10 we have sketched the flow one might expect in the neighbourhood of the jet-impingement point, together with the corresponding pressure distribution which would be measured on the model. Secondary peaks and troughs in the pressure distribution are evident as a result of the system of expansion and compression waves which is set up between the wall and the edge of the jet, as the jet spills outwards. This is in excellent agreement—at least qualitatively—with the pressure records obtained using the transducer in the sphere described in Section 5.2. The troughs following the peaks in Fig. 5.8 are evidently due to the expansion which meets the surface at the point C , Fig. 7.10, the pressure orifice being slightly above the centre line of the jet when the trough is recorded. The static measurements shown in Figs. 5.2–5.6 cannot be expected to reveal such fine

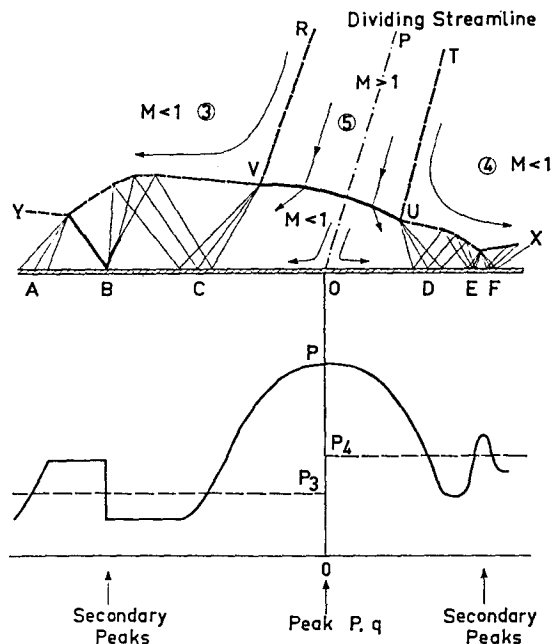


Fig. 7.10. Sketch of jet-impingement region (Type IV interference).

structure, of course, owing to the relatively wide spacing of the holes.

A detailed analysis of the jet-impingement region is extremely difficult, even if we assumed for a moment that we could calculate the width of the jet and the angle with which it impinges on the surface, which in fact we cannot! Some consolation can be derived from a recent study of the impingement of a supersonic jet on a flat plate in still air, carried out by Henderson [30]. In this study the width, Mach number and impingement angle of the jet could be controlled by the experimenter. The additional complications caused by the flow external to the jet and the pressure differential across the jet, which we are faced with, were also absent. Nevertheless, Henderson was still limited to a qualitative, though excellent, description of the impingement process. The stumbling block is, of course, the detached shock UV and the subsonic region at the impact point.

Of especial interest are the values of $C_{p_{\max}}$ and $C_{p_{\min}}$ measured on the flat plate by Henderson, particularly since the Mach numbers he investigated (1.8–2.14) are nearly the same as those in the jet we need to study. He defines

$$C_p = \frac{P_b - P_a}{\frac{1}{2}\gamma P_a M_j^2}$$

where P_b = plate pressure

P_a = ambient pressure

M_j = Mach number in jet.

Fig. 7.11 shows $C_{p_{\max}}$ and $C_{p_{\min}}$ as a function of impingement angle, θ . We see that the maximum pressures are generated for nearly normal impact, remaining fairly constant out to $\theta = 50^\circ$, and then falling with further decrease in impingement angle. It is evident from Figs. 5.9–5.13 that a similar variation occurs for Type IV interference, where a change in x/r is equivalent to a change in jet-impingement angle. Unfortunately, we cannot determine the impingement angle as a function of x/r and can only make a very crude estimate from schlieren photographs. The only thing we

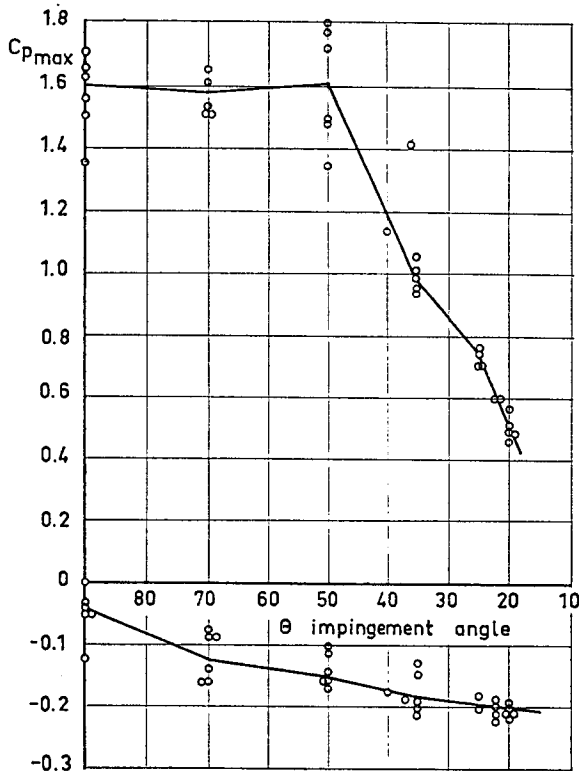


Fig. 7.11. $C_{p_{\max}}$ and $C_{p_{\min}}$ for an impinging jet on an inclined flat plate, after Henderson [30].

can compare directly with Henderson's results is $C_{p_{\max}}$ for the case where

$$C_{p_{\max}} = \frac{(P_{\text{peak}})_{\max} - P_5}{\frac{1}{2}\gamma P_5 M_5^2} = \frac{P_{\infty} - P_5}{\frac{1}{2}\gamma P_5 M_5^2}$$

Some typical values are shown below.

M_∞	ξ	M_5	$C_{p_{\max}}$	M_∞	ξ	M_5	$C_{p_{\max}}$
4.6	6.14	1.15	1.38	7.0	6.37	1.54	1.54
	10.70	1.26	1.45		11.11	1.71	1.60
	14.76	1.26	1.45		13.52	1.70	1.59

Finally we note that the pressure distribution will be sensitive to viscous effects. A high level of turbulence in the jet is evident from schlieren photographs and this will modify the velocity distribution in the jet prior to impingement. In addition, we can expect interactions between the boundary layer on the model and the shocks within the jet to alter the surface pressure distribution from that calculated on the basis of in-

viscid flow. When the jet is long and thin it will be fully turbulent at the point at which it meets the model and have diffused to the extent that the structure of the jet will in no way resemble that we have drawn in Fig. 7.10. Judging from measurements of the pressure decay in the axis of a supersonic jet exhausting into quiescent air, carried out by Anderson and Johns [54], the pitot pressure P_J remains fairly constant up to $l_{\max}/\Delta x \sim 5-10$, depending on the Mach number, thereafter falling off rapidly with l like

$$\frac{P_J}{P_{\infty}} \approx \left(\frac{l}{l_{\max}} \right)^{-2.3}.$$

Thus, when $l/\Delta x = 20$ the pitot pressure has fallen to 1/10 of its original value for $M_J = 1.84$. The jet can therefore no longer be supersonic.

This rapid decay in the jet explains the very sharp fall-off in the peak pressure on the sphere, for impingement above the point where the peak pressure is a maximum (Figs. 5.9-5.13), since not only does the impingement angle decrease but the jet becomes thinner and thinner as the impingement point moves up the face of the model. For impingement above the centre line the pressure decreases from P_1 to P_2 through the jet impingement region without any peak being observed (5.8a).

Henderson notes that strong oscillations (so-called Hartmann oscillations) were set up in the jet for Mach numbers between 2.0 and 2.7. On the basis of this criterion such oscillations would not have been expected in the present experiments and indeed the jet was remarkably stable. However, it is evident from Fig. 7.5 (the Mach number in the jet $M_J \leq M_2$) that this possibility cannot be excluded for higher free-stream Mach numbers.

8. PREDICTION OF HEAT-TRANSFER VARIATIONS IN VICINITY OF SHOCK-IMPINGEMENT POINT

We have already touched upon the different mechanisms whereby increased heating

occurs, when discussing the various types of interference in Chapter 6. There are three such mechanisms and they may be grouped as follows:

8.1. Heating attributable to shock/boundary-layer interactions

Local peak heating associated with Types I, II and V interference can in each case be attributed to a shock/boundary-layer interaction. Any overall increase downstream of the impingement point can usually be traced to transition.

The magnitude of the heating and the heat-transfer distribution through the interaction region will depend not only on the state of the boundary layer but on the strength of the shock.

Both Young [26] and Schlichting [31] discuss the various interactions that can arise. According to Schlichting, when the shock is weak and the Reynolds number is very small, the boundary layer remains laminar throughout. Increasing the Reynolds number causes transition to occur at the point of impingement. When the shock is strong and the Reynolds number is small, the laminar boundary will separate ahead of the shock owing to pressure diffusion; it may also undergo transition ahead of the shock. When the Reynolds number is large enough, transition in the boundary layer occurs ahead of the shock, whether the boundary layer has separated or not.

Young distinguishes the following cases:

a. The approaching boundary layer is laminar and remains so beyond the shock without separation. This is possibly the case in Fig. 6.6c. The transmitted shock QR , although nearly normal, does not produce a large pressure rise through the impingement point on the model surface, since the flow in region 3 is barely supersonic.

b. The approaching boundary layer is laminar, but separates because of the adverse pressure gradient and then returns to the surface in either a laminar or turbulent state. This is the most likely alternative at low Reynolds numbers for Type I interference (Fig. 6.4) since the Mach number in

region 3 is higher than for either Type II or Type V interference and hence stronger shocks are possible. We see examples of this in Figs. 6.4b and c. In Fig. 6.4b separation and transition occur well ahead of the impingement point which means that the interaction region is very broad.

No simple criterion for predicting separation exists at present, although we shall discuss some tests for separation later, based on observed pressure and heat-transfer distributions through the interaction region.

c. The approaching boundary layer is laminar and separates completely from the surface ahead of the shock and does not reattach itself to the surface. This appears to be what happens in Fig. 6.6b. It is interesting to compare this with Fig. 6.6c where separation does not occur. Evidently the Mach number in region 3 is higher in Fig. 6.6b than in Fig. 6.6c and hence the shock RQ is that much stronger. Note the λ -limb in Fig. 6.6b, which may be a peculiar feature of this interaction. A similar example is presented by Schlichting [31].

d. The approaching boundary layer is turbulent and does not separate from the surface. According to Fage and Sargent [28] turbulent boundary layers do not separate for a pressure ratio across the shock which is less than 1.8, which corresponds to a Mach number $M_3 < 1.3$ for a normal shock. However, a more recent study by Hamitt [32] showed that pressure ratios from 1.8 to 5.5, depending on the Mach number, could be sustained without separation taking place. A better criterion, Hamitt suggests, is the boundary-layer parameter

$$K = \bar{U}/U_e$$

where \bar{U} = average velocity in the boundary layer (momentum/mass)

U_e = free-stream velocity.

For the cases he examines K_{sep} varies between 0.79 and 0.85.

e. The approaching boundary layer is turbulent and separates from the surface.

A detailed study of these five alternatives is beyond the scope of the present study.

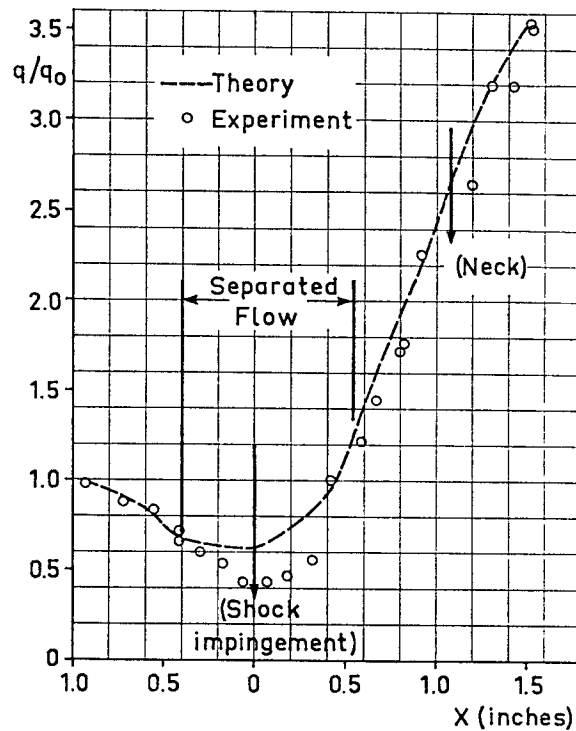


Fig. 8.1. Typical heat-transfer distribution through a shock/laminar boundary-layer interaction on a flat plate. $M_\infty = 10$. After Holden [34].

Indeed each is sufficiently difficult in itself to merit a separate investigation. In particular one would like to design an experiment using larger models in which it was possible to vary the strength of the transmitted shock and the Reynolds number over a wider range than was possible with the present experimental set up.

Recent studies of the heat transfer through a shock/boundary-layer interaction region on a flat plate include those by Kelley [36], Martellucci and Lipfert [37], Bogdonoff and Vas [33] and Holden [34, 35]. These studies are primarily concerned with laminar boundary layers. Only Kelley attempts to measure the heat-transfer distribution through a turbulent boundary-layer interaction. However, Kelley expresses some doubts as to whether he really succeeded in producing a fully turbulent boundary layer. The experimental evidence is inconclusive and we can safely say that our knowledge of turbulent interactions is poor at the present.

Holden [34], among others, tackles the laminar interaction problem using an integral method based on the laminar flow model shown in Fig. 7.1a. These calculations predict pressure and heat-transfer distributions through the interaction region in good agreement with experimental data obtained at Mach 10 (Fig. 8.1). A similar study by Martellucci and Lipfert [37] indicates equally good agreement even at $M = 2$ and 5.4, which is possibly more relevant to the present study. Note, however, that Martellucci and Lipfert calculate skin friction as opposed to heat-transfer rates. The main features which emerge from these studies and which are of immediate interest to us here may be summarized as follows:

(i) The maximum heat-transfer rate (i.e. q_{peak}) through the interaction region increases with increasing strength of the impinging shock. An increase in the local heating by a factor of 10 can easily be achieved. This is in agreement with the measurements on the blunted cone shown in Fig. 4.13, since increasing ξ increases the strength of the transmitted shock in Type I interference.

(ii) There is a marked dip in the heat-transfer rate immediately upstream of the impingement point, due to a thickening of the boundary layer, and coinciding with the pressure plateau we have already described in Section 7.1. The shape of this dip is important since it is a criterion as to whether separation has occurred. If the boundary layer has not separated the dip has a crisp-like or V profile. Once the boundary layer separates the dip has a rounded or U profile. This region of reduced heat transfer broadens as the strength of the impinging shock increases but the heat-transfer rate remains fairly constant at about 0.4 of the flat plate value upstream of the separation. Fig. 8.1 shows a typical heat-transfer distribution through a laminar interaction region.

For the tests on the hemisphere and the flat-faced cylinder the heating due to shock/boundary-layer interactions was almost negligible compared with that due to the at-

taching shear layer (Type III) and the impinging jet (Type IV).

However, this is not always the case, as is evidenced by the tests on the blunted cone. Here Type I interference on the underside of the cone gives rise to very high heat-transfer rates, comparable with those caused by Type III and Type IV interference. This is very well illustrated by the oscilloscope record shown in Fig. 8.2. The first peak is due to Type III interference and the second to Type I interference. (We have already described the reason for the proximity of these two peaks in Chapter 4.) The presence of the first peak can lead to difficulties in interpreting the heat-transfer record, in particular the determination of the heat-transfer rate downstream of the shock/boundary-layer interaction region. (Of course, if one wants to study the effects of Type I interference only, one can easily eliminate Type III interference by making measurements on a sharp cone instead of the blunted cone.) Nevertheless, in the particular example we have chosen, Fig. 8.2, the peaks are well separated. Moreover, the shape of the second peak can be expected to correspond fairly closely to the heat-transfer distribution through a shock/boundary-layer interaction region that would be measured on a stationary model. Note that this is not the case for records obtained using the sphere, as we have explained in Section 7.1 when discussing the pitfalls of interpreting pressure records. The difference in the case of the cone—or a wedge for that matter—is that impingement almost anywhere on the underside will produce much the same interference pattern, since the strength of the bow shock is constant, or nearly so, over a larger distance. Consequently, the interference pattern (Fig. 6.4) and in particular the strength of the transmitted shock and the angle it impinges on the model surface is fairly constant for large displacements of the model relative to the shock.

Two things should be pointed out in Fig. 8.2. One is the dip in the heat-transfer rate upstream of the impingement point (i.e. immediately following the second peak).

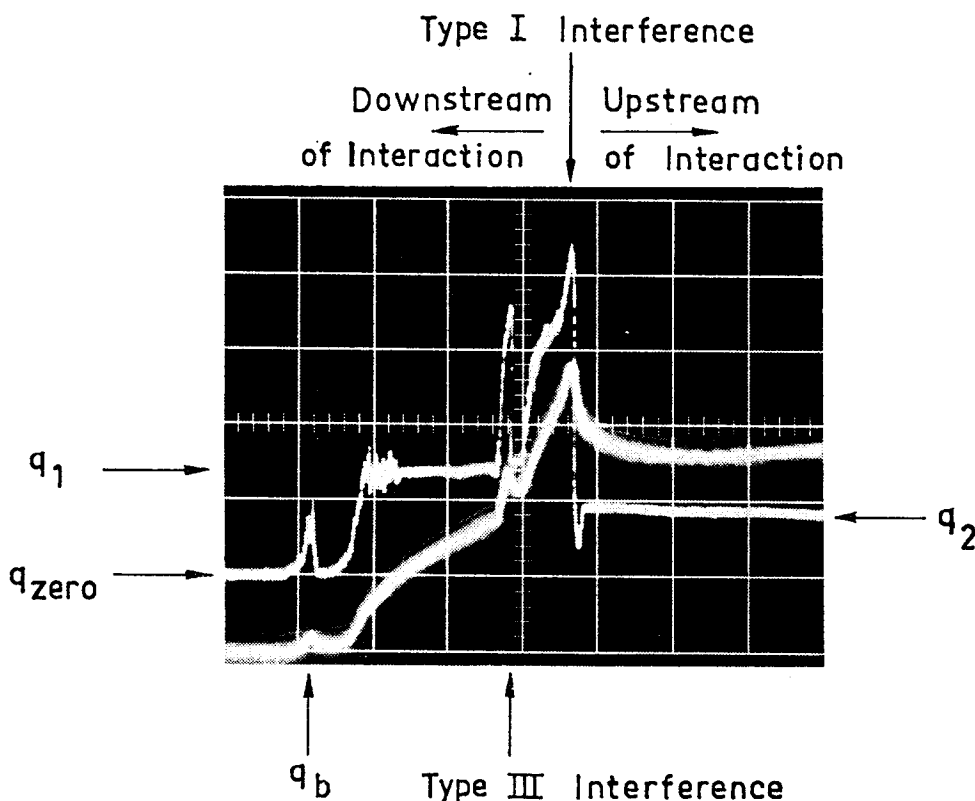


Fig. 8.2. Heat transfer (upper trace) and surface temperature (lower trace) for a blunted cone. $M_\infty = 4.6$. $\xi = 5^\circ$. $x/r = 1.535$ on underside.

Note that this is about 0.4 of the steady value well upstream of the interaction region, which agrees very well with what other investigators have measured. Note also that the dip is much narrower than the peak in this particular example, which would indicate that the separation bubble is quite small, if indeed separation has taken place. Schlieren photographs indicate that it has, but it would be going too far to suggest we could differentiate between a *U*-shaped and a *V*-shaped dip from Fig. 8.2!

There is no ambiguity about the other point we want to make, however, and that is the extremely abrupt rise in the heat-transfer rate on the upstream side of the impingement point compared with the more gradual fall-off on the downstream side. Again this agrees with what other investigators find.

This behaviour is more readily appreciated if we look at Fig. 8.3. Fig. 8.3*b* shows the underside of a paraboloid model, which has been coated with temperature-sensitive

paint, after about 10 seconds exposure to an impinging shock. Dark regions (blue in the original) mark areas of high heat transfer and light regions (pink in the original) mark areas of low heat transfer. (We shall say more about this technique in Chapter 9.)

The nose is quite clearly an area of high heat transfer, as we should expect. However, what is of interest here is the second area of high heat transfer below the nose, namely that bounded by the sharp parabolic contour. It is this second region which is due to the shock/boundary-layer interaction (Type I interference). Note the extremely abrupt rise in the heat-transfer rate on the upstream side of the interaction region (i.e. nearest the nose) as opposed to the more gradual fall-off downstream of the interaction region (i.e. nearest the base). This is exactly what is predicted on the basis of the heat-transfer rate measurements on the blunted cone (Fig. 8.2).

A further example of the temperature-

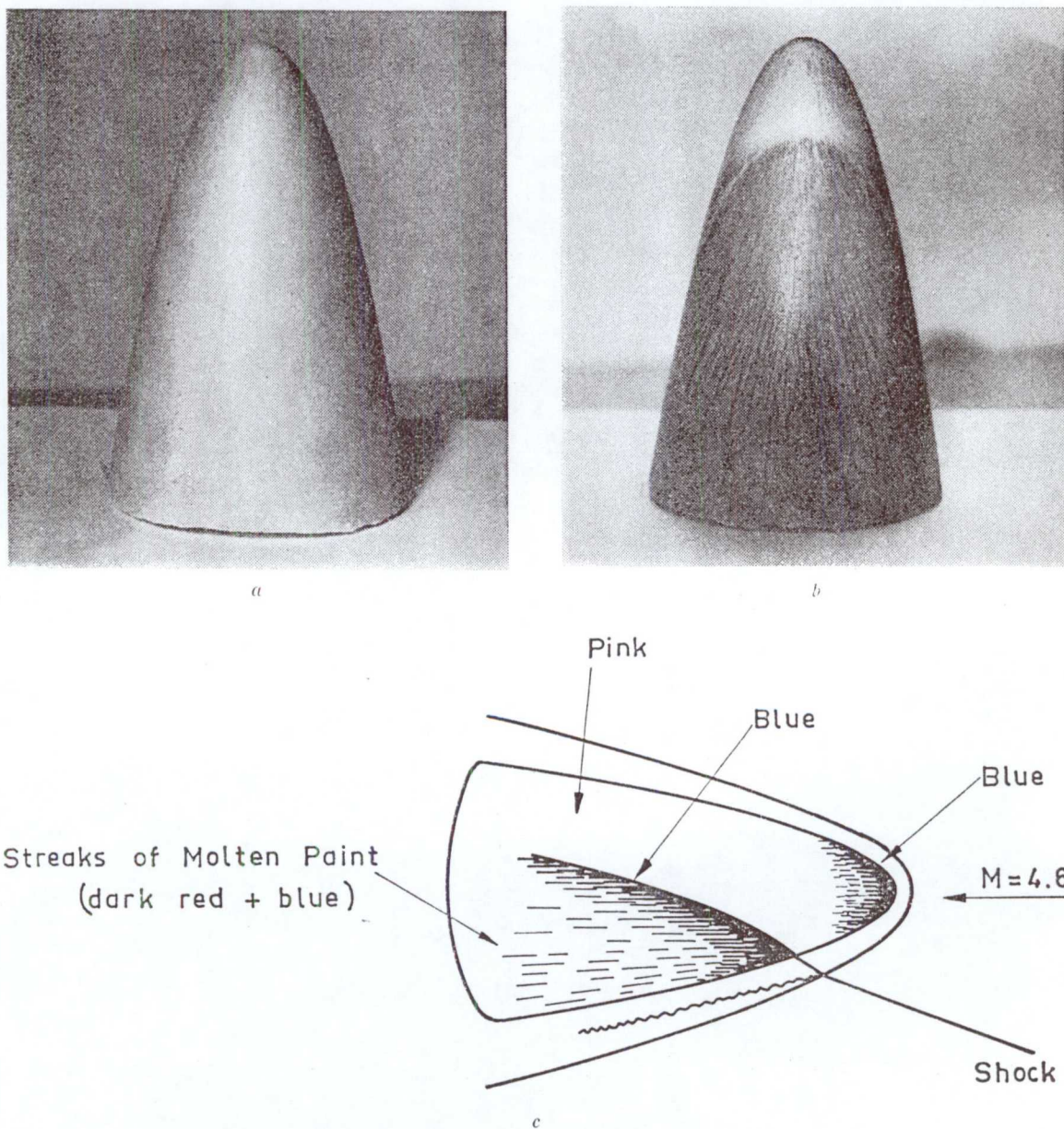


Fig. 8.3. Rubber model coated with Detectotemp. *a*. Prior to run. *b*. underside after 10 sec run at $M = 4.6$. $\xi = 5^\circ$.
c. Type I interference, showing location of regions of high heat transfer.

sensitive paint technique to study Type V interference on a cylindrical fin is shown in Fig. 8.4. Three hot spots are evident. These occur around the bottom edge of the fin (as expected for a sharp leading edge), at the point where the transmitted shock meets the fin and outboard of the point where the vortex sheet, formed by the coalescence of the shear layer and the jet (see Fig. 6.14), meets the fin. Note that the heating due to

the shock is more severe than the heating due to the vortex sheet. For this reason we have grouped Type V interference with the shock/boundary-layer interactions. The heating due to the vortex sheet should not be ignored, however.

At $\xi = 5^\circ$ Type V interference had little or no noticeable effect on the heat transfer on the blunted cone. At $\xi = 15^\circ$, however, large peaks were recorded by films on the upper-

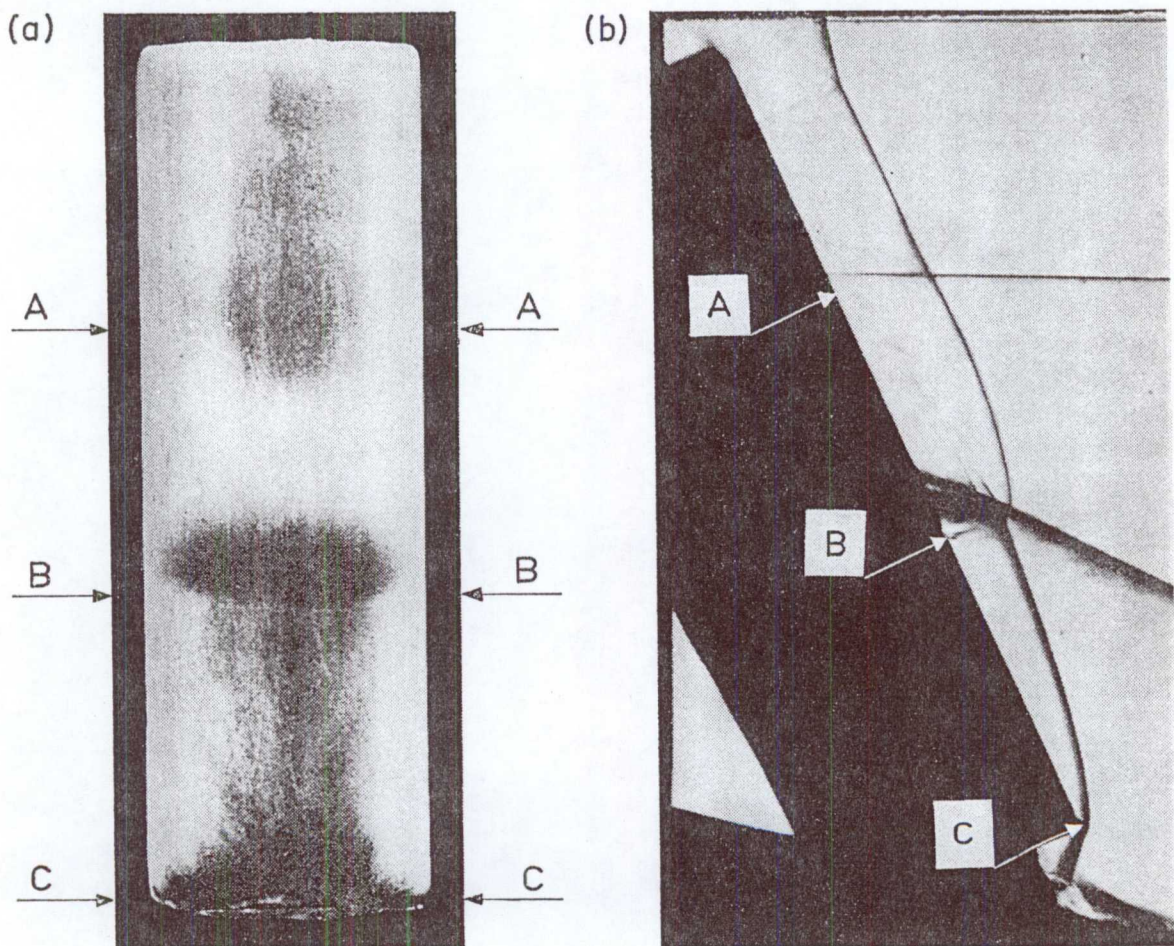


Fig. 8.4. a. Cylindrical fin coated with Detectotemp after 6 sec run at $M = 4.6$, $\xi = 15^\circ$. b. Corresponding schlieren photograph locating regions of high heat transfer. Type V interference.

side of the model (Fig. 8.5). The first is due to interference from the boundary layer on the plate—this is also present at $\xi = 5^\circ$. The second is thought to be caused by the shock/boundary-layer interaction associated with Type V interference. Unfortunately, no schlieren photographs coincident with the second peak were obtained. Consequently, it is not possible to state categorically that this peak is due to Type V interference. Interpretation of the records from films on the upperside of the model is also complicated by the presence of a separation near the nose (it is this separation which gives rise to dips on some of the records, e.g. Fig. 4.7d).

8.2. Heating attributable to an attaching shear layer

8.2.1. Analogy with separated flows. The peak heating associated with Type III interference is due to the attachment of a free-shear layer. A survey of recent separated flow studies reveals that high heat-transfer rates in reattachment regions are by no means uncommon. The analogy between Type III interference and separated flows is apparent from Fig. 8.6. Investigators who have studied these flows experimentally include:

- (i) Rom & Seginer [38] and Baker & Martin [39] who studied the reattachment behind a backward facing step (Fig. 8.6b).
- (ii) Bogdonoff & Vas [33], Holden [41, 43],

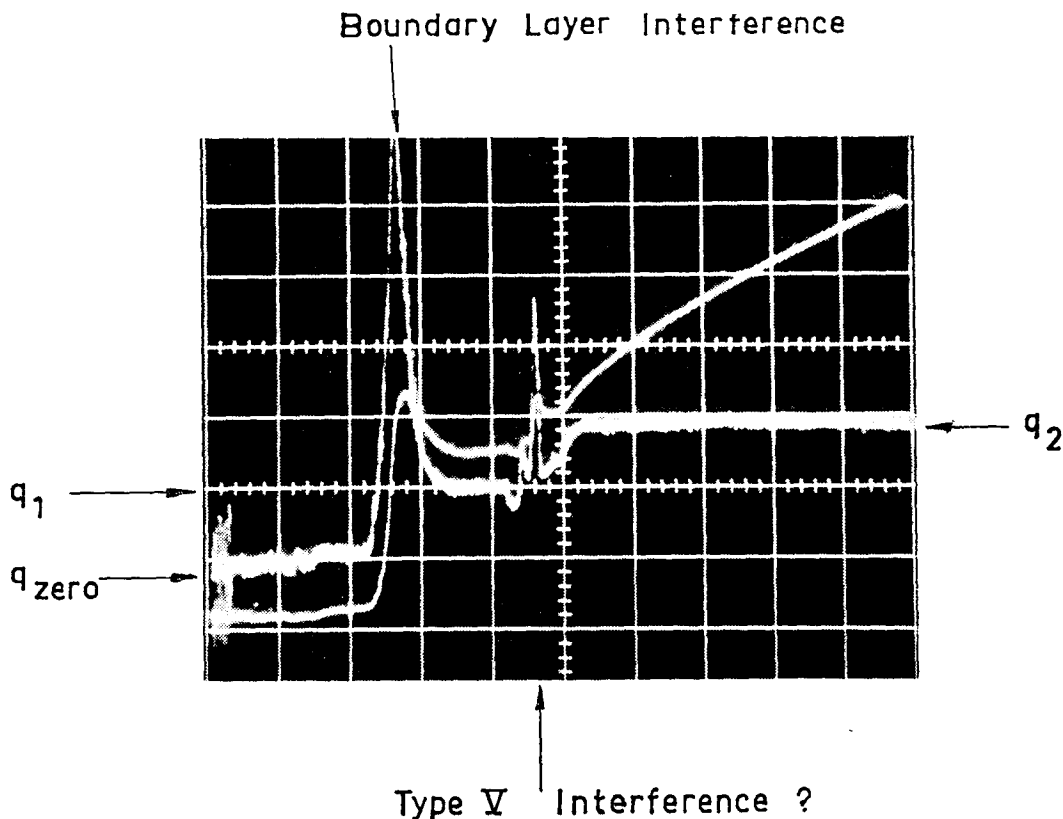


Fig. 8.5. Heat transfer (upper trace) and surface temperature (lower trace) for a blunted cone. $M_\infty = 4.6$. $\xi = 15^\circ$.
 $x/r = 1.032$ on upper side.

- Poisson-Quinton & Cérésuela [44], Kaufman, Meckler & Hartofilis [45] and Nestler [46] who studied reattachment on a forward facing wedge or flap (Fig. 8.6c).
 (iii) Bogdonoff & Vas [33], Wagner & Pine [47] and Holden [40, 42] who studied separation and reattachment on spiked bodies of revolution (Fig. 8.6d).
 (iv) Bogdonoff & Vas [33] who studied the reattachment on the downstream lip of a cavity (Fig. 8.6e).

8.2.2. Laminar and turbulent shear layers. In general the studies mentioned above were concerned with laminar shear layers. Nestler is the only worker who has made any progress with the turbulent reattachment problem. Poisson-Quinton and Cérésuela made an attempt to produce a turbulent shear layer, by using transition strips. This was only partially successful

and there is some doubt as to whether a fully turbulent shear layer was achieved. The experimental data available is too limited to draw any definite conclusions from, except that the heat transfer through a turbulent reattachment region is higher than through a laminar attachment region. This conclusion is also supported by the work of Kaufman and his co-workers who showed that the peak heat-transfer rate increased with Reynolds number.

Now Type III interference differs from the separated flows shown in Fig. 8.4 in so much that the Mach number M_2 adjacent to the free-shear layer is much lower than in the other cases for the same free-stream Mach number. In the present tests, for instance, M_2 was at most 2.35 (at $M_\infty = 7$ and $\xi = 10^\circ$). Even for free-stream Mach numbers up to 20, M_2 will not exceed 3.8 whatever value ξ we choose (see Fig. 7.5).

The question, therefore, is whether the

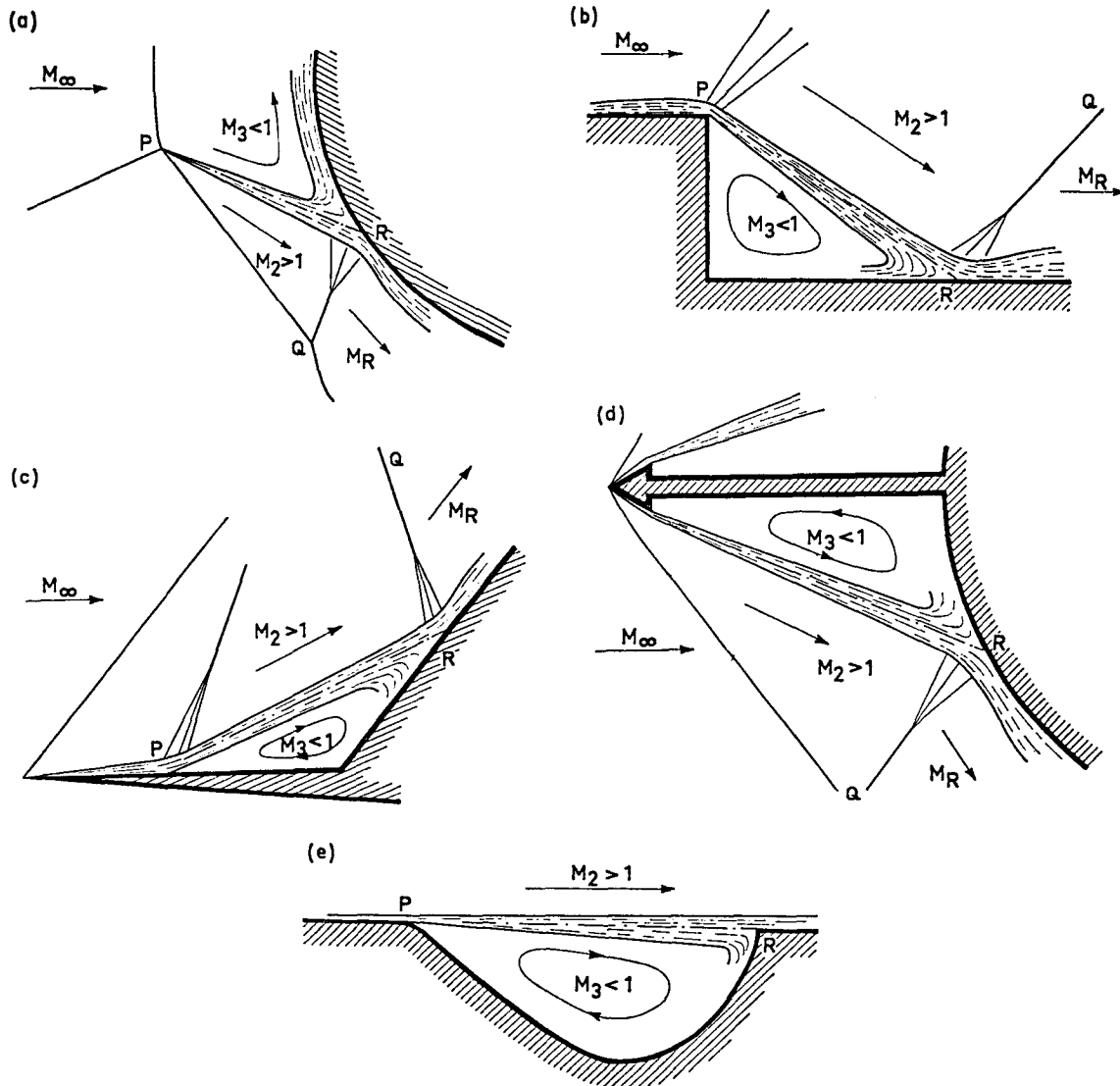


Fig. 8.6. Analogy between (a) Type III interference and (b-e) various types of separated flows.

shear layer will remain laminar at these relatively low Mach numbers. Consequently, how much of the separated flow studies we have mentioned are relevant to Type III interference? We have already seen an example of turbulent attachment in Fig. 6.10 for $M_\infty = 4.6$ and $\xi = 10^\circ$, whereas at $M_\infty = 7$ and $\xi = 10^\circ$ the shear layer appears to be laminar upto the attachment point (Fig. 7.7).

To answer this question we first look at work of Lin [48], Pai [49] and Miles [50] on the stability of a laminar shear layer. The criterion arrived at by Lin is that an inviscid vortex sheet will be stable with respect to

small disturbances provided

$$U_2 - U_3 > a_2 - a_3 \quad (8.1)$$

whereas Miles derives a somewhat different result, namely

$$U_2 - U_3 > (a_2^{\frac{1}{2}} + a_3^{\frac{1}{2}})^{\frac{1}{2}} \quad (8.2)$$

Pai arrives at a similar result to Miles but does not give it in this form. U_2 and U_3 are the velocities on either side of the vortex sheet and a_2 and a_3 the corresponding speeds of sound.

Fig. 8.7 shows how $(U_2 - U_3)$ varies with ξ for various free-stream Mach numbers, in

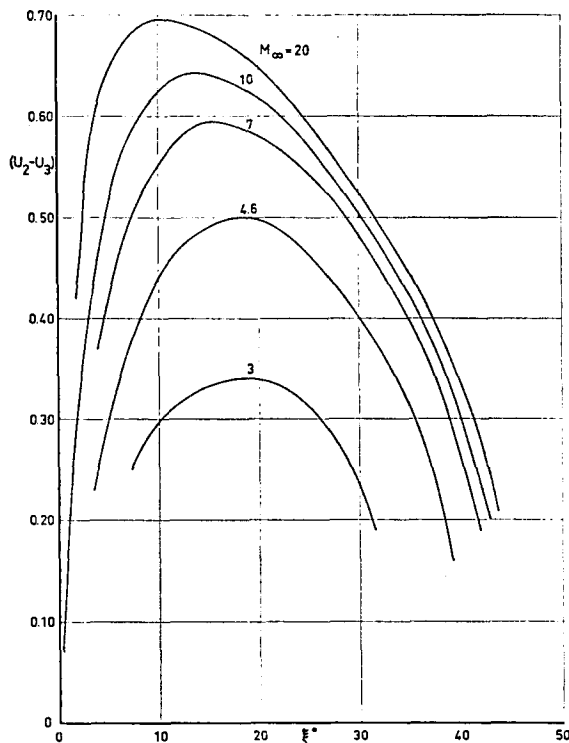


Fig. 8.7. $(U_2 - U_3)$ as a function of ξ^* for various free-stream Mach numbers. Type III interference.

the case of Type III interference. We do not need to calculate $(U_2 - U_3)$ directly to apply Lin's or Miles' criteria to Type III interference but we shall come back to this figure later.

Miles applies both his own and Lin's criteria to the stability of a vortex sheet originating at the intersection of two shocks. It is just this case which is of interest to us here. For such a flow

$$\frac{1}{2} U_2^2 + \frac{a_2^2}{(\gamma - 1)} = \frac{1}{2} U_3^2 + \frac{a_3^2}{(\gamma - 1)}. \quad (8.3)$$

Eqs. 8.1 and 8.2 can then be rewritten to give the stability boundaries in parametric form for the particular case of intersecting shocks.

According to Lin's criterion the boundary is defined by

$$M_3 = \frac{1}{2} [(3 - \gamma) - (\gamma + 1)m]/(\gamma - 1) \quad (8.4 \text{ a})$$

$$M_2 = \frac{1}{2} [-(3 - \gamma) + (\gamma + 1)m^{-1}]/(\gamma - 1) \quad (8.4 \text{ b})$$

where $m = a_2/a_3$

and according to Miles' criterion the stability boundary is defined by

$$M_3 = (\gamma - 1)^{-1}(1 + m^{\frac{1}{2}})^{-\frac{1}{2}}(1 - m^2) \\ - \frac{1}{2}(1 + m^{\frac{1}{2}})^{\frac{1}{2}} \quad (8.5 \text{ a})$$

$$M_2 = (\gamma - 1)^{-1}m^{-1}(1 + m^{\frac{1}{2}})^{-\frac{1}{2}}(1 - m^2) \\ + \frac{1}{2}m^{-1}(1 + m^{\frac{1}{2}})^{\frac{1}{2}} \quad (8.5 \text{ b})$$

Fig. 8.8 shows both these boundaries drawn for the case $\gamma = 1.4$. In the case of Type III interference it is fairly straightforward to calculate M_2 and M_3 on either side of the shear layer for any given M_∞ , ξ and γ (see Section 6.2). Fig. 8.8 shows the result of such a calculation covering a range of ξ from 0 to 40° . M_3 is plotted as a function of M_2 for various free-stream Mach numbers. These curves lie well above the stability boundaries defined by Eqs. 8.4 and 8.5. Judged by either criterion the shear layer would be expected to be unstable for all free-stream Mach numbers up to 20, which is contrary to what we observe experimentally, i.e. unstable for $M_\infty = 4.6$, stable for $M_\infty = 7$.

Increasing M_∞ and increasing ξ upto the point where M_2 is a maximum (see also Fig. 7.5) brings us nearer and nearer to a stable situation. Decreasing γ (i.e. increasing the stagnation temperature nearer to that

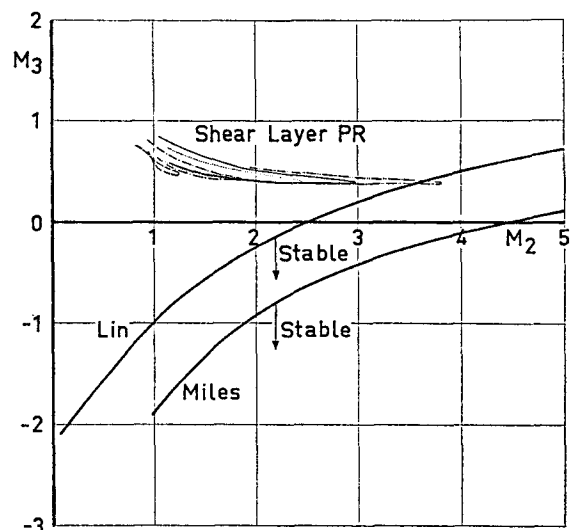


Fig. 8.8. M_3 versus M_2 for Type III interference, compared with stability criteria of Lin and Miles for $\gamma = 1.4$.
--- $M_\infty = 3$, - - - $M_\infty = 4.6$, $M_\infty = 7$, — $M_\infty = 10$, — . — $M_\infty = 20$.

encountered in actual flight) has an even greater tendency to stabilize the shear layer. This is clearly seen in Fig. 8.9, where we have examined the effect of varying γ at $M_\infty = 10$. Unfortunately, it has not been possible to test these predictions experimentally. However, the fact that a stable shear layer appears to be possible at a lower free-stream Mach number than that predicted by either Lin's or Miles' analysis, does not necessarily rule out the possibility that these trends (i.e. increasing stability with increasing M_∞ and ξ and decreasing γ) still hold.

It seems obvious, therefore, that viscosity, or more precisely Reynolds number, must be taken into consideration. In the case of separated flows, U_3 is virtually zero and the Reynolds number may be defined as

$$Re_2 = \frac{\rho_2 U_2 l}{\mu_2} \quad (8.6)$$

where l is the length of the free-shear layer. In the case of Type III interference, U_3 is quite large and the Reynolds number might be more appropriately defined as

$$Re_{2,3} = \frac{\rho_2 (U_2 - U_3) l}{\mu_2}. \quad (8.7)$$

Fig. 8.10 shows Re_2 and $Re_{2,3}$ per cm for $M_\infty = 4.6$ and 7 and $\xi = 6^\circ$ and 11° as a function of M_2 . These are calculated for $T_0 = 600^\circ\text{K}$ and $P_0 = 10$ atm. A typical length for the shear layer is between 5 and 10 mm at attachment. Also drawn in Fig. 8.9 is a line marking the transition Reynolds number for a free-shear layer as a function of M_2 . This is based on experimental data obtained by Chapman, Kuehn and Larson [51]. According to these earlier results the shear layer should be turbulent at $M_\infty = 4.6$ and laminar at $M_\infty = 7$. (Fortunately, our definition of Reynolds number is not critical here.) This, then, agrees very well with what we observe experimentally.

For a given free-stream Mach number R_2 and $R_{2,3}$ are a maximum when U_2 and $(U_2 - U_3)$ are a maximum. (Note that the variation of U_3 is small compared to the variation of U_2 .) Some idea of how the

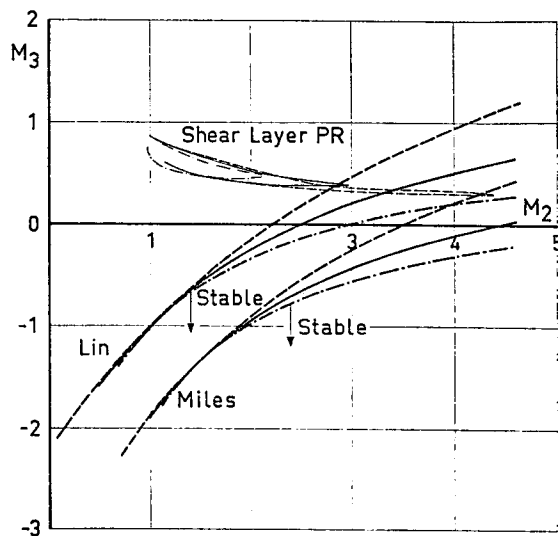


Fig. 8.9. M_3 versus M_2 for Type III interference at $M_\infty = 10$, compared with stability criteria of Lin and Miles. $\dots \gamma = 1.67$, $- \gamma = 1.4$, $-- \gamma = 1.2$.

Reynolds number depends on ξ can be gained from Fig. 8.7.

8.2.3. Theoretical attachment heat transfer.

(i) *Laminar shear layer.* The only analytical contributions to the problem of reattachment heat transfer to date are those of Chung and Viegas [52] and Holden [41]. Chung and Viegas derive a semi-empirical expression for the average heat transfer in a laminar reattachment region, based on normal reattachment at the lip of a cavity (Fig. 8.6e). The expression they derive for the average Nusselt number Nu_r is

$$Nu_r = \frac{q_r \sigma l}{(h_0 - h_w) \mu_2} = 0.0463 \sigma^{\frac{1}{3}} Re_l^{\frac{2}{3}} \times \left(\frac{P_r}{P_2} \right)^{\frac{1}{3}} \left(0.76 + 1.411 \frac{P_2}{P_r} \right) \quad (8.8)$$

for $2 \leq P_r/P_2 \leq 10$

where σ = Prandtl number

l = length of free-shear layer
and P_r/P_2 = pressure rise along the attachment streamline.

Holden [40, 42] purports to have used Chung and Viegas' result to calculate the heat-transfer rate on the shoulder of a spiked cone (Fig. 8.6d). We note, however, that Holden misquotes Chung and Viegas'

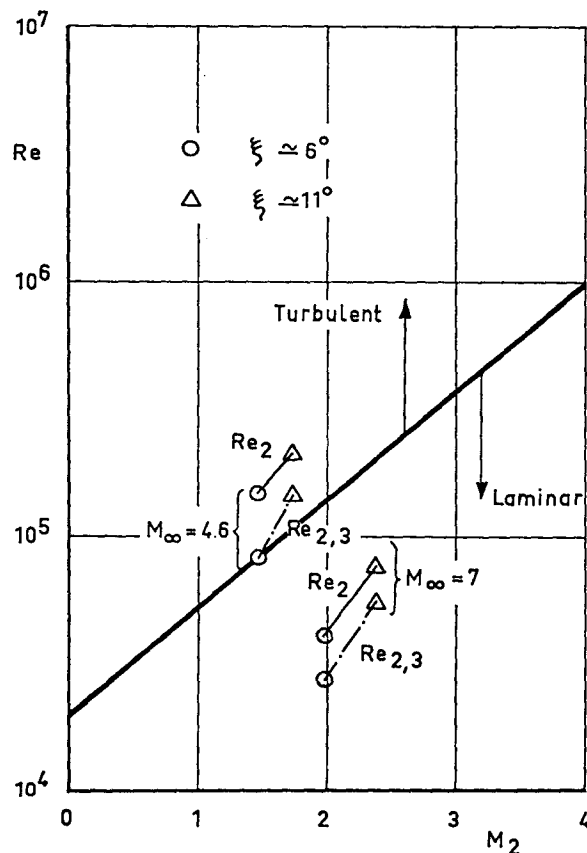


Fig. 8.10. Re_2 and $Re_{2,3}$ for Type III interference compared with transition Reynolds number as a function of M_2 .

result writing P_2/P_r instead of $(P_r/P_2)^{\frac{1}{2}}$. This mistake is repeated both in Refs. 40 and 42. Be this as it may, the average heat-transfer rates he obtains are then compared with the experimentally measured heat-transfer rates on a series of spiked cones (30° , 45° , 60° and 75° half angle) at $M = 10$ and 15. The agreement is poor, however. In some cases the theory overestimates the heat-transfer rate by as much as a factor of 3 and in other cases underestimates it by a factor of 2. Nor can any direct correlation between the size of the discrepancy and the cone angle be detected.

It is tempting to try to apply Eq. 8.6 to predict Type III interference heating, even though the reattachment angle is very shallow and the theory is really only intended for normal reattachment. (The only comparison with experiment Chung and Viegas have made was for an attachment angle of

45° but nevertheless showed good agreement.) Unfortunately, it overestimates the heating by a factor of 5 for the cases examined, neither does it predict the correct variation with P_r/P_2 for shallow attachment angles.

Holden [41] derives an approximate expression using an integral method for the maximum heat transfer immediately downstream of the reattachment compression for a laminar shear layer, based on the flow model shown in Fig. 8.6c. He shows that for reattachment angles greater than 35° the shear layer is so thinned out in the compression process that the boundary layer may be assumed to grow from the reattachment point. In this case the heat transfer, distance x downstream of the reattachment point, is adequately represented by

$$q_R = 0.332 \rho_R^* U_R (\sigma^*)^{-\frac{1}{2}} (h_{aw} - h_w) (Re_2)^{-\frac{1}{2}} \quad (8.9)$$

where the reference conditions are defined by

$$T^* = T_\infty + 0.58 (T_w - T_\infty) + 0.19 (T_{aw} - T_\infty) \quad (8.10)$$

Comparing Eqs. 8.7 and 2.2 we see that this is essentially the same assumption made by Hiers and Loubsky [13].

Of course, this method predicts an infinite heat-transfer rate at the attachment point. To overcome this difficulty an estimate of the boundary-layer thickness, δ_R , at the end of the reattachment process is needed. The maximum heat-transfer rate is then given by [41]

$$q_{\max} = \frac{0.332 \rho_R^* U_R (\sigma^*)^{-\frac{1}{2}} (h_{aw} - h_w)}{(\rho_R^* U_R x_R / \mu_R^*)^{\frac{1}{2}}} \quad (8.11)$$

$$\text{where } x_R = \left(\frac{U_R \rho_R T_w}{\mu_w T_R} \right) \left(\frac{\delta_R}{4.795} \right)^{\frac{1}{2}}. \quad (8.12)$$

A fairly simple method to calculate δ_R in terms of the boundary-layer thickness δ_1 at separation is described by Holden. He also compares the maximum heat-transfer rate predicted by Eq. 8.9 with the experimentally

measured values. Agreement with experiment is good upto reattachment angles of 30° but beyond this the theory becomes increasingly in error, underestimating the heat transfer by at least a factor of 2 at 45° reattachment angle. In fact the discrepancy may be even worse than we indicated since it is by no means certain that Holden actually measured the maximum heat-transfer rate. This is always difficult to establish when the gauges are mounted at finite intervals apart.

The drawback with Holden's analysis is that he attempts to apply integral methods to separation and reattachment regions where boundary-layer theory is no longer valid. Many workers share the uneasiness about such methods [53]. Nevertheless this is the only approach which has shown any results so far.

No attempt has been made to adapt Holden's analysis to Type III interference, although this should not be too difficult. In spite of our reservations about the use of integral methods there is still some hope that such an approach might give reasonable numbers for Type III interference heating, since the attachment angles are small. At $M_\infty = 4.6$ the attachment angle varies from 0° to 19° and $M_\infty = 7$ from 0° to 30° . Even at $M_\infty = 20$ the maximum attachment angle is only 38° .

Note that only the $M_\infty = 7$ experimental data in the present tests could be used for the purpose of comparison with the results of such an analysis.

(ii) *Turbulent shear layer.* The problem of turbulent reattachment heat transfer has been tackled semi-empirically by Nestler [46] for the case of reattachment on a deflected flap (Fig. 8.6c). Nestler postulates that

$$q_{\text{peak}} \sim (\rho_s U_2)^{0.8} \left(\frac{\mu_s}{\Delta x} \right)^{0.2} \sin \theta = \lambda_1 \quad (8.13)$$

where s denotes the stagnation conditions behind a normal shock having M_2 and P_2 approach condition Δx = width of the shear layer at reattachment θ = attachment angle

In the case of a deflected flap it is convenient to normalize q_{peak} relative the hinge line heat-transfer rate q_0 .

$$q_0 \sim \frac{(\rho_\infty U_\infty)^{0.8}}{F_c} \left(\frac{\mu_\infty}{x_0} \right)^{0.2} = \lambda_2 \quad (8.14)$$

where F_c = compressibility correction factor
= C_f/C_{f_0} and

x_0 = distance of hinge line from leading edge.

For M_2 in the range 2.6 to 6.5, a correlation of available experimental data leads to the following empirical relation:

$$\frac{q_{\text{peak}}}{q_0} = 0.245 \left(\frac{\lambda_1}{\lambda_2} \right) + 2.35 \quad (8.15)$$

It is possible that a similar expression could be obtained for q_{peak}/q_{20} in the case of Type III interference. It is easy to calculate everything in Eq. 8.13 with the exception of Δx . This can either be measured from schlieren photographs or calculated from another empirical relation obtained by Chow and Korst [65], viz.

$$\Delta x = \frac{2.14}{(12 + 2.76 M_2)} l \quad (8.16)$$

where l is the length of the shear layer. We cannot predict l exactly, as we have already pointed out, but fortunately λ_1 is a weak function of Δx , so we can accept a fairly large error in l without effecting too large an error in λ_1 . For engineering purposes this is probably acceptable.

No attempt has been made to correlate the limited data available from the $M = 4.6$ tests, in this fashion as yet.

8.2.4. Dependence of attachment heat-transfer rate on the attachment pressure rise. It is evident that the attachment heat-transfer rate and the attachment pressure rise exhibit a similar variation with x/r (cf. Figs. 4.10 and 4.11 with Figs. 5.9–5.13). This suggests a correlation between q_{peak}/q_{20} and p_{peak}/p_{20} . A plot of $\log (q_{\text{peak}}/q_{20})$ against $\log (p_{\text{peak}}/p_{20})$ shows that for the part of the curve which is attributable to Type III interference the following empirical relation holds

$$\left(\frac{q_{\text{peak}}}{q_{20}}\right) \simeq A \left(\frac{p_{\text{peak}}}{p_{20}}\right)^{1.35} \quad (8.17)$$

where $A = 2.2$ at $M = 4.6$
and $A = 1.1$ at $M = 7$.

The higher heat-transfer rate at $M = 4.6$, roughly double that at $M = 7$ for the same p_{peak}/p_{20} , may be due to the fact that the shear layer is turbulent at $M = 4.6$ whereas it is laminar at $M = 7$. The two curves converge for higher values of p_{peak}/p_{20} due to Type IV interference. We shall say more about Type IV interference in the next section.

If Eq. 8.17 holds for all Mach numbers, then we see at once, from what we have already said concerning the variation of p_{peak}/p_{20} with M_∞ and ξ in Section 7.2, that q_{peak}/q_{20} at a particular point on the model increases with both M_∞ and ξ , for small ξ up to $10\text{--}18^\circ$ depending on M_∞ .

This conclusion is consistent with experimental data of Holden [41] for the case of a laminar reattaching shear layer, which shows that the peak heat-transfer rate increases with increasing attachment angle, and of Nestler [46], for the case of a turbulent reattaching shear layer, which shows that the peak heat-transfer rate increases with both increasing attachment angle and increasing Mach number.

8.3. Heating attributable to a supersonic impinging jet

The peak heating associated with Type IV interference occurs at the point where a supersonic jet impinges on the surface of the model (Fig. 7.10). Just as in the case of Type III interference the peak heating increases with the peak pressure generated by the impact of the jet. This is evident from comparing the variation of q_{peak}/q_{20} with x/r (Figs. 4.10 and 4.11) with the variation of p_{peak}/p_{20} with x/r (Figs. 5.9–5.12) for the hemisphere. Note that in the case of blunt axisymmetric bodies Type IV interference is that which gives the highest peak heat-transfer rates.

Now the peak heating is dependent not only on the peak pressure generated by the

jet but also on the width of the jet, the angle with which the jet impinges on the surface of the model and whether the jet is laminar or turbulent at this point. In fact these are all interrelated. We have already seen how a thin jet curls up more than a broad jet resulting in a shallower impingement angle. In addition the pressure decay along the axis of the jet increases as $\Delta x/l$, the width to length ratio, decreases, as does the turbulence level.

Assuming that $\Delta x/l$ is large (i.e. greater than $1/5$ roughly speaking), such that the core of the jet is still laminar and the impingement angle is large, then the flow in the impingement region of the jet will still be like we have shown it in Fig. 7.10. The point O is then a stagnation point and the heat transfer is given by [19]

$$q_{\text{peak}} = \frac{k_w(T_0 - T_w)}{\sqrt{\nu_w}} \left(\frac{Nu}{\sqrt{Re_w}} \right) \sqrt{C} \quad (8.18)$$

$$= 0.47 \frac{k_w(T_0 - T_w)}{\sqrt{\nu_w}} \sqrt{C} \quad (8.19)$$

for a two-dimensional stagnation point where $T_w/T_0 = 0.5$ and $\sigma = 0.7$.

A suitable estimate for C , the stagnation-point velocity gradient, in the case of impact normal to the surface can be made by appealing to the analogy between the subsonic flow in the impingement region of the jet (Fig. 7.10) and that ahead of a blunt body, diameter Δx , in a supersonic flow. This gives

$$C = F \cdot \frac{2}{\Delta x} \sqrt{\frac{p_{\text{peak}}}{\rho_{\text{peak}}}} \quad (8.20)$$

where F is a factor which depends on the bluntness of the body. Within the accuracy of this approximation we can assume $F = 1$. Hence

$$q_{\text{peak}} = 0.47 \frac{k_w(T_0 - T_w)}{\sqrt{\mu_w}} \left(\frac{2}{\Delta x} \sqrt{p_{\text{peak}} \cdot \rho_{\text{peak}}} \right)^{\frac{1}{2}} \quad (8.21)$$

Now the stagnation point heat-transfer rate q_{20} for a hemisphere is given by

$$\begin{aligned} q_{20} &= \frac{k_w(T_0 - T_w)}{\sqrt{\nu_w}} \left(\frac{Nu}{\sqrt{Re_w}} \right) \sqrt{C} \\ &= 0.64 \frac{k_w(T_0 - T_w)}{\sqrt{\mu_w}} \cdot \left(\frac{1}{r} \cdot \sqrt{p_{20} \cdot \rho_{20}} \right)^{\frac{1}{2}} \end{aligned} \quad (8.22)$$

for the case $T_0/T_w = 0.5$ and $\sigma = 0.7$.

Combining Eqs. (8.21) and (8.22) and remembering that T_0 and T_w are the same in both cases we get

$$\frac{q_{\text{peak}}}{q_{20}} = 1.03 \left(\frac{r}{\Delta x} \cdot \frac{p_{\text{peak}}}{p_{20}} \right)^{\frac{1}{2}}. \quad (8.23)$$

From schlieren photographs taken at $M = 4.6$, $(r/\Delta x)$ is estimated to be somewhere between 15 and 20 when the maximum peak pressure is generated. The variation of q_{peak}/q_{20} with ξ according to Eq. 8.23 can then be expressed in the following table:

M_∞	ξ	$r/\Delta x$ est.	p_{peak}/p_{20} max.	q_{peak}/q_{20} max.
4.6	5°	17.5	2.7	7.05
4.6	10°	17.5	4.05	8.65
4.6	15°	17.5	4.4	9.05

The agreement between these calculated values and the measured values of q_{peak}/q_{20} shown in Fig. 4.10 is remarkable. The success of this simple approach in predicting the maximum peak heat transfer with such accuracy may well be fortuitous. Ideally we should like to measure the velocity gradient in the stagnation region of the jet directly. This necessitates measuring the pressure distribution on the model in the vicinity of the stagnation point with a high degree of accuracy. In the present tests this is precluded by the narrowness of the subsonic region ($\sim 1-2$ mm). However, this should not be too difficult for larger models, say 10 cm diameter, or larger, should further tests be forthcoming. If Eq. 8.23 holds and $r/\Delta x$ is not a strong function of M_∞ or ξ , then we can at once predict the effect of varying both M_∞ and ξ on the maximum heat-transfer rate, since

$$\frac{q_{\text{peak}}}{q_{20}} \simeq \text{const} \left(\frac{p_{60}}{p_{20}} \right)^{\frac{1}{2}}. \quad (8.24)$$

From Fig. 7.8 it is clear that q_{peak}/q_{20} will increase with increasing M_∞ and for increasing ξ upto 10–18° depending on M_∞ .

If the jet impinges on the surface at some angle θ , the peak heat-transfer rate can be approximated by

$$\frac{q_{\text{peak}}}{q_{20}} \simeq \text{const} \left(\frac{p_{60}}{p_{20}} \right)^{\frac{1}{2}} \cdot \sin \theta \quad (8.25)$$

providing $\Delta x/r$ is still reasonably large, so that the pressure decay along the axis of the jet near the impingement point is small. Unfortunately, we cannot predict θ analytically and the condition $\Delta x/l$ large (i.e. $> 1/5$) only holds over a small range of positions of the impinging shock relative to the body.

From Figs. 6.11 and 6.12 we see how the jet soon becomes fully turbulent. Transition occurs first in the shear layer *PRV*, either before or at the shock *QR*. The remarks concerning transition in Section 8.2.2 apply here since Type IV interference is identical to Type III interference upto the shock *QR*.

The shear layer *QTU* is usually laminar upto the point *T* because of the lower velocity difference $(U_5 - U_4)$, which means that $R_{5,4} \sim \frac{1}{2} R_{2,3}$. Fig. 8.11 shows the variation of $(U_5 - U_4)$ with ξ for free-stream Mach numbers up to 20.

The rôle of turbulence on the stagnation point heat transfer is not yet well understood. Direct measurements of the effects of turbulence on the heat-transfer characteristics of two-dimensional impinging jets have been carried out by Gardon and Akfirat [56]. The turbulence level in the jet was varied by altering the distance of the nozzle from the plate on which the measurements were made as well as by means of turbulence promoters. The maximum heat transfer coincided with the maximum turbulence ($u'/u \sim 65\%$) in the jet, for $l/\Delta x \sim 8$ and was at this point about $1\frac{1}{2}$ times the heat-transfer rate for $l/\Delta x = 2$ where $u'/u \sim 5\%$. Any further increase in $l/\Delta x$ beyond 8 was accompanied by a rapid fall-off in the heat-transfer rate being about $\frac{1}{3}$ of that for $l/\Delta x = 2$ at $l/\Delta x = 80$. What is lacking in their work is an indication of what the laminar heat-

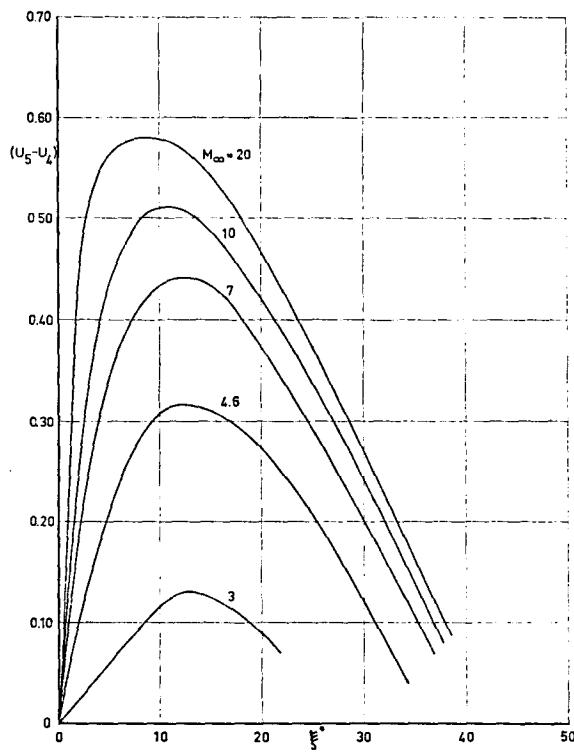


Fig. 8.11. Variation of $(U_5 - U_4)$ with ξ for various free-stream Mach numbers. Type IV interference.

transfer rate should have been since we know from the work of Kestin and others [22, 23] that a turbulence level of only 2% can have a very large effect (an increase by $\sim 60-80\%$) on the stagnation point heat transfer.

One effect of the high turbulence level will be that transition in the boundary layer in the plate will occur very near the stagnation point. In this case the heat-transfer rate in the stagnation region can be expressed, according to van Driest [57], in the form

$$q(x) = \frac{f}{(Re_x)^{\frac{1}{4}}} \rho \cdot C \cdot x(h_r - h_w) \quad (8.26)$$

$$\text{where } f = C_H \cdot (Re_x)^{\frac{1}{4}} = 0.040 \sigma^{-\frac{1}{4}} \quad (8.27)$$

for a cylinder

$$\text{and } f = 0.042 \sigma^{-\frac{1}{4}} \quad (8.28)$$

for a sphere,

where x is the distance from the stagnation point, C_H the Stanton number and C is the velocity gradient as before.

Eq. 8.26 has been successfully applied by Jepps and Robinson [55] to determine the convective heating on a rocket launch pad.

Note that the laminar heat-transfer rate (Eq. 8.19) exceeds the turbulent heat-transfer rate for very small x . However, the turbulent heat-transfer rate soon exceeds the laminar heat-transfer rate for larger x . Supposing then that transition occurs some distance from the stagnation point, the heat transfer will fall at first, as x increases, then rise again sharply at the point where transition takes place. This can have the effect of producing secondary peaks in the heat-transfer distribution. We note that Gardon and Aksirat measured secondary peaks on either side of the primary peak at the stagnation point but offered no explanation for this phenomenon.

In the present case secondary peaks are also observed (see Fig. 4.7a) but these are probably due to shock/boundary layer interactions at the points *B* and *E* (Fig. 7.10).

For very thin jets, the flow picture we have sketched in Fig. 7.10 no longer holds. The jet is now fully turbulent and the pitot pressure on the centre line of the jet has decayed markedly. According to measurements made by Anderson and Johns [54] the pitot pressure will have decayed to approximately $1/10$ of its original value by the time $l/\Delta x = 20$. The jet is, therefore, no longer supersonic and has diffused completely. There is no noticeable pressure rise at the point where the jet meets the model surface although it does lead to an increase in the heat-transfer rate outboard of this point. This is probably due to transition in the boundary layer on the model due to the high external turbulence level.

An example of the temperature-sensitive paint technique to study the heating due to a thin, diffused jet on a fin is shown in Fig. 8.12. Note the region of low heating inboard of the impingement point which is thought to be due to a bubble of 'dead' air. This reasoning is supported by surface flow tests which we shall discuss in Section 9.1. This then would explain a broad dip followed by a slight hump in records obtained with thin

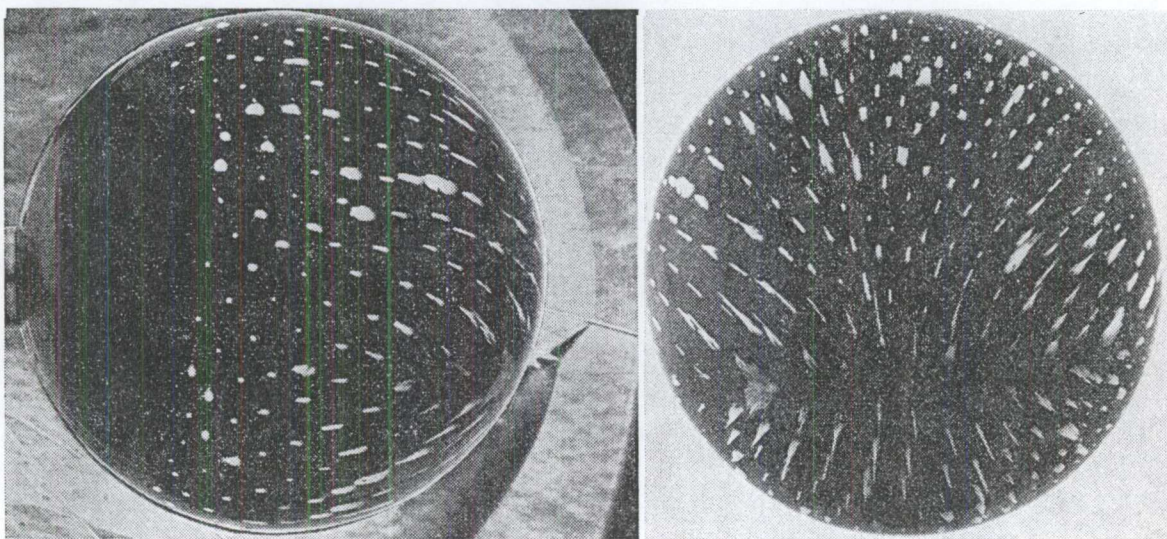


Fig. 9.1. Oil-spot pattern on 50 mm sphere. Side view superimposed on schlieren photograph (left). Front view (right). $M = 4.6$. $\xi = 5^\circ$. Type IV interference.

films on the upperside of the hemisphere.* The dip coincides with the bubble and the hump with the attachment of the diffused jet. We have already seen an even more extreme example of a thin diffused jet in Fig. 8.4, in connection with Type V interference.

9. SUPPLEMENTARY TESTS

Supplementary tests were carried out to ascertain the importance of 3-dimensional flow about the models, since the analysis of shock impingement presented here is strictly 2-dimensional. An oil-spot flow visualization technique was used to determine surface flow patterns and temperature-sensitive paint to localize regions of high heat transfer. The feasibility of making further pressure and heat-transfer measurements in the FFA hypersonic gun tunnel was also investigated.

9.1. Oil-spot flow visualization tests

We have already seen an example of the oil-spot technique in Fig. 4.6. In this case it was employed to check that the flow over

* It may also explain the low heat-transfer rates measured by Carter and Carr [3] for $M < 3$ (see Table I, Chapter 3).

the shock generator was sensibly two-dimensional.

The paint used for these tests was white, consisting of a mixture of zinc oxide and linseed oil. The models were blued to improve contrast, the paint being applied with a fine brush or pen so as to form a grid of small white spots.

The models were mounted on the injector but raised and lowered manually, their position relative to shock being more easily adjusted in this way. This setting-up took 1–2 sec. Consequently, the paint should be very viscous so as not to be disturbed appreciably during this period. About 30 sec exposure to the flow was sufficient to produce a satisfactory pattern.

Fig. 9.1 shows the surface flow pattern on a 50 mm sphere, resulting from Type IV interference. To make comparison easier the side view of the model is superimposed on the schlieren photograph taken during the run. The front view of the model shows how the stagnation point (or rather stagnation line) no longer coincides with the axis of the model but is shifted downwards to the jet-attachment line. Note also the very well defined upward and downward deflection of the flow on either side of the attachment line. Summing up from these tests we can say that for Types III and IV interfer-

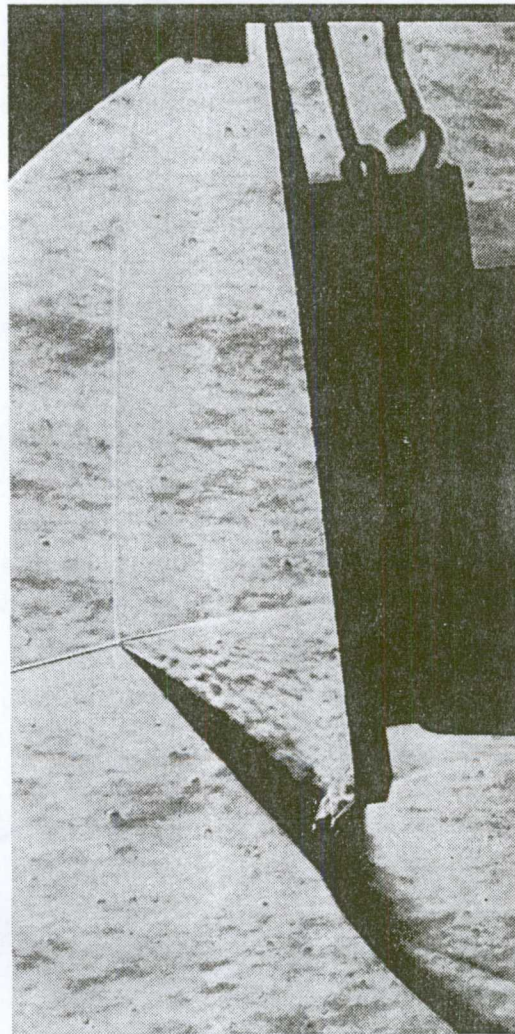
*a**b*

Fig. 9.2. *a.* Oil-spot pattern on a 30 mm wide flat plate. *b.* Corresponding schlieren photograph. $M = 4.6$. $\xi = 5^\circ$. Type III interference.

ence on a sphere, the flow is virtually 2-dimensional near the attachment line of the shear layer or jet, except for very shallow attachment angles (i.e. for impingement low down or high up on the body).

For blunter bodies, say a flat-faced cylinder, the 2-dimensional character of the flow is even more pronounced. This is illustrated for the extreme case of Type III interference on a flat plate nearly normal to the free stream (Fig. 9.2). It is arranged such that the shear layer meets the plate along the bottom edge. Immediately above the attachment line there is a region of dead air, due to the shallow attachment angle.

But what is really remarkable is the way the flow climbs up the face of the plate and over the top edge and not so much round the sides as one might expect for a plate of this aspect ratio. Again this confirms that we are on fairly safe ground tackling the problem 2-dimensionally.

When we come to look at cylindrical fins, however, the picture is a little more complicated. Fig. 9.3 shows the surface flow pattern on a cylinder resulting from Type IV interference. In this particular example the jet is much thinner than the one we saw in Fig. 9.1. As a result the jet curls upwards more and the attachment angle is much

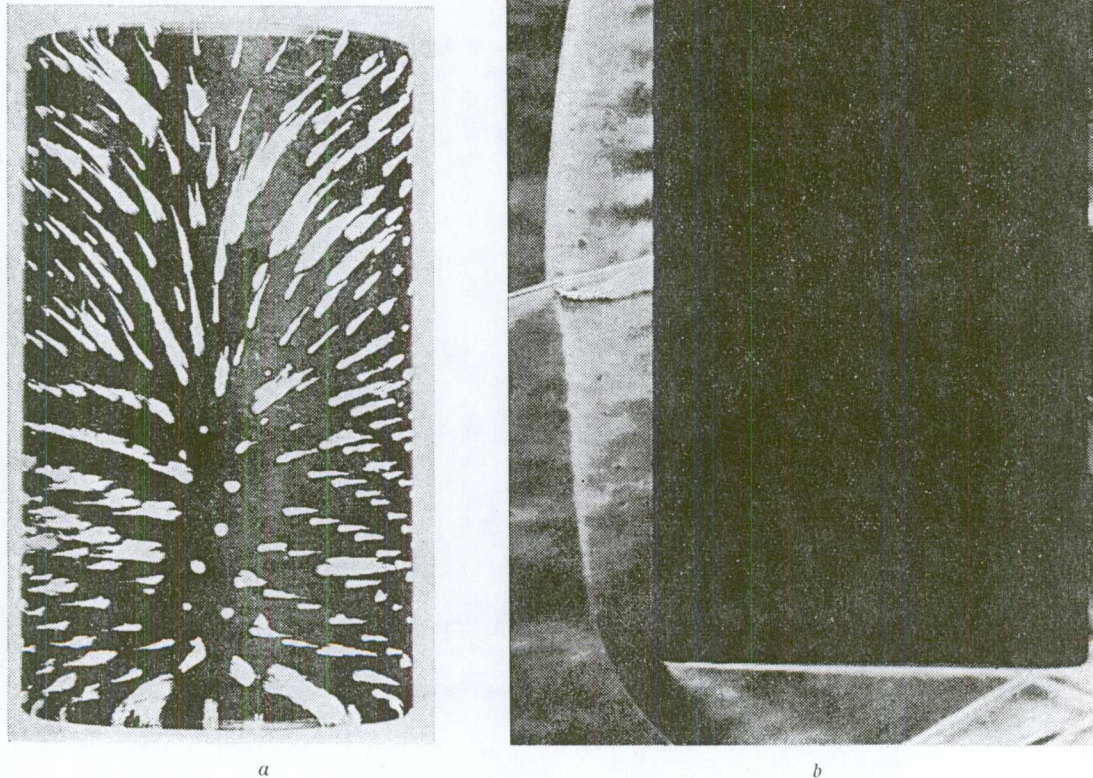


Fig. 9.3. *a.* Oil-spot pattern on a 30 mm diameter cylinder. *b.* Corresponding schlieren photograph. $M = 4.6$, $\xi = 5^\circ$. Type IV interference.

shallower. Note how this again gives rise to a dead-air region immediately below the attachment point. Above the attachment point the flow runs roughly parallel to the leading edge, whereas below the attachment point the flow is virtually perpendicular to the leading edge. In this case, a 2-dimensional analysis would scarcely be justified except over a very thin strip along the leading edge of the model.

This visualization technique may be further refined to the point where one can predict the heat-transfer rate at various points on the model, with surprising accuracy, although this was not tried here. A more sophisticated account of this method and its possibilities is given by Meyer [58].

9.2. Heat-transfer visualization tests

These tests rely on the property of certain temperature-sensitive paints which change colour at some known temperature. Several colour changes can be incorporated into one paint, if desired. Such paints are available commercially under the name Detectotemp, supplied by Hardman & Co., Belleville, N.J.

The models for these tests were moulded from a hard silicone rubber (Emerson & Cumming's Eccosil 4850) which has low thermal conductivity and which will withstand temperatures upto 200°C . The technique finally arrived at to give an aerodynamically smooth surface was first to paint the model with silicon lacquer. While the model was still 'tacky' it was powdered

with the paint (which comes in powdered form) and carefully smoothed out with a finger. A very smooth and even cover was achieved in this fashion.

Earlier attempts to paint or spray the model using the solvents and binder supplied by the manufacturer gave much less satisfactory results. Included in these preliminary tests were a few runs made using the same glass models that had been used for the thin-film measurements although the paint was rough and flaked easily from the glass. However, these served to confirm the location of the peak heating.

Fusible temperature indicators of the type described by Jones and Hunt [59], which change from an opaque solid to a translucent liquid at a known temperature were also tried as an alternative to temperature-sensitive paints. However, these were finally rejected because of an uneven and rough surface finish.

Examples of the use of temperature-sensitive paints to study the heating due to Type I interference on a paraboloid model (Fig. 8.3) and Types IV and V interference on a swept fin (Figs. 8.4 and 8.10) have already been presented. In particular the reader should compare Fig. 8.10 with the oil-flow pattern shown in Fig. 9.3. Together they give us a much better insight into the effects of Type IV interference on a fin, one technique filling in gaps not covered by the other.

Ideally a sequence of photographs of the model should be taken over a period of, say, 30 sec to establish the temperature-time history of the model. In this way absolute values for the heat-transfer distribution on the model can be deduced (see Cérésuela, Bétrémieux and Cadars [60] and Cérésuela & Bétrémieux [61]). Unfortunately, this was difficult with the present experimental set-up since the model had to be removed from the tunnel to be photographed. For this reason each model was photographed only once, after 5–10 sec exposure to the flow. Note that the paints do not return to their original colours when the models cool down, otherwise this procedure would not have been possible.

9.3. Tests in a hypersonic gun tunnel

Some ten runs were made in the FFA Hypersonic Gun Tunnel at $M = 9.8$, using equipment left over from earlier experiments, to ascertain the feasibility of conducting a shock impingement study in this facility. This would have been very attractive, not only because of the higher Mach numbers possible ($M_\infty = 9.8$ and 12) but because much higher temperatures, up to 2200°K in air, could be attained. This, together with the possibility of using gases other than air, would have allowed us to check the theoretical predictions concerning the variation of γ .

Unfortunately, these preliminary tests showed that a larger test section would be necessary to accommodate models of sufficient size to make accurate measurements possible. In the old test section the flow was uniform over a core approximately 10 cm in diameter. Fig. 9.4 shows a typical schlieren photograph taken during one of these runs in the gun tunnel. This photograph, taken using a provisional schlieren system, is of poorer quality than those obtained in Hyp 200 but nevertheless enables us to identify the Type III interference pattern quite easily. The shock is produced by a flat plate ($\sim 5 \times 5$ cm) mounted on a thin support below the model. The model is a 15 mm hemisphere, the largest which could be used without blocking the tunnel. The sting houses a pressure transducer for measurements on the hemisphere. Only one pressure measurement could be obtained per run with the large Kistler 701 transducer available for these tests. However, this could have been considerably improved by using specially designed models and up to 6 transducers (the smaller Kistler 630 A) if it had been decided to go ahead with the study.

10. CONCLUSIONS

The problem of shock impingement has been 'solved' in the sense that we are able to predict all six different shock interference patterns observed experimentally. Moreover, we are able to establish under what condi-

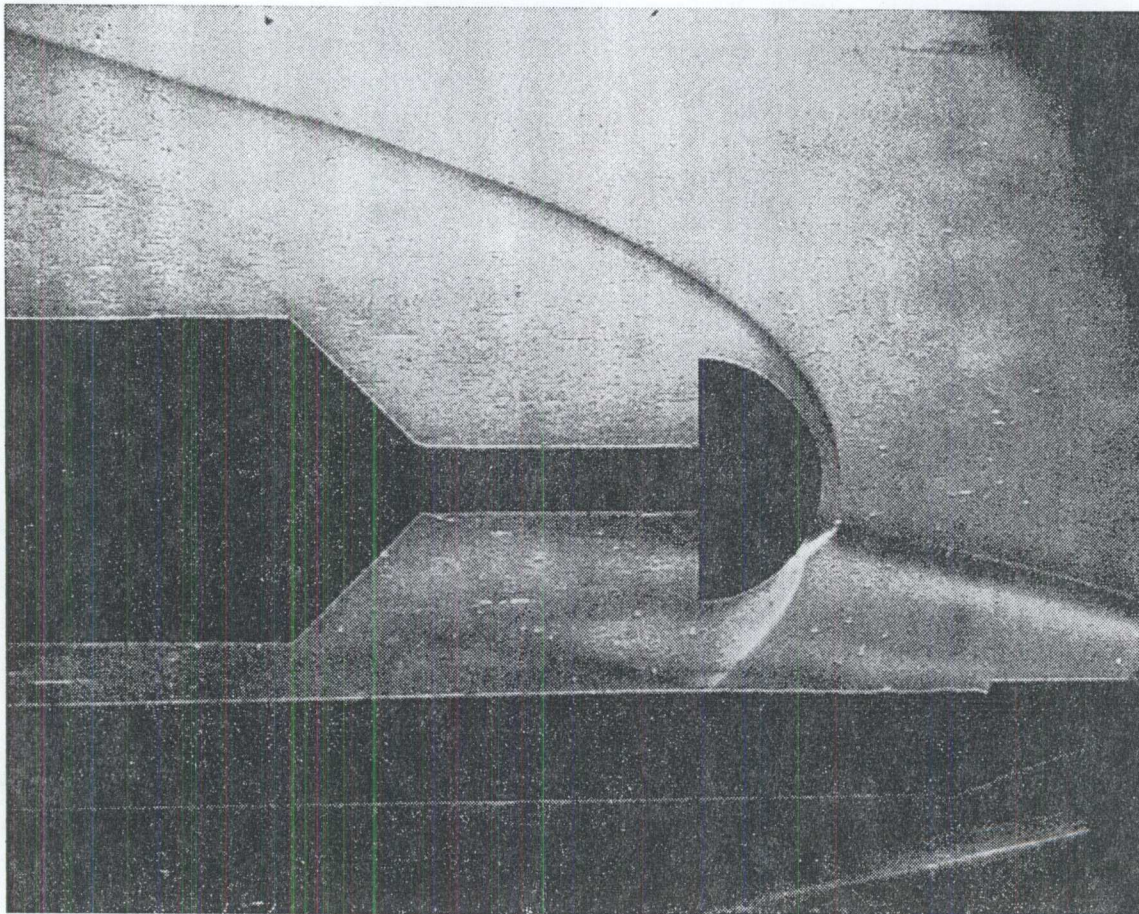


Fig. 9.4. Type III interference on a 15 mm hemisphere in a gun tunnel. $M_\infty = 9.8$.

tions each is set up—depending on the geometry of the model, the free-stream Mach number and the strength and position of the impinging shock relative to the model.

This enables us to identify four distinct mechanisms, not including transition, which are responsible for the peak pressures and peak heat-transfer rates measured near the impingement point on the model. Given a particular configuration the problem of shock impingement can be transformed into one of the better known (yet still very difficult and not too well understood) 'standard' problems of fluid mechanics. These include shock/boundary-layer interactions (Types I, II and V interference), stability and attachment of a free-shear layer (Type III interference), impingement of a supersonic jet (Type IV interference) and the phenomena of vorticity amplification (Types IV

and V interference). When we add to this list the asymmetric blunt body problem—which must be solved in the case of Type III interference to obtain the shock stand-off distance above the impingement point and hence the length of the free-shear layer and which appears again for Type IV interference, when we must solve two simultaneous problems with a common boundary in order to determine the dimensions of the jet—the immense complexity of the shock impingement problem can at once be appreciated. This has meant that we have not always been able to produce numbers for pressures or heat-transfer rates but have contented ourselves with establishing the physics of the problem and giving a qualitative description of the effects of varying the free-stream Mach number and strength of the impinging shock, for example.

Nevertheless, in the case of Type III interference we can calculate the peak pressure in good agreement with experiment for any given free-stream Mach number and strength of the impinging shock. We have shown that the peak pressure will increase with increasing Mach number and increasing strength of the impinging shock, reaching a maximum for ξ between 10° and 18° depending on Mach number. A similar dependence on M_∞ and ξ is shown to exist for Type IV interference, although in this case we can only calculate the peak pressure for the case of normal impact of the jet, again in excellent agreement with experiment. The effect of varying γ has also been examined. As γ decreases the peak pressure can also be expected to increase for a given free-stream Mach number. It has not been possible to check this experimentally in any of FFA's existing facilities but this obviously needs to be done.

The discrepancy between the predicted attachment pressure rise and the experimentally measured pressure rise depends on whether the shear layer or jet is laminar or turbulent. In order to throw more light on this, the problem of transition in a free-shear layer has been examined. It is shown that the transition Reynolds number for given free-stream conditions may easily be calculated, again in good agreement with available experimental data.

The attachment heat-transfer rate for Type III interference has not been calculated explicitly, although methods of tackling this problem for both laminar and turbulent attaching shear layers have been discussed. The measured variation with M_∞ , ξ and the geometry of the model is similar to that for the peak pressure and a simple correlation is given. We observe that the attachment heat-transfer rate is higher for a turbulent shear layer than for a laminar one for the same attachment pressure rise. The data on which these correlations are based is scanty, however, and more is needed. A further study of Type III interference on a wedge, say, is justified because of its similarity to a number of other separated flow

problems. Since the origin of the shear layer and the flow conditions on either side of it are well defined and easily calculated, uncertainties in connection with the separation process are eliminated and hence we have far better control over the conditions at attachment.

In the case of Type IV interference an expression for the maximum heat peak transfer rate which occurs for normal impact of the jet has been derived by appealing to the analogous flow ahead of a blunt body which has the same diameter as the jet. The agreement with experiment is surprisingly good. The peak heating can be expected to increase with the square root of the peak pressure, and hence increases with increasing Mach number and increasing strength of the impinging shock reaching a maximum when $\xi = 10\text{--}18^\circ$ depending on the Mach number.

Type IV interference is of special interest for the case of blunt fins at small angles of sweep. The width and impact angle of the jet on the fin leading edge will depend on the overall fin/body configuration—in particular the leading edge diameter and the distance of the impingement point outboard of the fin/body junction—as well as the free-stream conditions. In general the jet will be relatively long and thin (compared to the case of normal impact) and impact the fin obliquely (Fig. 6.18a). In this case we cannot predict the impact pressure or the heat transfer rate without taking into consideration the pressure decay along the jet axis and the high level of turbulence in the jet. Evidently much more work, both theoretical and experimental, is needed in this area. The transition from Type IV, to Type V and finally to Type VI interference on a cylindrical fin, as the sweep angle is increased, is evident from Fig. 6.18. Whether Type IV interference gives greater peak heating than Type V (shock/boundary-layer interaction) depends on how much the jet has diffused at the point of impact.

The experiments described in this report are mainly concerned with axisymmetric blunt bodies, since they show all the inter-

esting features of shock impingement. For practical engineering applications the study of shock impingement on blunt fins is possibly of more importance. Certainly the quasi-static techniques developed here for measuring the heat transfer and pressure could be used for a blunt fin, too. However, in view of the many experiments that have been carried out on wedge/fin configurations earlier, it would be desirable to re-examine these results first, in the light of the present study. There is evidently a great body of data which has not been presented in these various reports (schlieren photographs of each run etc), which could be of value and yet which did not at first appear relevant to the problem.

Finally we note that the novel experimental techniques described in this report could find a more general application in continuous tunnels where conventional calorimetry, for example, is unsatisfactory for one reason or another.

ACKNOWLEDGEMENTS

The author wishes to thank Mr. P. Westerström for help in conducting the tunnel tests and for many useful contributions to the experimental programme. He would also like to express his appreciation of many valuable discussions with Prof. H. Thomann and Dr. I. Ryhming, as well as other colleagues whose scepticism when shown the initial results provoked a more detailed study! The kind cooperation of Dr. P. F. Bikle of NASA Flight Research Center is also acknowledged.

SYMBOLS

- a = speed of sound
- α = skin thickness (Eq. 2.1.)
- A = constant (Eq. 8.17)
- c = specific heat
- C = velocity gradient
- c_p = specific heat at constant pressure
- C_f = skin friction coefficient
- C_{f_i} = incompressible skin friction coefficient

- C_H = Stanton number
- C_p = pressure coefficient
- d = diameter of leading edge
- D defined by Eq. 2.5
- E defined by Eq. 2.6
- h = specific enthalpy
- k = thermal conductivity
- K defined by Eq. 2.4
- l = length of shear layer or jet
- l_{\max} = distance along jet where centre line pitot pressure starts to decay
- m = ratio of speeds of sound on either side of shear layer
- M = Mach number
- Nu = Nusselt number
- P = pressure
- P_j = pitot pressure on centre line of jet
- q = heat transfer rate
- r = radius of axi-symmetric body
- Re = Reynolds number
- t = time
- T = temperature
- U = flow velocity
- V = injection velocity
- x = distance from centre line or attachment point along surface of model
- Δx = width of jet or shear layer at attachment
- y = distance above shock
- ξ = flow deflection produced by shock generator
- η = flow deflection downstream of shock impingement point
- σ = Prandtl number
- δ = shock stand-off distance
- γ = ratio of specific heats
- λ_1 defined by Eq. 8.13.
- λ_2 defined by Eq. 8.14.
- ν = kinematic viscosity = μ/ρ
- μ = viscosity
- ρ = density
- Λ = sweep angle

Suffixes

- ∞ in free stream
- 1, 2, 3 etc. regions in shock interference patterns defined in text
- 10 stagnation point conditions in shock layer on plate

20	stagnation point conditions in free stream	<i>w</i>	at wall
0	at edge of boundary layer	<i>aw</i>	adiabatic wall

R downstream of reattachment point

APPENDIX

CONSTRUCTION AND CALIBRATION OF THIN-FILM GAUGES AND ANALOGUE NETWORKS

1. CONSTRUCTION OF THIN-FILM GAUGES

The glass models were ground from 30 mm diameter rods of Duran 50—a borosilicate glass, similar to Pyrex, which is supplied by Jenaer Glaswerk, Scott & Gen Mainz. Four holes were bored in each model to take out leads. The surface was then polished and the edges of the holes rounded and flamed to give an aerodynamically smooth finish and a good backing for the gauges. Fig. A.1 shows a hemispherical model prior to application of the gauges.

Six thin films, approximately 0.4 mm wide, were applied to each model using

Hanovia Bright Platinum 05* and a drawing pen. The paint was subsequently reduced to a bright metallic film by heating the model to 800°C in a well ventilated oven. The oven was switched off immediately 800°C had been reached and the model allowed to cool slowly to around 100°C when it could be removed from the oven. The cooling took about 4 hours. This technique yielded clean, well defined gauges approximately 0.1μ thick, one coat of platinum being sufficient to achieve a satisfactory film.

The leads connecting the thin film gauges to the holes bored in the model consisted of a 3 mm wide platinum underlay, over which was painted a layer of Hanovia Silver Paste 38. The platinum underlay and the thin films were fired at the same time and the silver painted over afterwards. To bond the silver paste to the platinum the model was heated to 600°C. Finally, copper wires, taken out through the holes in the model, were soldered directly to the platinum underlay, the holes plugged with epoxi and the leads rubbed down with a fine-grade steel wool to preserve a smooth surface.

Before being glued into their brass holders the models were annealed for 12 hours at 150°C, to release stresses in the glass. An earlier model had exhibited a slight increase in cold resistance between calibrations, although the temperature coefficient of resistance appeared unchanged. A similar tendency had also been noted by Winding *et al.* [62], who attributed this to stress relief



Fig. A.1. Hemispherical glass model prior to application of gauges and leads.

in the glass and suggested the above annealing process, which worked very well.

Fig. A.2 illustrates the construction of a hemispherical model. A typical glass model was shown earlier in Fig. 4.1.

2. CONSTRUCTION OF THE ANALOGUE NETWORKS

T-section analogue networks, similar to the type devised by Meyer [18], were used, one with a rise time of $50 \mu\text{ sec}$ and providing a total test time of 50 msec and the other with a rise time of $100 \mu\text{ sec}$ and providing a total test time of 100 msec . Fig. A.3 shows the circuit diagram for the $50 \mu\text{ sec}$ rise time analogue network connected to the Wheatstone bridge containing the thin-film gauge. The electrical components used in the network were $\pm 5\%$ quality with the exception of the first ten sections, where $\pm 1\%$ components were used.

3. CALIBRATION OF THE THIN-FILM GAUGES AND THE ANALOGUE NETWORKS

The surface temperature of the gauge, T_w , is given in terms of the bridge output voltage, V_T , by the expression

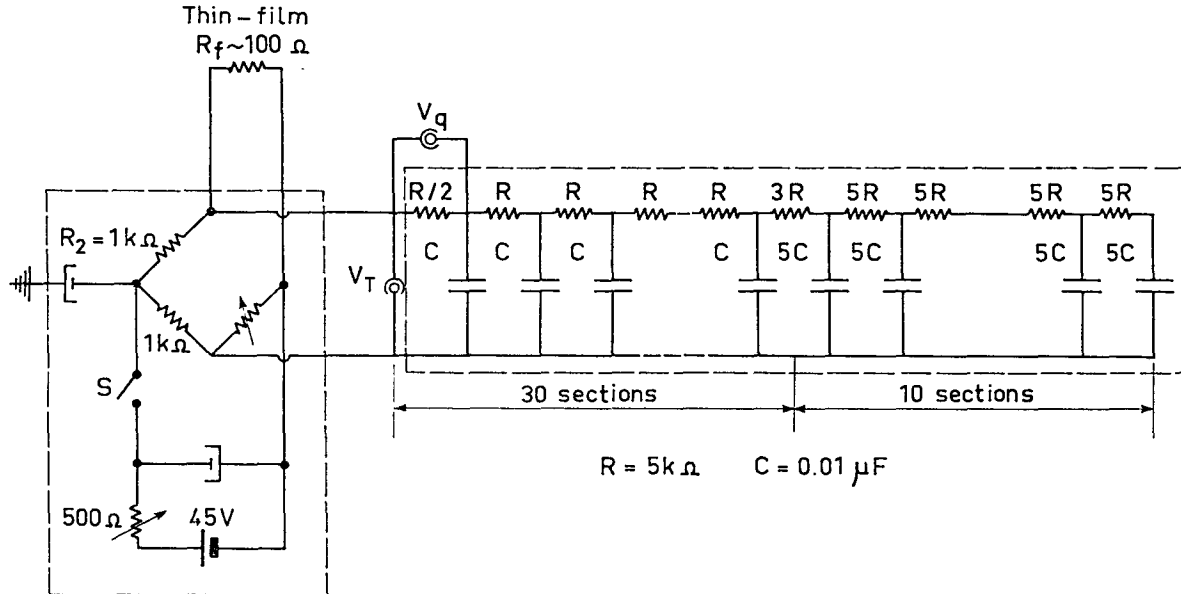


Fig. A.2. Construction of typical glass model.

$$T_w(t) = \frac{(R_2 + R_f)^2}{ER_2 R_f} V_T \quad (\text{A.1})$$

and the heat-transfer rate, q , is given in terms of the analogue-network output voltage, V_q , by the expression:

$$q(t) = \frac{2 G(\rho ck)^{\frac{1}{2}}}{\alpha(RC)^{\frac{1}{2}}} \frac{(R_2 + R_f)^2}{ER_2 R_f} \cdot V_q \quad (\text{A.2})$$

where α is the temperature coefficient of resistance of the thin film,
 ρ, c, k are the density, specific heat and

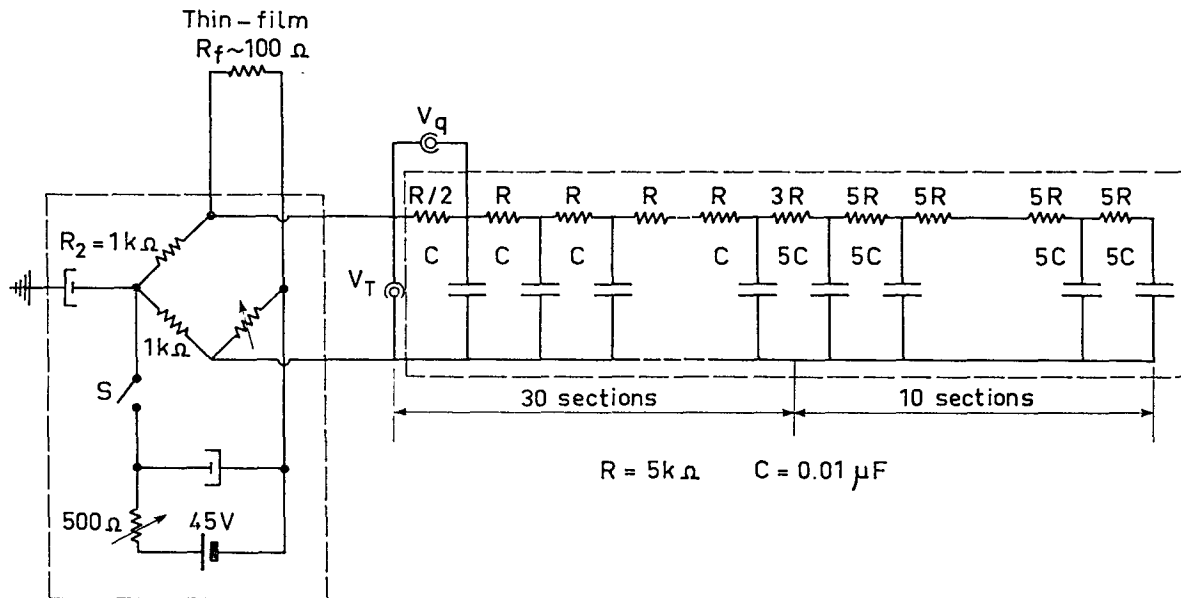


Fig. A.3. Thin-film gauge connected to bridge and analogue network.

thermal conductivity, respectively, of the backing material, and G is a gauge factor, which accounts for the temperature-dependent thermal properties of the backing material—here assumed equal to unity since the surface temperature changes are small.

It is the quantities α and $(\rho ck)^{\frac{1}{2}}$ that must be determined by calibration. The resistance of the thin film, R , the voltage across the bridge, E , and the components R_2 , R and C , defined in Fig. A.3, are assumed known.

3.1. Determination of α

The temperature coefficient of resistance, α , was measured by heating the model in a silicon oil bath over the range 15°C to 150°C, the calibration curves being linear over this range. The variation of α from gauge to gauge was approximately $\pm 5\%$, providing the same manufacturing process and the same batch of platinum paint was used. A typical value was $\alpha = 1.05 \times 10^{-3} \text{ }^{\circ}\text{C}^{-1}$. This agrees well with a value of $0.92 \times 10^{-3} \text{ }^{\circ}\text{C}^{-1}$ obtained by Vidal [63].

3.2. Determination of $(\rho ck)^{\frac{1}{2}}$

The values given by the manufacturers for Duran 50 at 20°C were

$$\rho = 2.23 \text{ gm cm}^{-3}$$

$$c = 0.199 \text{ cal gm}^{-1} \text{ }^{\circ}\text{C}^{-1}$$

$$k = 2.79 \times 10^{-3} \text{ cal cm}^{-1} \text{ sec}^{-1} \text{ }^{\circ}\text{C}^{-1}$$

This gives $(\rho ck)^{\frac{1}{2}} = 3.52 \times 10^{-2} \text{ cal cm}^{-2} \text{ }^{\circ}\text{C}^{-1} \text{ sec}^{-\frac{1}{2}}$ (cf. $(\rho ck)^{\frac{1}{2}} = 3.57 \times 10^{-2} \pm 5\%$ for Pyrex obtained by Skinner [64]).

As a check the technique devised by Skinner was used to measure $(\rho ck)^{\frac{1}{2}}$ for Duran 50. In this method a capacitor is discharged through the thin film, first with the model in air and then immersed in a reference liquid—for which $(\rho ck)^{\frac{1}{2}}$ is accurately known. If the output of the Wheatstone bridge be $A(t)$ with the gauge in air and $A^*(t)$ with the gauge immersed in the reference liquid, then

$$(\rho ck)_{\text{glass}}^{\frac{1}{2}} = (\rho ck)_{\text{liquid}}^{\frac{1}{2}} \left(\frac{A}{A^*} - 1 \right)^{-1}. \quad (\text{A.3})$$

Since the gauges used in the present investigation were uncoated, Dow Corning 200 Silicone Fluid was substituted for water, which Skinner used as reference liquid. Assuming $(\rho ck)^{\frac{1}{2}}$ for the silicone fluid to be 0.0102, values of $(\rho ck)^{\frac{1}{2}}$ for Duran 50 within 5 % of the manufacturer's figures were obtained. Although this method is an improvement on the earlier electrical calibration method described by Vidal [63], which was accurate only to $\pm 15\%$, it appears to have no advantage—other than convenience—over more accurate, direct measurements of ρ , c and k , as carried out by the manufacturer. Consequently, the manufacturer's figures were used throughout.

It was also assumed that the variation of $(\rho ck)^{\frac{1}{2}}$ with temperature was the same for Duran 50 as for Pyrex. Consequently, Skinner's value for Pyrex, viz.

$$\frac{1}{(\rho ck)^{\frac{1}{2}}} \cdot \frac{d(\rho ck)^{\frac{1}{2}}}{dT} = 0.002 \pm 20\% \quad (\text{A.4})$$

was used for making small corrections. This was in reasonable agreement with data supplied by the manufacturer, who was unable to quote more accurate figures.

3.3. Check on the performance of the analogue network

Although many workers check out the working of their analogue networks by discharging a condenser through a thin film, connected into the bridge/analogue circuit, this method has a number of disadvantages. Among these we must reckon the fact that Joule heating along a narrow strip violates the assumption of one-dimensional heat flow, that such heating may be uneven due to irregularities in the film and that the area of the film is often difficult to measure accurately.

The method devised here uses the normal bridge/analogue circuit. The bridge is placed out of balance and a mercury switch, S , closed generating a step voltage, V_T , at the input of the analogue. We note that V_T

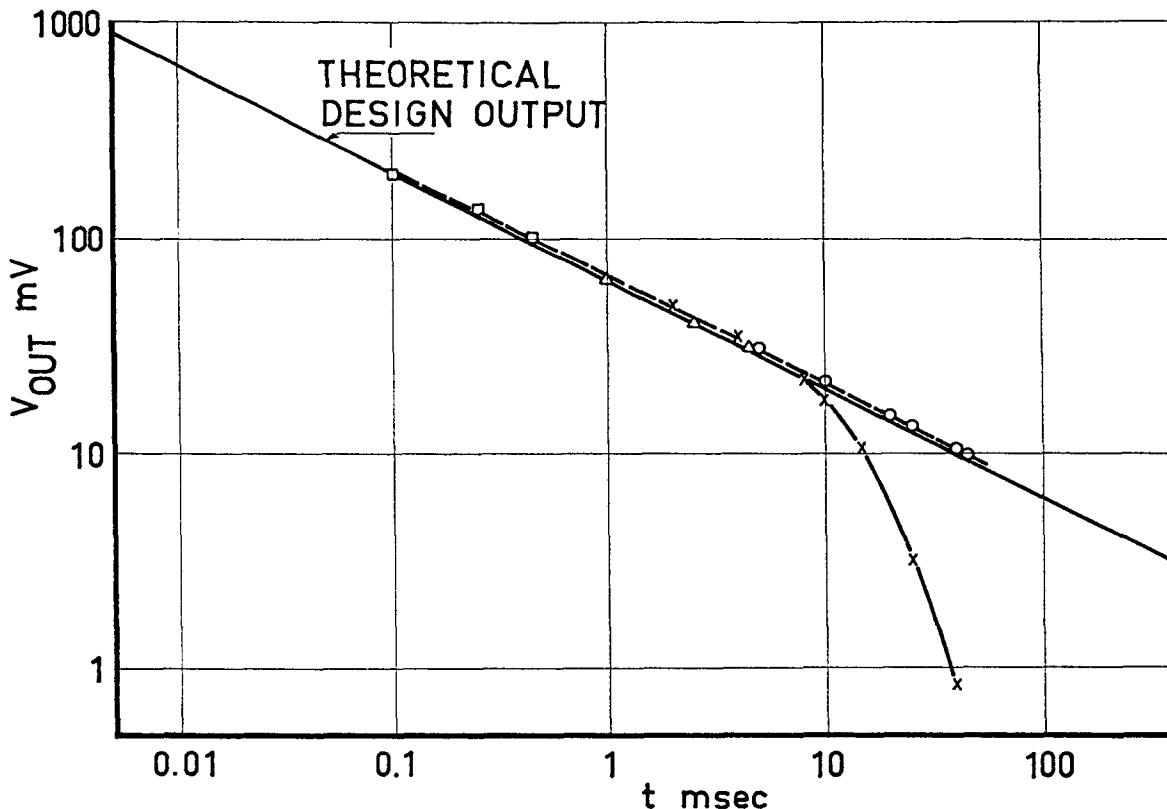


Fig. A.4. Comparison between measured and theoretical output from analogue network. \square , \triangle and \circ $t_R \approx 50$ msec $\times t_R \approx 1.7$ msec. Sudden drop in output marks end of available test time.

constant (i.e. T_w constant) corresponds to $q(t)$ proportional to $t^{-\frac{1}{2}}$. This would be the heating due to, say, a laminar boundary layer generated aft of a shock wave moving over some point on a body. The measured output voltage, $V_q(t)$, can then be compared with the design output

$$V_q(t)_{\text{design}} = \left(\frac{RC}{4\pi t} \right)^{\frac{1}{2}} V_T. \quad (\text{A.5})$$

Fig. A.4 shows such a comparison. It demonstrates how a loose connection after 13 sections was detected as a reduction in the test time ($t_R \sim 1.7$ msec compared with a design test time of 50 msec).

REFERENCES

1. EDNEY, B. E.: Temperature measurements in a hypersonic gun tunnel using heat-transfer methods. *J. Fluid Mech.*, Vol. 27, P. 3 (February 1967), pp. 503-512 and 4 plates.
2. NEWLANDER, R. A.: Effect of shock impingement on the distribution of heat-transfer coefficients on a right circular cylinder at Mach numbers of 2.65, 3.51, and 4.44. *NASA TN D-642* (1961).
3. CARTER, H. S., CARR, R. E.: Free-flight investigation of heat transfer to an unswept cylinder subjected to an incident shock and flow interference from an upstream body at Mach numbers up to 5.50. *NASA TN D-988* (1961).
4. FRANCIS, W. L.: Experimental study of the effect of shock impingement on fin heat transfer in hypersonic flow. *Ford Aeronutronic Publ. U-1802* (1962).
5. BECKWITH, I. E.: Experimental investigation of heat transfer and pressures on a swept cylinder in the vicinity of its intersection with a wedge and flat plate at Mach number 4.15 and high Reynolds numbers. *NASA TN D-2020* (1964).
6. JONES, R. A.: Heat-transfer and pressure investigation of a fin-plate interference model at a Mach number of 6. *NASA TN D-2028* (1964).
7. SILER, L. G., DESKINS, H. E.: Effect of shock impingement on heat-transfer and

- pressure distributions on a cylindrical-leading-edge model at Mach number 19. *Arnold Eng. Dev. Center, AEDC-TDR-64-228* (1964).
8. FONTENOT, J. E., Jr.: A method of estimating the effect of shock interaction on stagnation line heating. *AIAA J.*, Vol. 3, No. 3 (March 1965), pp. 562-564.
 9. RAY, A. D., PALKO, R. L.: An investigation of the effects of shock impingement on a blunt leading edge. *Arnold Eng. Dev. Center, AEDC-TR-65-153* (1965).
 10. FRANCIS, W. L.: Experimental heat-transfer study of shock impingement on fins in hypersonic flow. *J. Spacecr. Rockets*, Vol. 2, No. 4 (July-August 1965), pp. 630-632.
 11. KNOX, E. C.: Measurements of shock-impingement effects on the heat transfer and pressure distributions on a hemicylinder model at Mach number 19. *Arnold Eng. Dev. Center, AEDC-TR-65-245* (1965).
 12. BUSHNELL, D. M.: Interference heating on a swept cylinder in region of intersection with a wedge at Mach number 8. *NASA TN D-3094* (1965).
 13. HIERS, R. S., LOUBSKY, W. J.: Effects of shock-wave impingement on the heat transfer on a cylindrical leading edge. *NASA TN D-3859* (1967).
 14. DEVEIKIS, W. D., SAWYER, J. W.: Aerodynamic characteristics of tension shell shapes at Mach 3.0. *NASA TN D-3633* (1966).
 15. SAWYER, J. W., DEVEIKIS, W. D.: Effects of configuration modifications on aerodynamic characteristics of tension shell shapes at Mach 3.0. *NASA TN D-4080* (1967).
 16. BIKLE, P. F., WATTS, J. D., KNIGHT, W. J.: NASA Edwards Flight Research Center. *Private communications*. (January 1968.)
 17. HOSHIZAKI, H.: Mass transfer and shock generated vorticity. *ARS J.*, Vol. 30, No. 7 (July 1960), pp. 628-634.
 18. MEYER, R. F.: Further comments on analogue networks to obtain heat flux from surface temperature measurements. *Nat. Aero. Establ., Canada, LR 375* (1963).
 19. RESHOTKO, E., COHEN, C. B.: Heat transfer at the forward stagnation point of blunt bodies. *NACA TN 3513* (1955).
 20. WERLE, M. J.: Simplified expressions for laminar heating rates on isothermal bodies. *J. Spacecr. Rockets*, Vol. 3, No. 6 (June 1966), pp. 946-947.
 21. SHORT, W. W., BROWN, R. A. S., SAGE, B. H.: Thermal transfer in turbulent gas streams. Effect of turbulence on local transport from spheres. *J. Appl. Mech.*, Vol. 27, No. 3 (September 1960), pp. 393-402.
 22. KESTIN, J., MAEDER, P. F., SOGIN, H. H.: The influence of turbulence on the transfer of heat to cylinders near the stagnation point. *ZAMP*, Vol. 12, Nr. 2 (März 1961), pp. 115-132.
 23. SUTERA, S. P., MAEDER, P. F., KESTIN, J.: On the sensitivity of heat transfer in the stagnation-point boundary layer to free-stream vorticity. *J. Fluid Mech.*, Vol. 16, P. 4 (August 1963), pp. 497-520.
 24. LIEPMANN, H. W., ROSHKO, A.: *Elements of gasdynamics* (NY & London 1960), pp. 85-88.
 25. LIEPMANN, H. W., ROSHKO, A., DHAWAN, S.: On reflection of shock waves from boundary layers. *NACA Rep. 1100* (1952).
 26. YOUNG, A. D.: Boundary layers. *Modern developments in fluid dynamics. High speed flow*. Vol. 1 (Oxford 1953), pp. 375-475.
 27. SEDDON, J.: The flow produced by interaction of a turbulent boundary layer with a normal shock wave of strength sufficient to cause separation. *Aero. Res. Counc., R & M 3502* (1960).
 28. FAGE, A., SARGENT, R. F.: Shock wave and boundary layer phenomena near a flat plate surface. *Proc. Roy. Soc. Lond. (A)*, Vol. 190, No. 1020 (1947), pp. 1-20.
 29. FINLEY, P. J.: Experiments on the reattachment of a turbulent axisymmetric shear layer. *Aero. Quart.*, Vol. 18, P. 4 (November 1967), pp. 379-398.
 30. HENDERSON, L. F.: Experiments on the impingement of a supersonic jet on a flat plate. *ZAMP*, Vol. 17, Nr. 5 (September 1966), pp. 553-569.
 31. SCHLICHTING, H.: *Boundary layer theory* (NY et al. 1960), pp. 364-374.
 32. HAMITT, A. G.: The interaction of shock waves and turbulent boundary layers. *J. Aero. Sci.*, Vol. 25, No. 6 (June 1958), pp. 345-356.
 33. BOGDONOFF, S. M., VAS, I. E.: Some experiments on hypersonic separated flows. *ARS J.*, Vol. 32, No. 10 (October 1962), pp. 1564-1572.
 34. HOLDEN, M. S.: An analytical study of separated flows induced by shock wave-boundary layer interaction. *NASA CR-600* (1966).
 35. HOLDEN, M. S.: Theoretical and experimental studies of separated flows induced by shock wave-boundary layer interaction. *AGARD separated flows meeting, Brussels, May 1966*.
 36. KELLEY, L. R.: Wind tunnel tests at supersonic Mach numbers to determine heat-transfer coefficients in the shock wave-boundary layer interaction region on a

- plane surface. *Univ. So. Calif., Engng. Center, USCEC Rep.* 65-41 (1962).
37. MARTELLUCCI, A., LIPFERT, F. W.: Shock wave-laminar boundary-layer interaction. Integral analysis and experimental results. *AGARD separated flows meeting, Brussels, May 1966.*
 38. ROM, J., SEGINER, A.: Laminar heat transfer to a two-dimensional backward facing step from the high-enthalpy supersonic flow in the shock tube. *AIAA J.*, Vol. 2, No. 2 (February 1964), pp. 251-255.
 39. BAKER, P. J., MARTIN, B. W.: Heat transfer in a supersonic separated flow over a two-dimensional backward-facing step. *Int. J. Heat Mass Transfer*, Vol. 9, No. 10 (October 1966), pp. 1081-1088.
 40. HOLDEN, M. S.: Separated flow studies at hypersonic speeds. P. I. Separated flows over axisymmetric spiked bodies. *Cornell Aero. Lab., CAL Rep. AF-1285-A-13 (1)* (1964).
 41. HOLDEN, M. S.: Separated flow studies at hypersonic speeds. P. II. Two-dimensional wedge separated flow studies. *Cornell Aero. Lab., CAL Rep. AF-1285-A-13 (2)* (1964).
 42. HOLDEN, M. S.: Experimental studies of separated flows at hypersonic speeds. P. I: Separated flows over axisymmetric spiked bodies. *AIAA J.*, Vol. 4, No. 4 (April 1966), pp. 591-599.
 43. HOLDEN, M. S.: Experimental studies of separated flows at hypersonic speeds. P. II: Two-dimensional wedge separated flow studies. *AIAA J.*, Vol. 4, No. 5 (May 1966), pp. 790-799.
 44. POISSON-QUINTON, Ph., CÉRÉSUELA, R.: Efficacité et échauffement de gouvernes en hypersonique. *5th ICAS & Royal Aero. Soc. Centenary Conf., London, September 1966.*
 45. KAUFMAN, L. G. II, MECKLER, L., HARTOFILIS, S. A.: An investigation of flow separation and aerodynamic controls at hypersonic speeds. *J. Aircraft*, Vol. 3, No. 6 (November-December 1966), pp. 555-561.
 46. NESTLER, D. E.: Correlation of turbulent heat flux to deceleration flaps in supersonic flow. *AIAA Paper No. 68-13* (1968).
 47. WAGNER, R. D. JR., PINE, W. C., HENDERSON, A., JR.: Laminar heat-transfer and pressure-distribution studies on a series of reentry nose shapes at a Mach number of 19.4 in helium. *NASA TN D-891* (1961).
 48. LIN, C. C.: On the stability of the laminar mixing region between two parallel streams in a gas. *NACA TN 2887* (1953).
 49. PAI, S.-I.: On the stability of a vortex sheet in an inviscid compressible fluid. *J. Aero. Sci.*, Vol. 21, No. 5 (May 1954), pp. 325-328.
 50. MILES, J. W.: On the disturbed motion of a plane vortex sheet. *J. Fluid Mech.*, Vol. 4, P. 5 (September 1958), pp. 538-552.
 51. CHAPMAN, D. R., KUEHN, D. M., LARSON, H. K.: Preliminary report on a study of separated flows in supersonic and subsonic streams. *NACA RM A55L14* (1956).
 52. CHUNG, P. M., VIEGAS, J. R.: Heat transfer at the reattachment zone of separated laminar boundary layers. *NASA TN D-1072* (1961).
 53. YOUNG, D. A. *et al.*: Separated flows. A round table discussion, Rhode-Saint-Genèse. *AGARD Rep. 548* (1966).
 54. ANDERSON, A. R., JOHNS, F. R.: Characteristics of free supersonic jets exhausting into quiescent air. *Jet Prop.*, Vol. 25, No. 1 (January 1955), pp. 13-15, 25.
 55. JEPPE, G., ROBINSON, M. L.: Convective heating at the deflecting surface of a rocket launch-pad. *J. Roy. Aero. Soc.*, Vol. 71, No. 679 (July 1967), pp. 469-475.
 56. GARDON, R., AKFIRAT, J. C.: The role of turbulence in determining the heat-transfer characteristics of impinging jets. *Int. J. Heat Mass Transfer*, Vol. 8, No. 10 (October 1965), pp. 1261-1272.
 57. VAN DRIEST, E. R.: The problem of aerodynamic heating. *Aero. Eng. Rev.*, Vol. 15, No. 10 (October 1956), pp. 26-41.
 58. MEYER, R. F.: A note on a technique of surface flow visualisation. *Nat. Aero. Establ., Canada, Rep. LR-457* (1966).
 59. JONES, R. A., HUNT, J. L.: Use of fusible temperature indicators for obtaining quantitative aerodynamic heat-transfer data. *NASA TR R-230* (1966).
 60. CÉRÉSUELA, R., BÉTRÉMIEUX, A., CADARS, J.: Mesure de l'échauffement cinétique dans les souffleries hypersoniques au moyen de peintures thermosensibles. *Rech. Aéro.*, No. 109 (Novembre-Décembre 1965), pp. 13-19. Also publ. as ONERA T. P. n° 313.
 61. CÉRÉSUELA, R., BÉTRÉMIEUX, A.: Mesures de flux thermiques en hypersonique. *Colloque d'aérodynamique appliquée à l'A.F.I.T.A.E., Tolouse, 8-9 novembre 1965.* Also publ. as ONERA T. P. n° 293.
 62. WINDING, C. C., TOPPER, L., BAUS, B. V.: Metal-film resistance thermometers for measuring surface temperatures. *Industr. Engng. Chem.*, Vol. 47, No. 3 (March 1955), pp. 386-392.
 63. VIDAL, R. J.: Model instrumentation techniques for heat transfer and force measurements in a hypersonic shock tunnel. *Cor-*

- nell Aero. Lab., CAL Rep. AD 917-A-1*
(1956).
64. SKINNER, G. T.: A new method of calibrating thin film gauge backing materials. *Cornell Aero. Lab., CAL Rep. 105* (1962).
65. CHOW, W. L., KORST, H. H.: On the flow structure within a constant pressure compressible turbulent jet mixing region. *NASA TN D-1894* (1963).

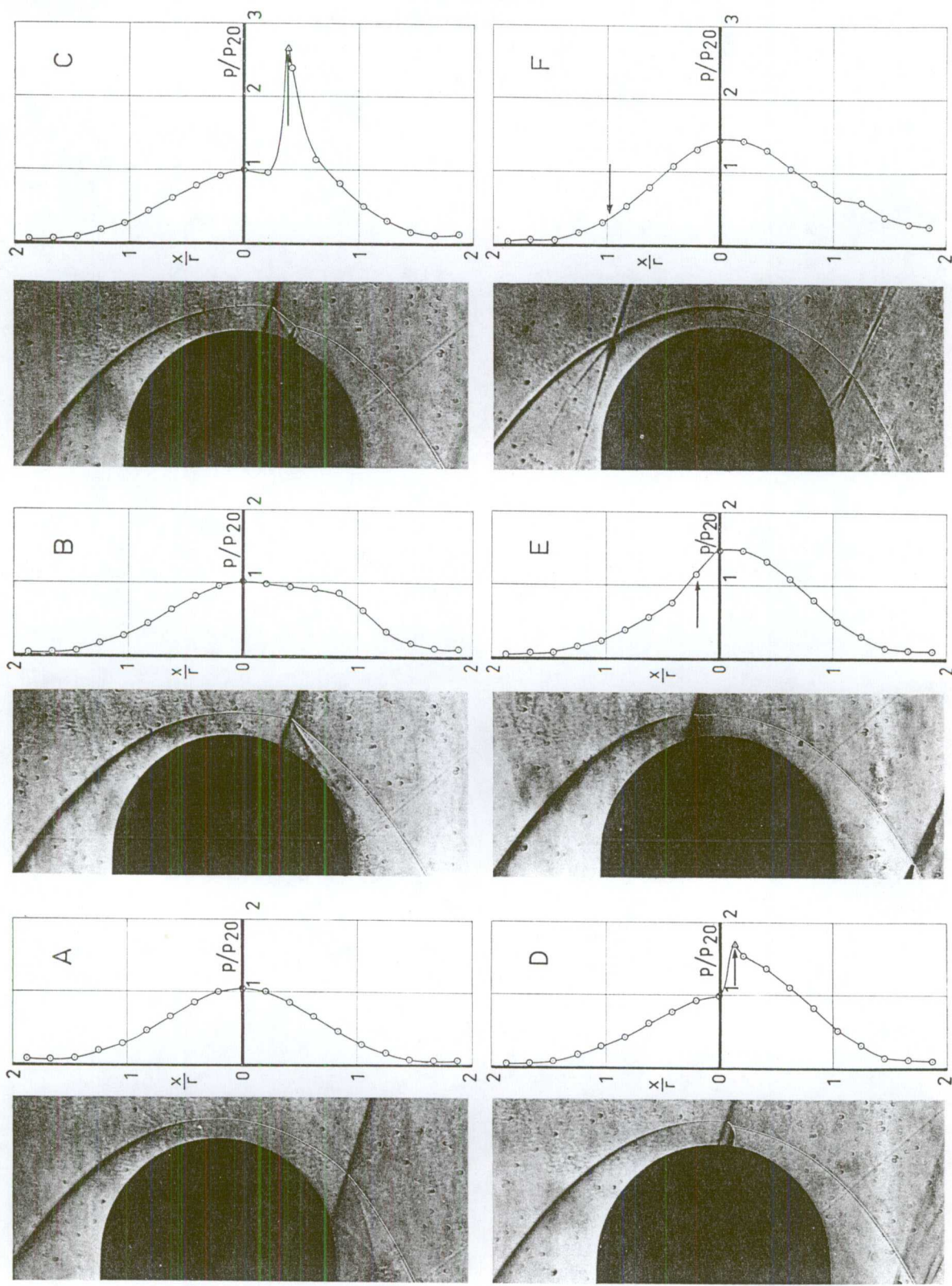


Fig. 5.2. Pressure distributions on a hemisphere, $M = 4.6$, $\xi = 5^\circ$. Arrow indicates point at which disturbance meets model surface.

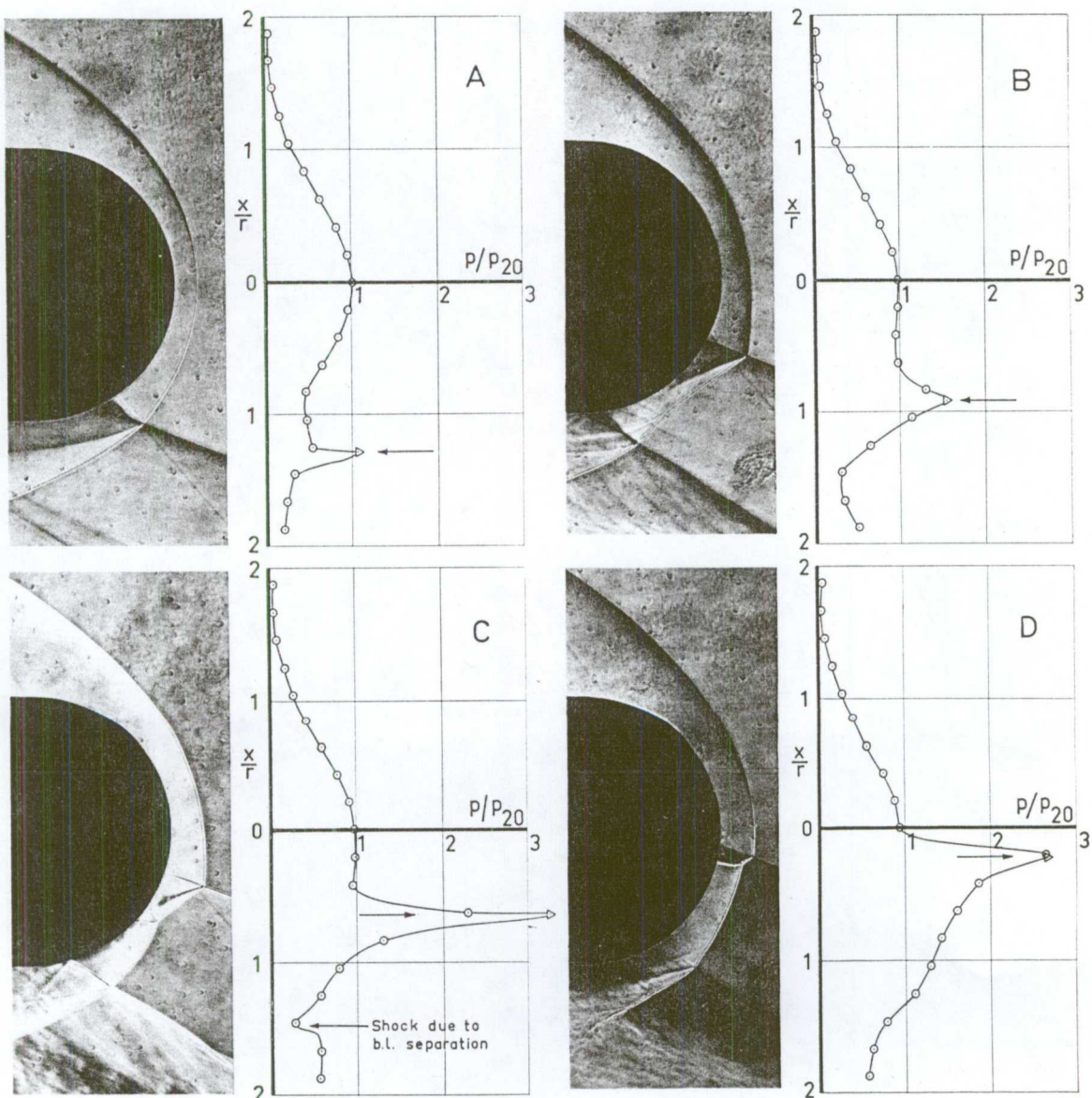


Fig. 5.3. Pressure distributions on a hemisphere. $M = 4.6$, $\xi = 10^\circ$.

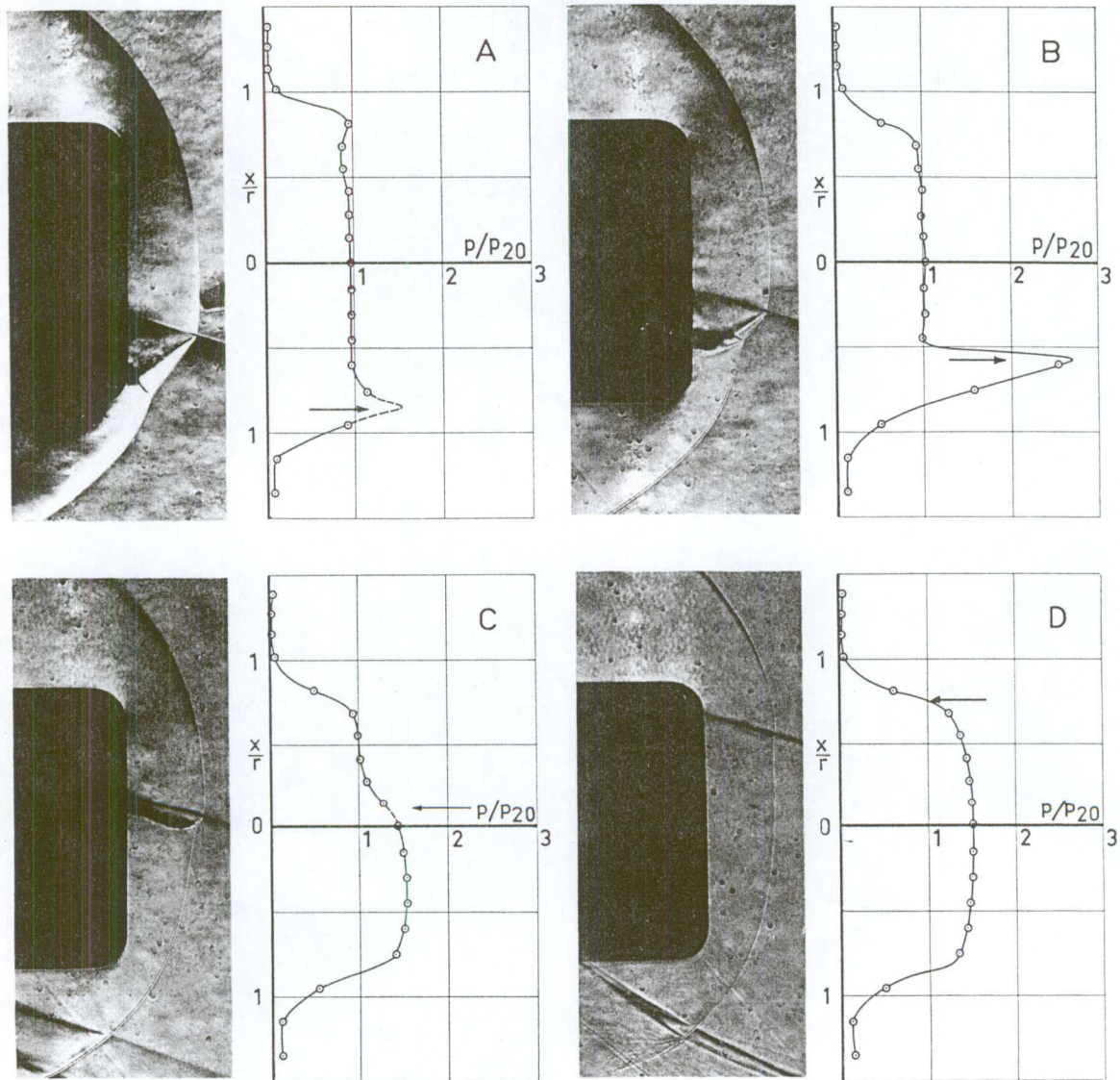


Fig. 5.4. Pressure distributions on a flat-faced cylinder. $M = 4.6$, $\xi = 5^\circ$.

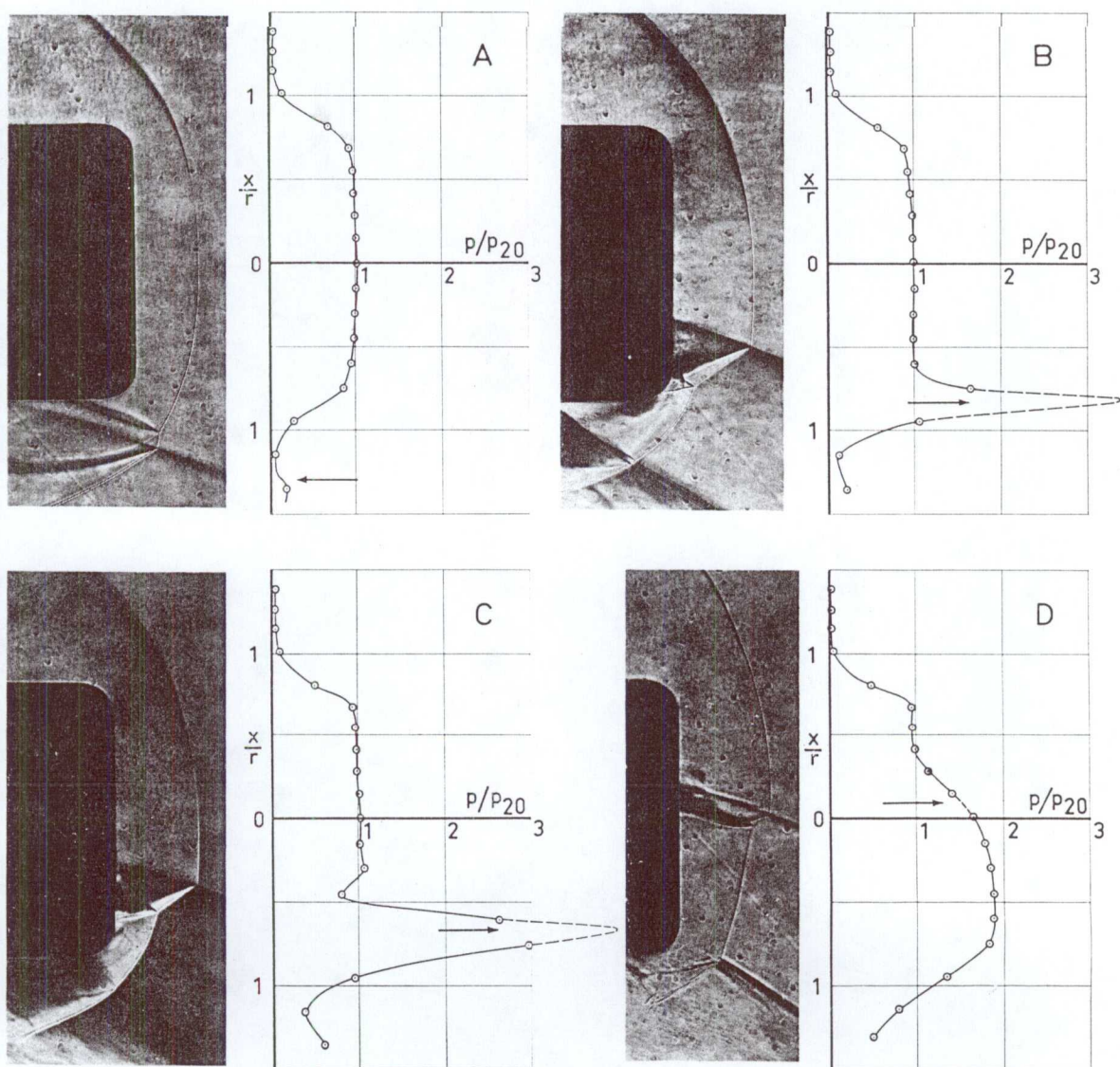


Fig. 5.5. Pressure distributions on a flat-faced cylinder. $M = 4.6$, $\xi = 10^\circ$.

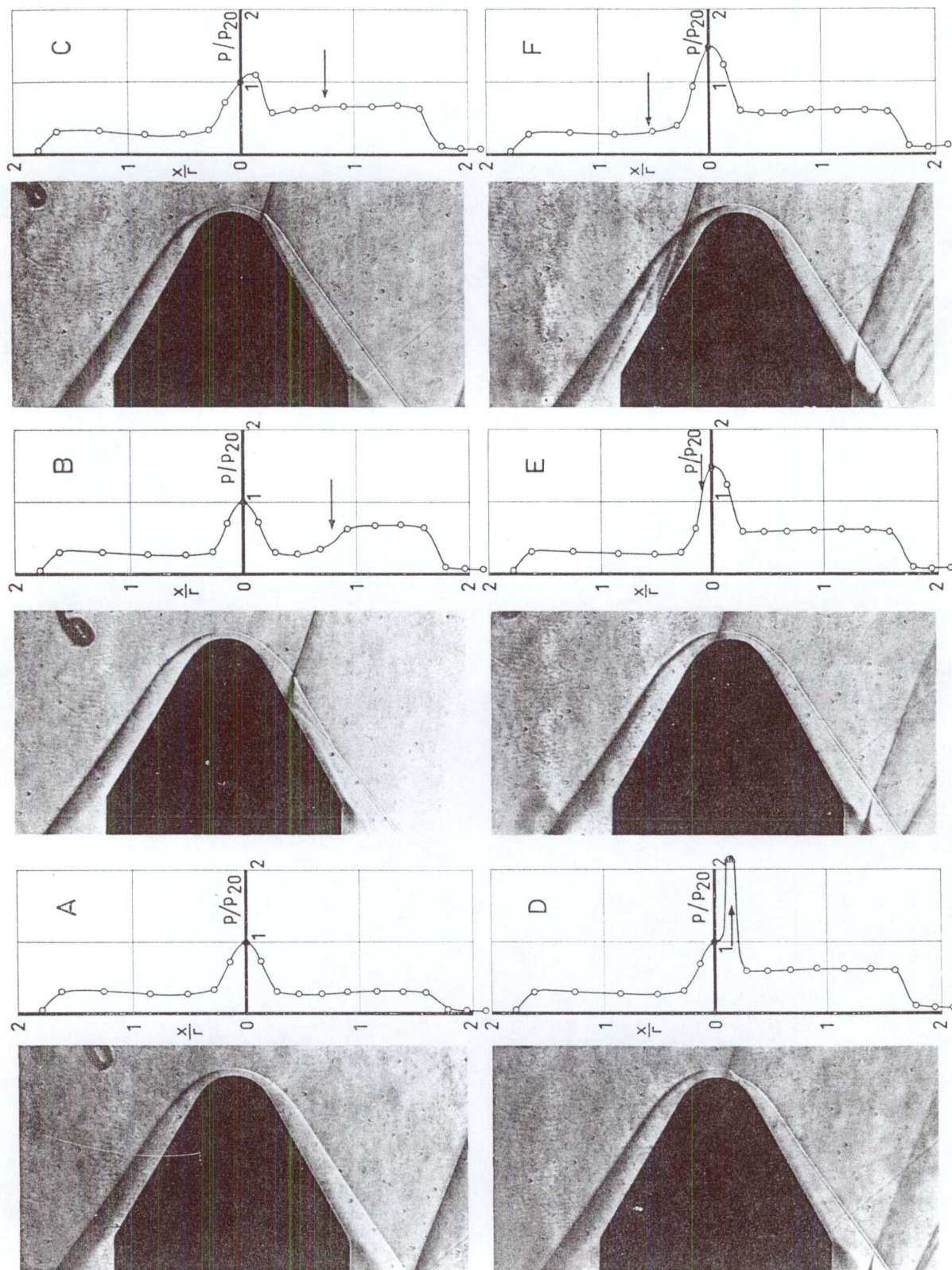


Fig. 5.6. Pressure distributions on a blunted cone. $M = 4.6$, $\xi = 5^\circ$.

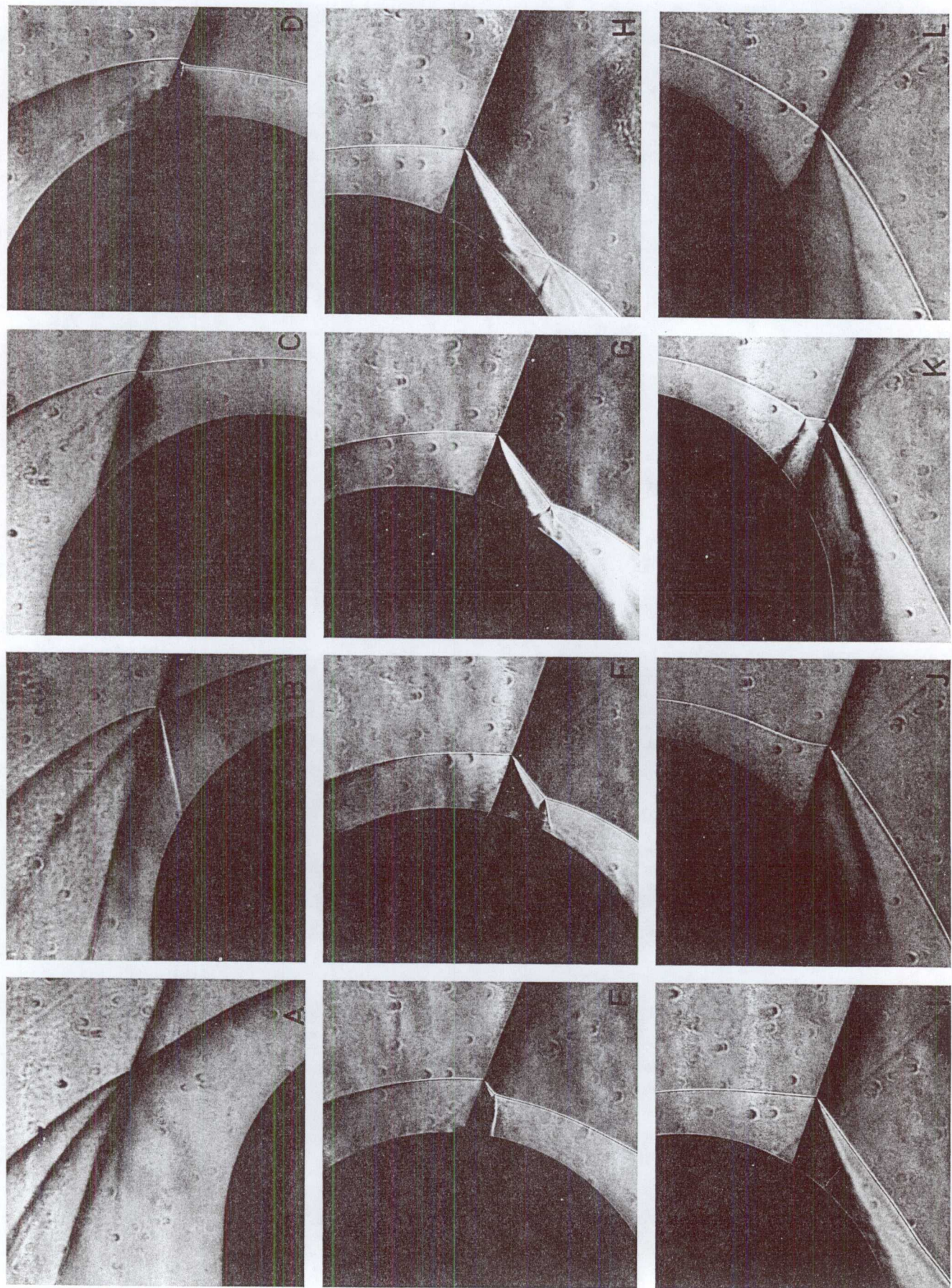


Fig. 6.1. Interference patterns on hemisphere, $M = 1.6$, $\xi = 5^\circ$.

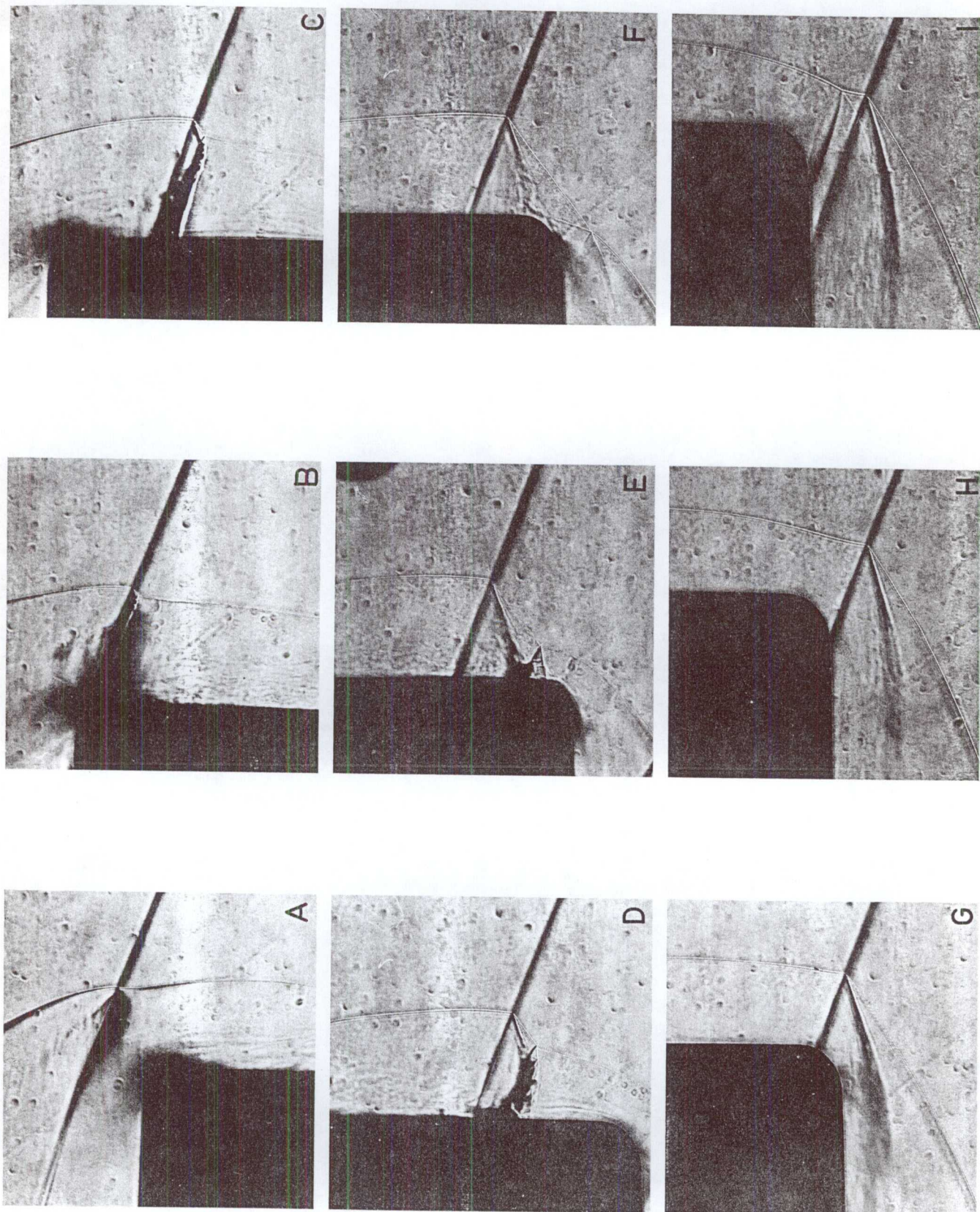


Fig. 6.2. Interference patterns on a flat-faced cylinder, $M = 4.6$, $\zeta = 5^\circ$.

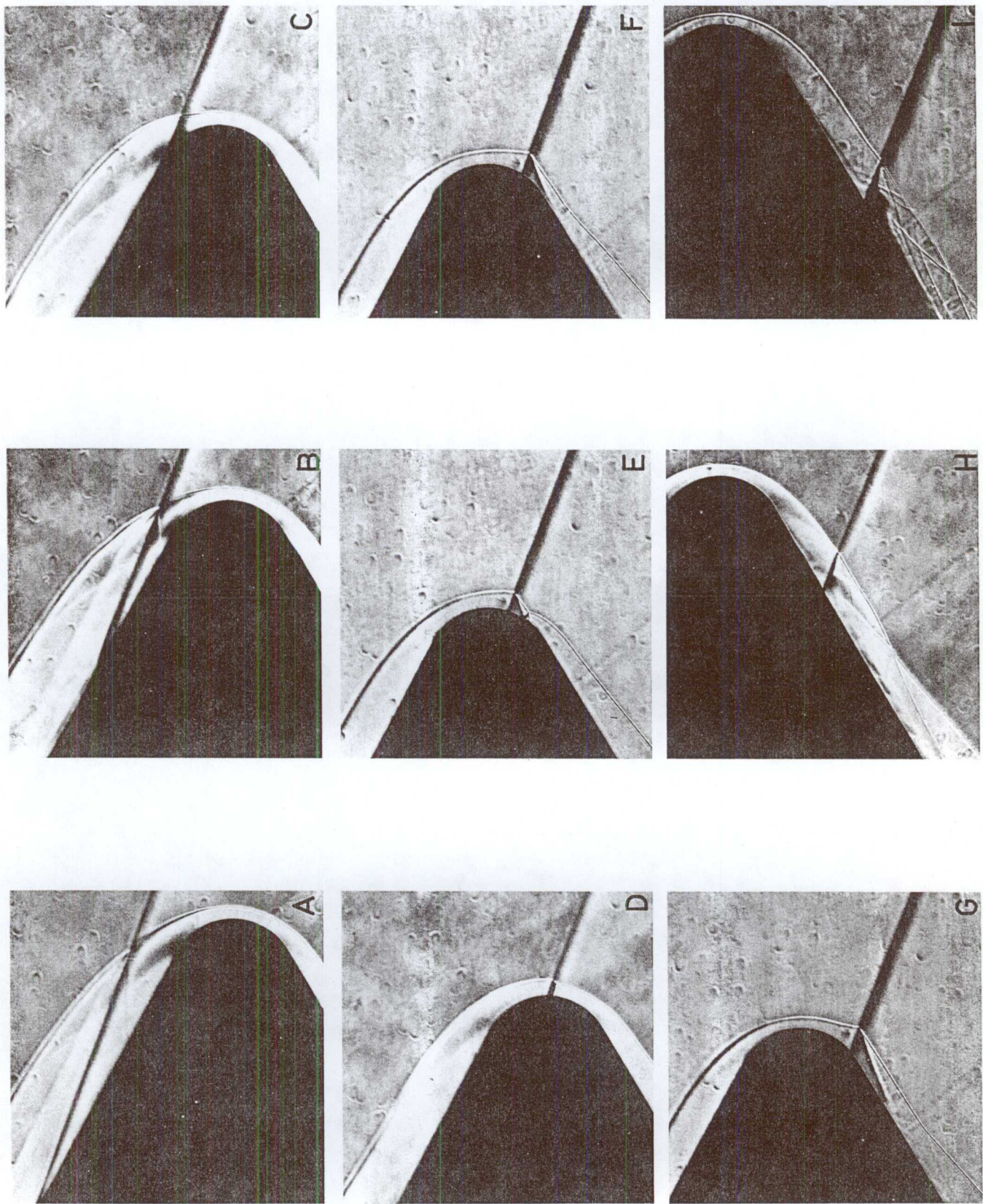


Fig. 6.3. Interference patterns on a blunted cone, $M = 4.6$, $z = 5^\circ$.

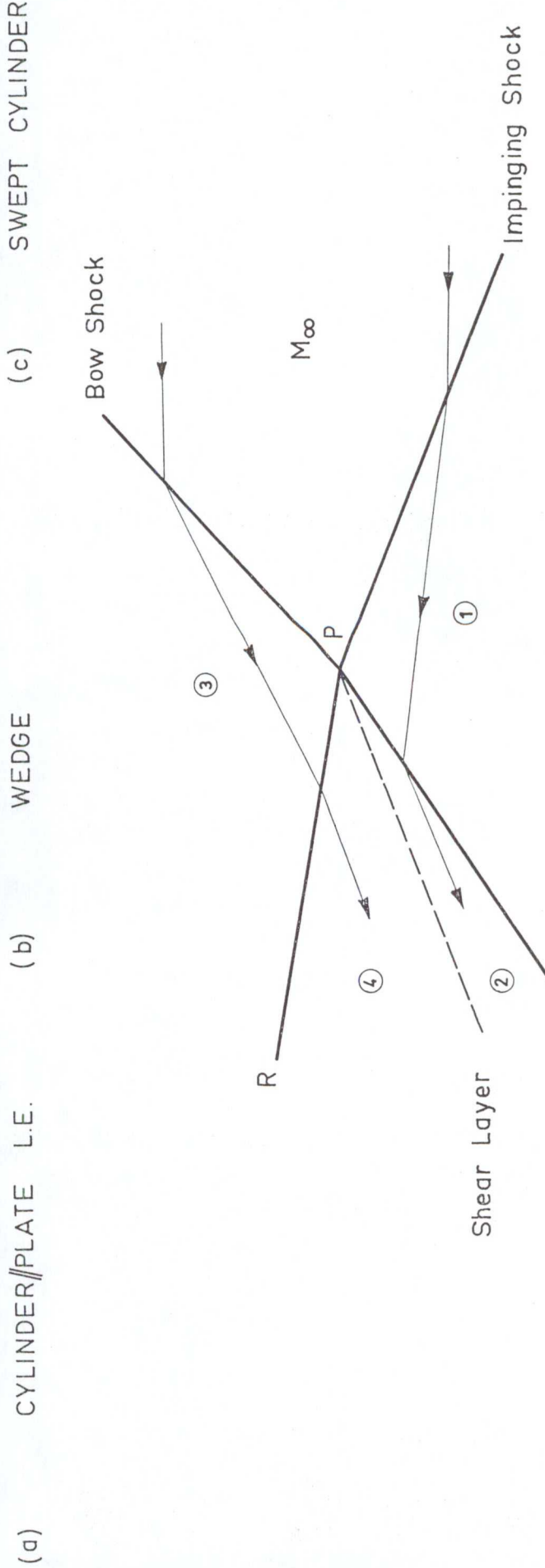
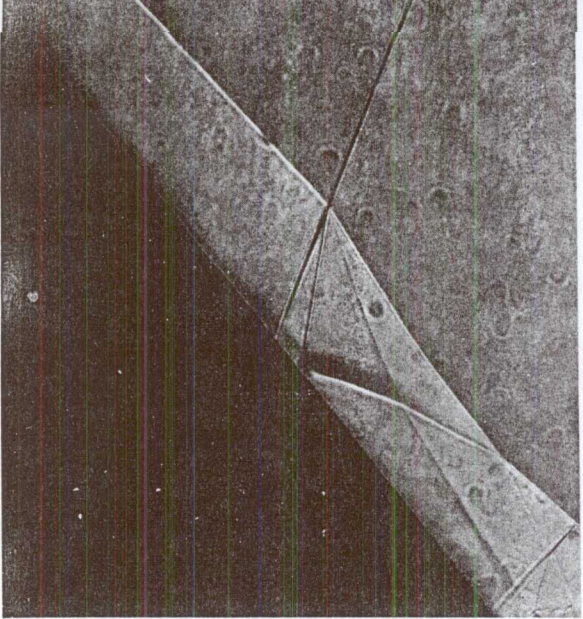
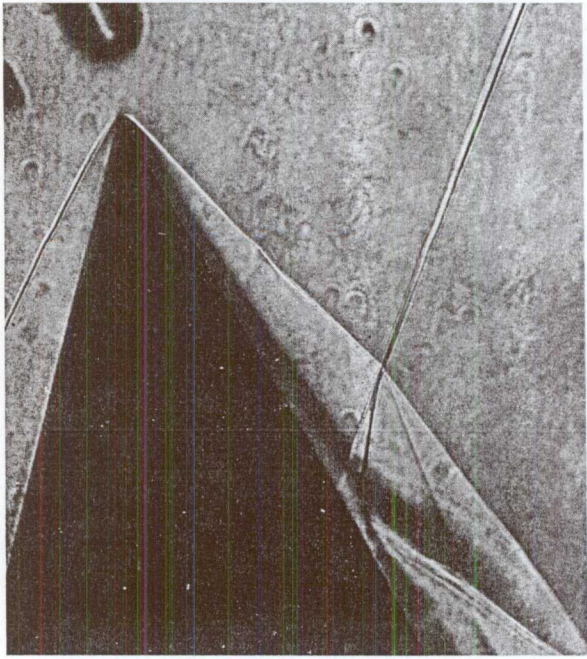
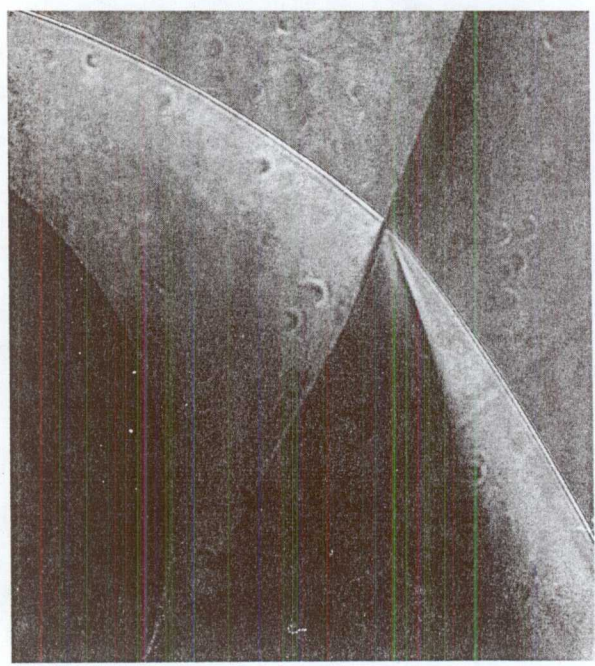


Fig. 6.1. Type I interference, $M = 4.6$, $\zeta = 10^\circ$.



(d) HEMISPHERE

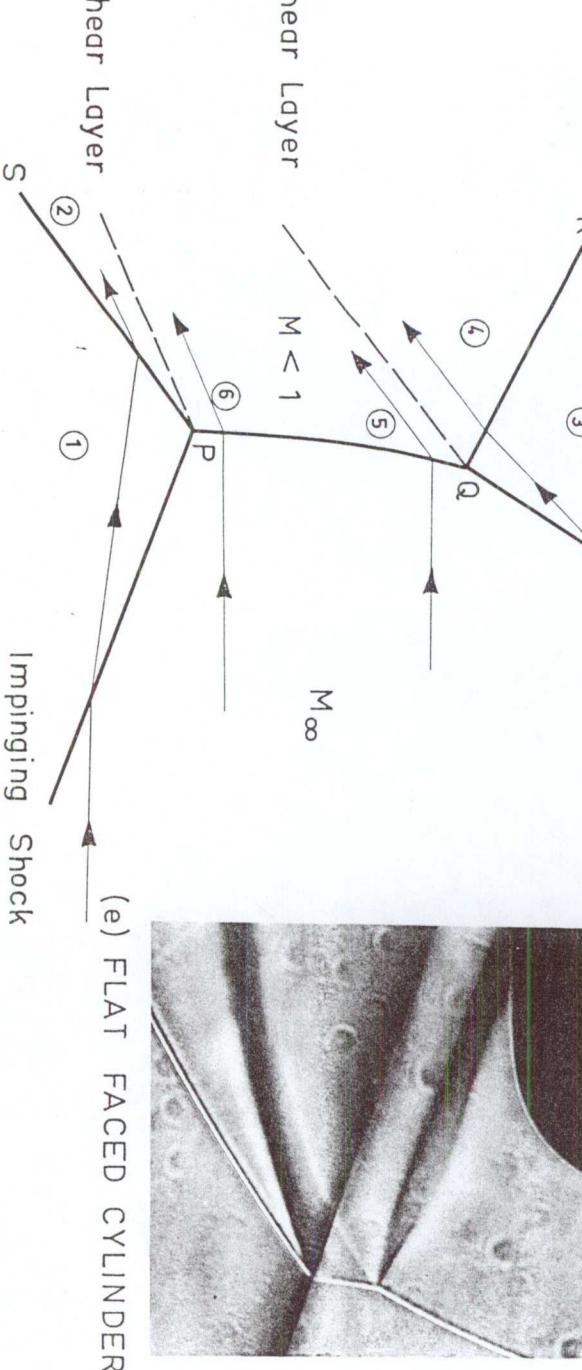
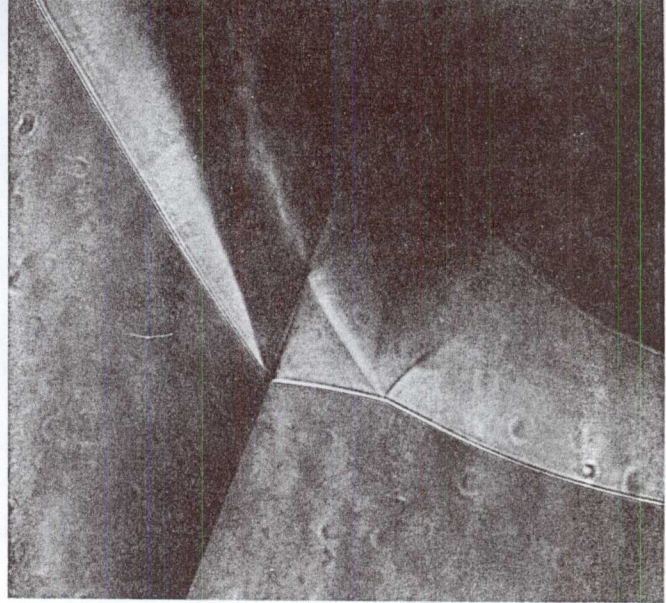


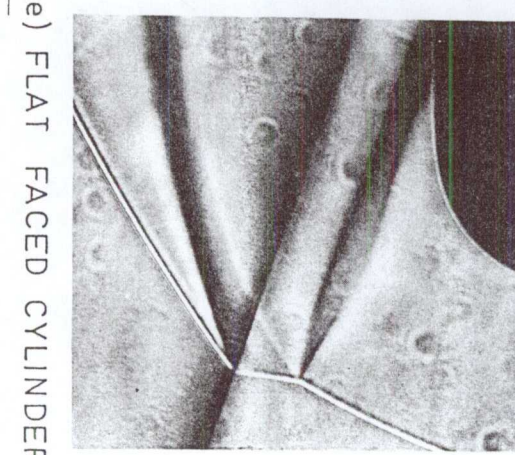
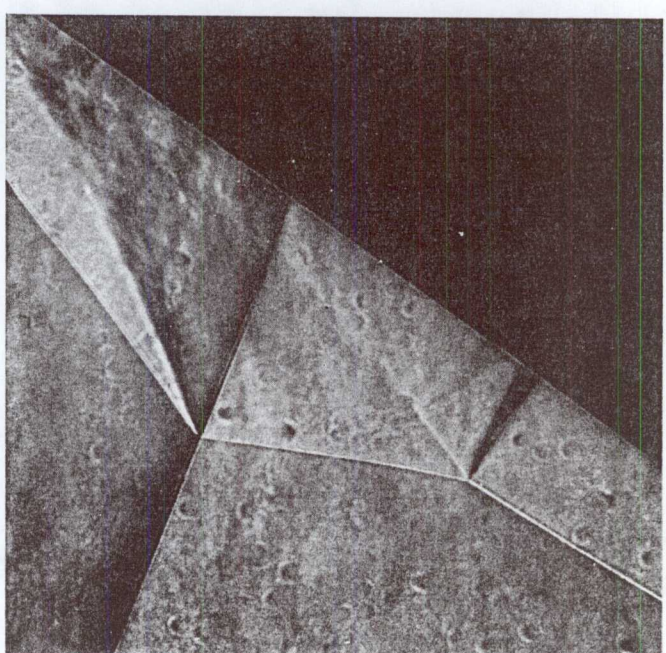
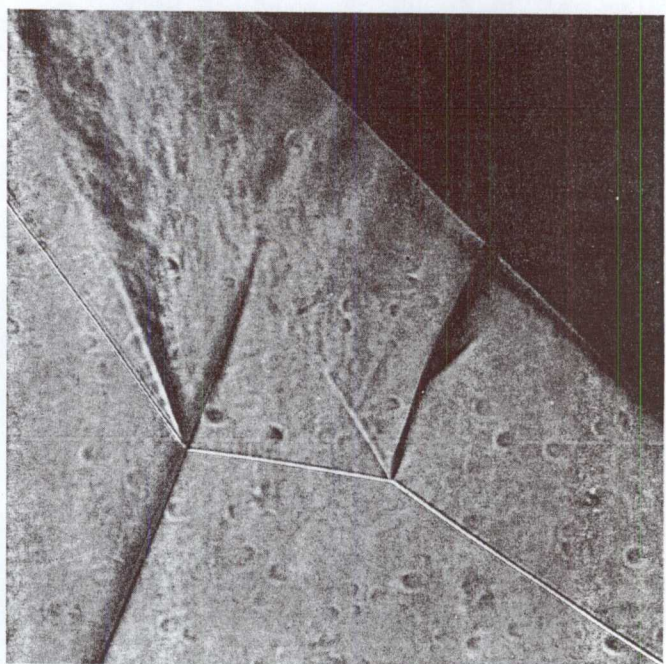
Fig. 6.6. Type II interference, $M = 1.6$, $g = 10^3$.

CYLINDER // PLATE L.E.



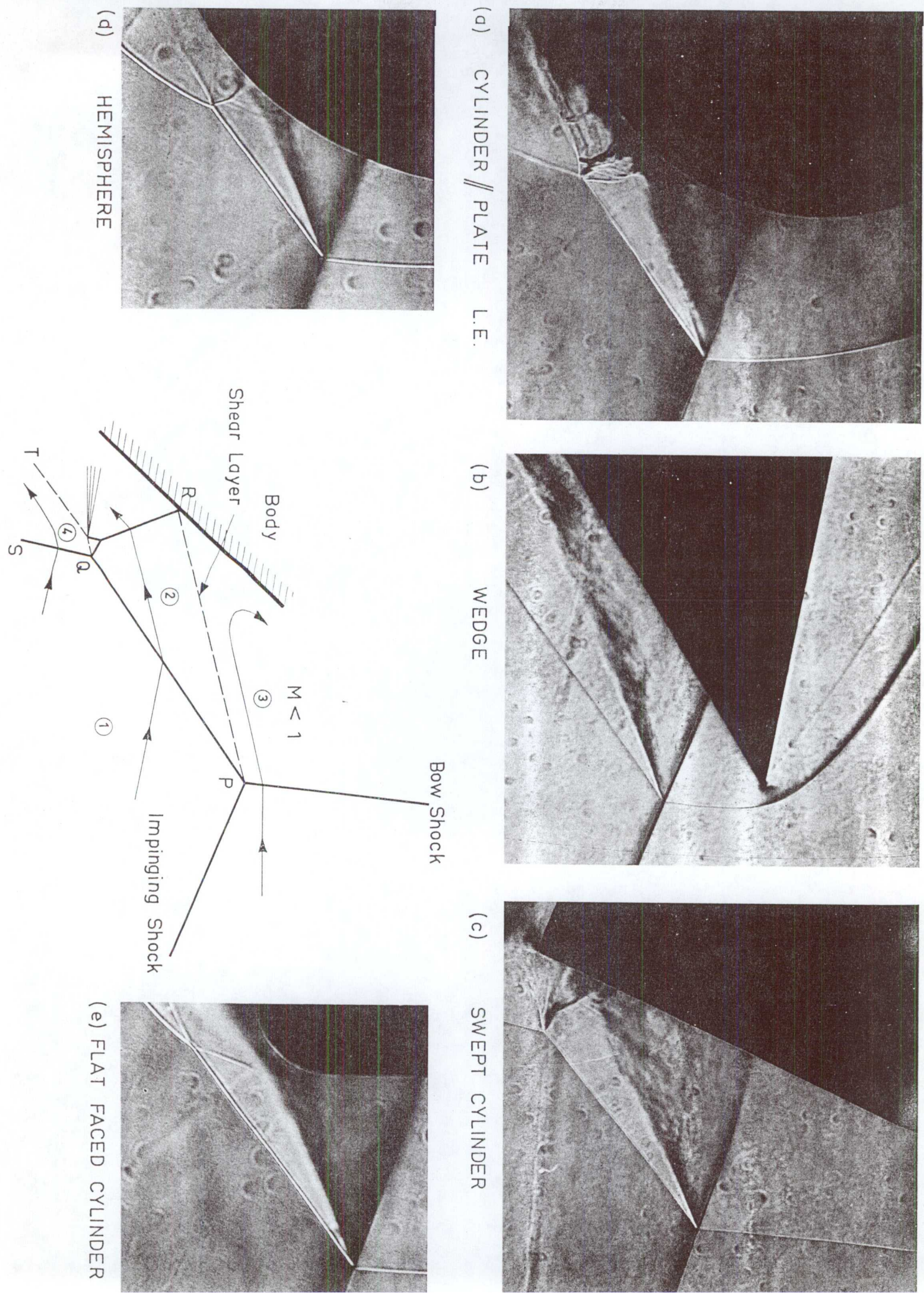
(b) WEDGE

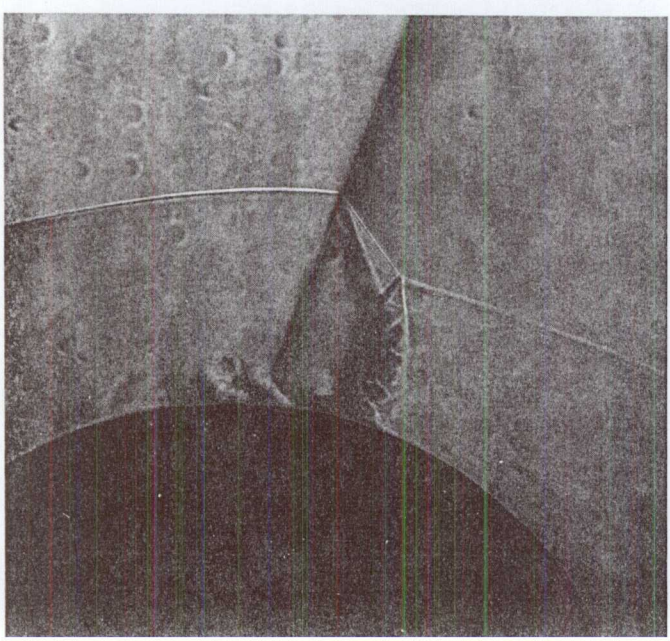
SWEPT CYLINDER



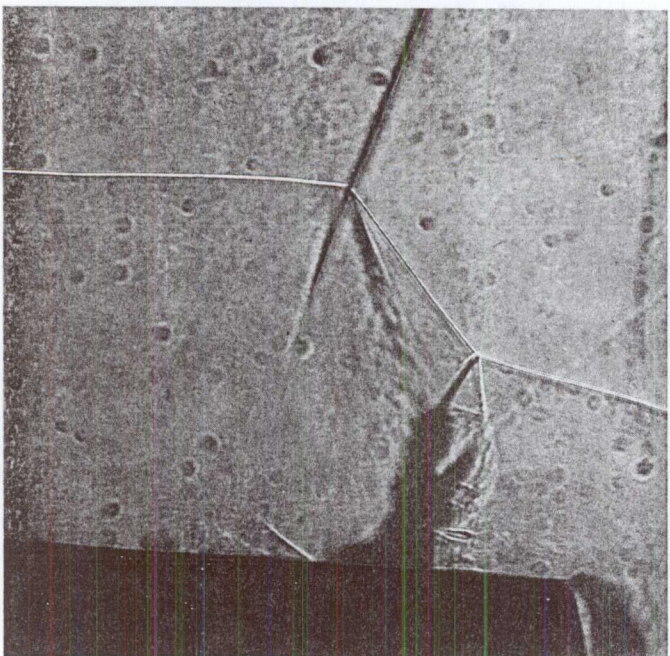
(e) FLAT FACED CYLINDER

FIG. 66. Type II interference, $M = 1.6$, $L/G = 10^4$.

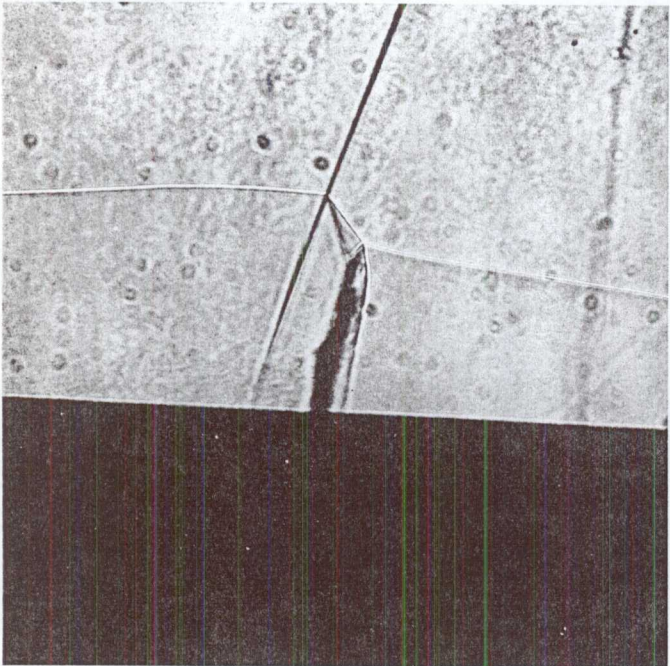




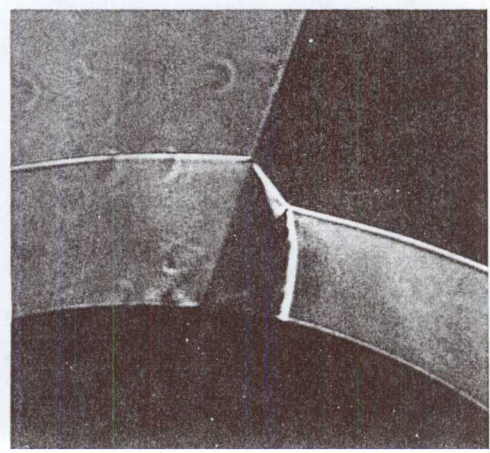
(a) CYLINDER // PLATE L.E.



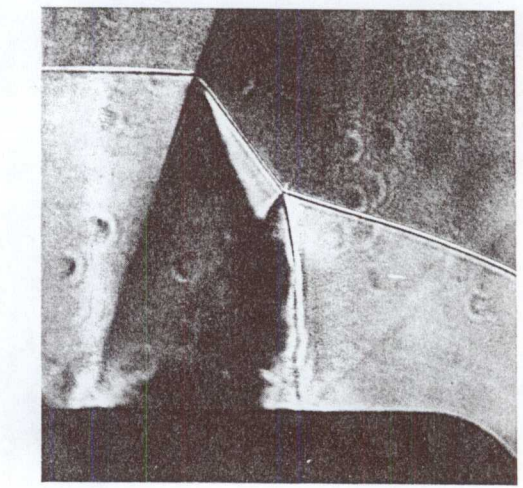
(b) CYLINDER // PLATE L.E.



(c) SWEPT CYLINDER



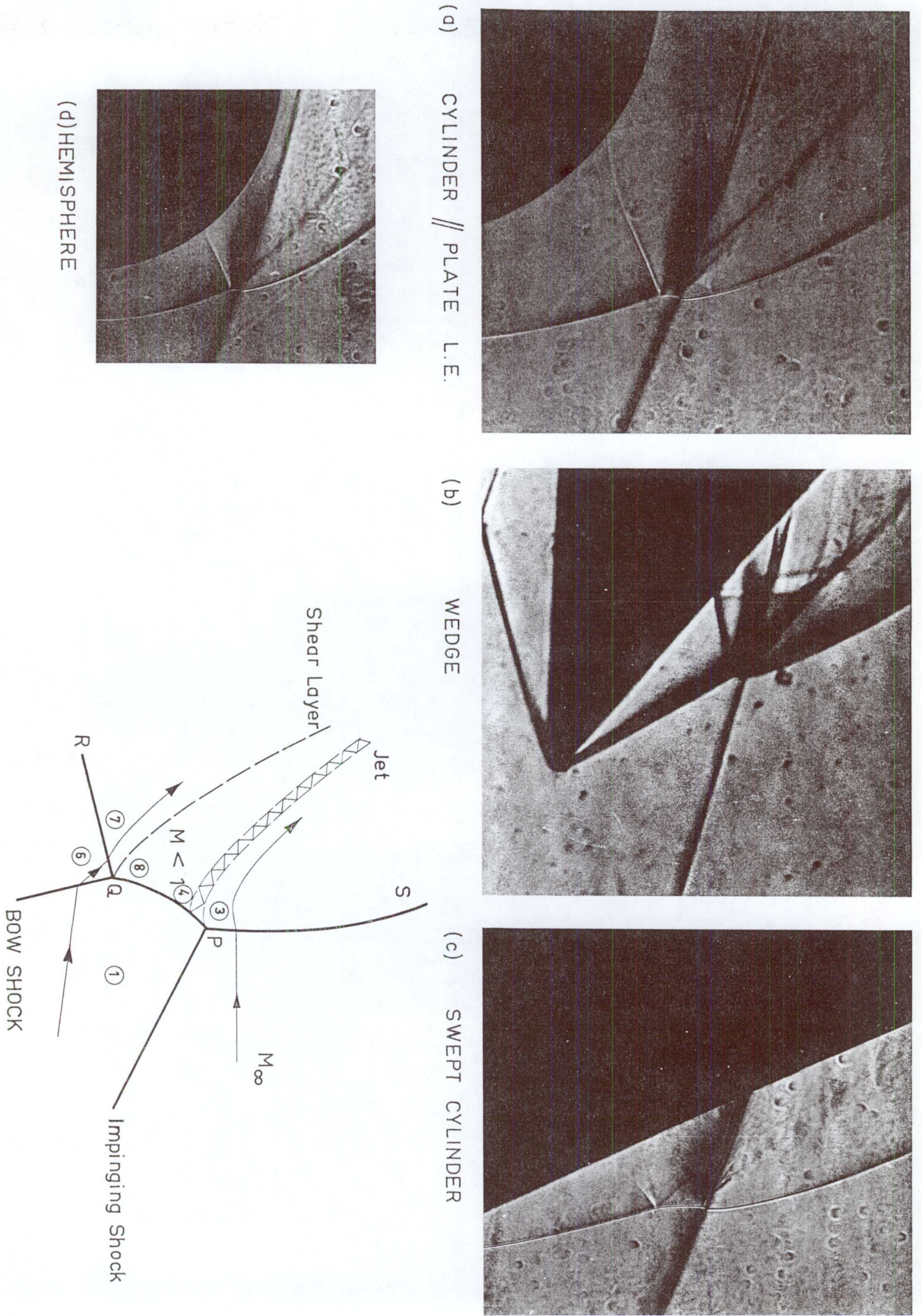
(d) HEMISPHERE

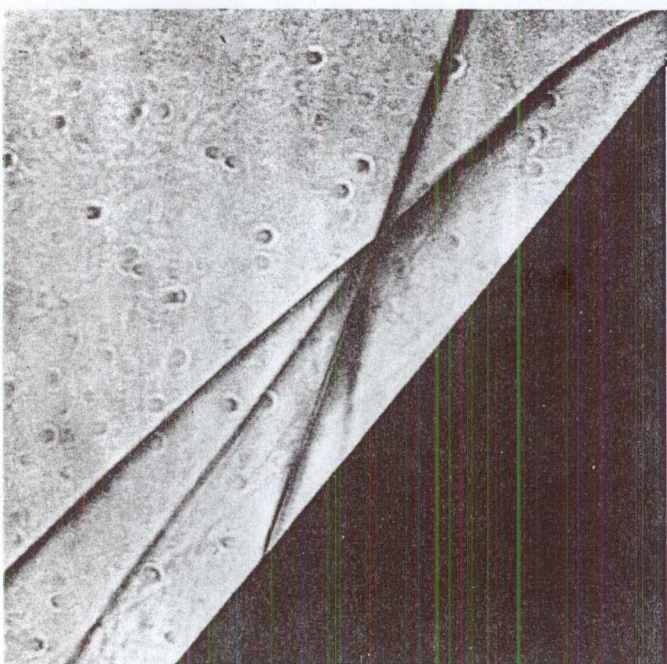


(e) FLAT FACED CYLINDER

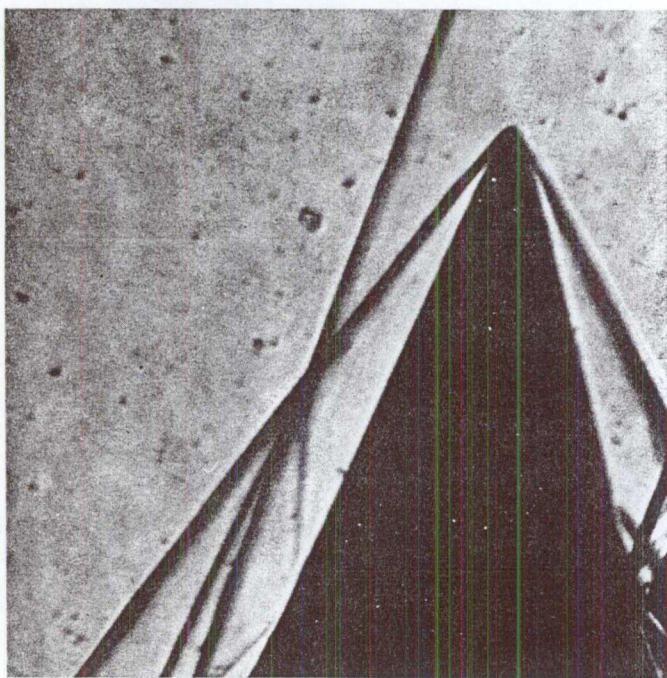
Fig. 6.11. Type IV interference. $M = 4.6$, $\xi = 10^\circ$

Fig. 6.14. Type V interference. $M = 4.6$, $\xi = 10^6$.

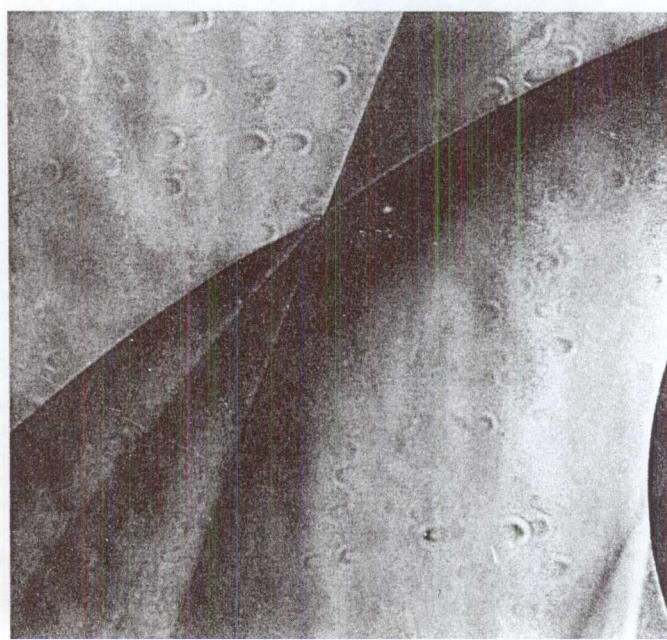




(c) SWEPT CYLINDER



(b) WEDGE



CYLINDER // PLATE L.E.

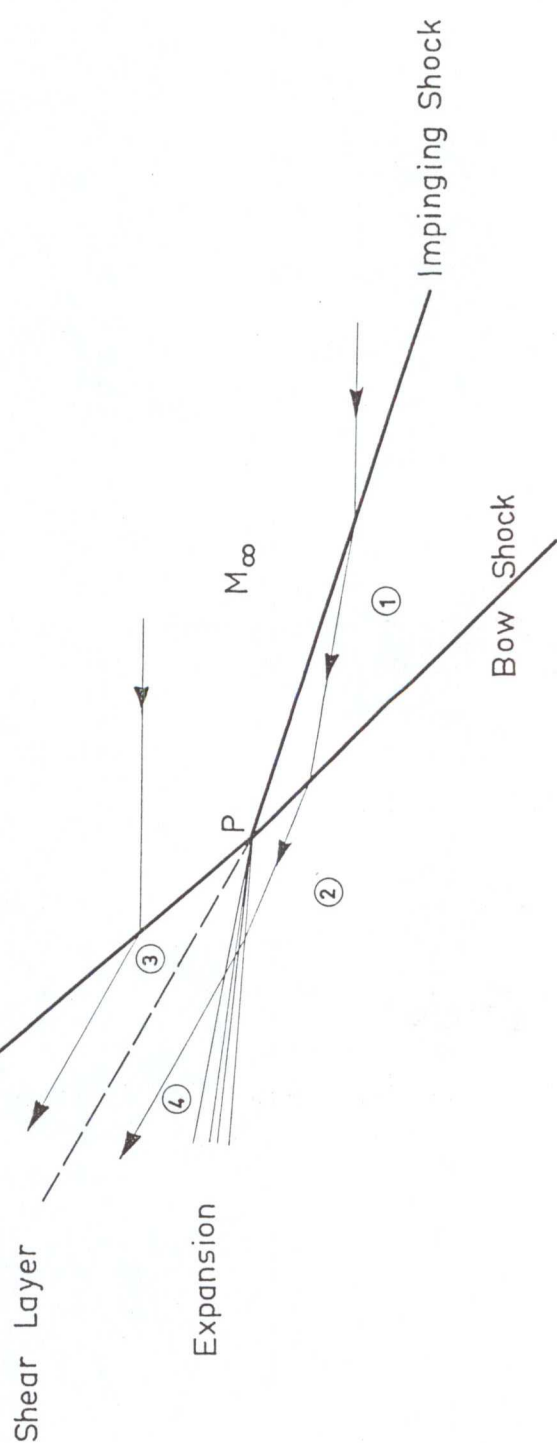


Fig. 6.16. Type VI interference. $M = 4.6$, $\xi = 10^\circ$.

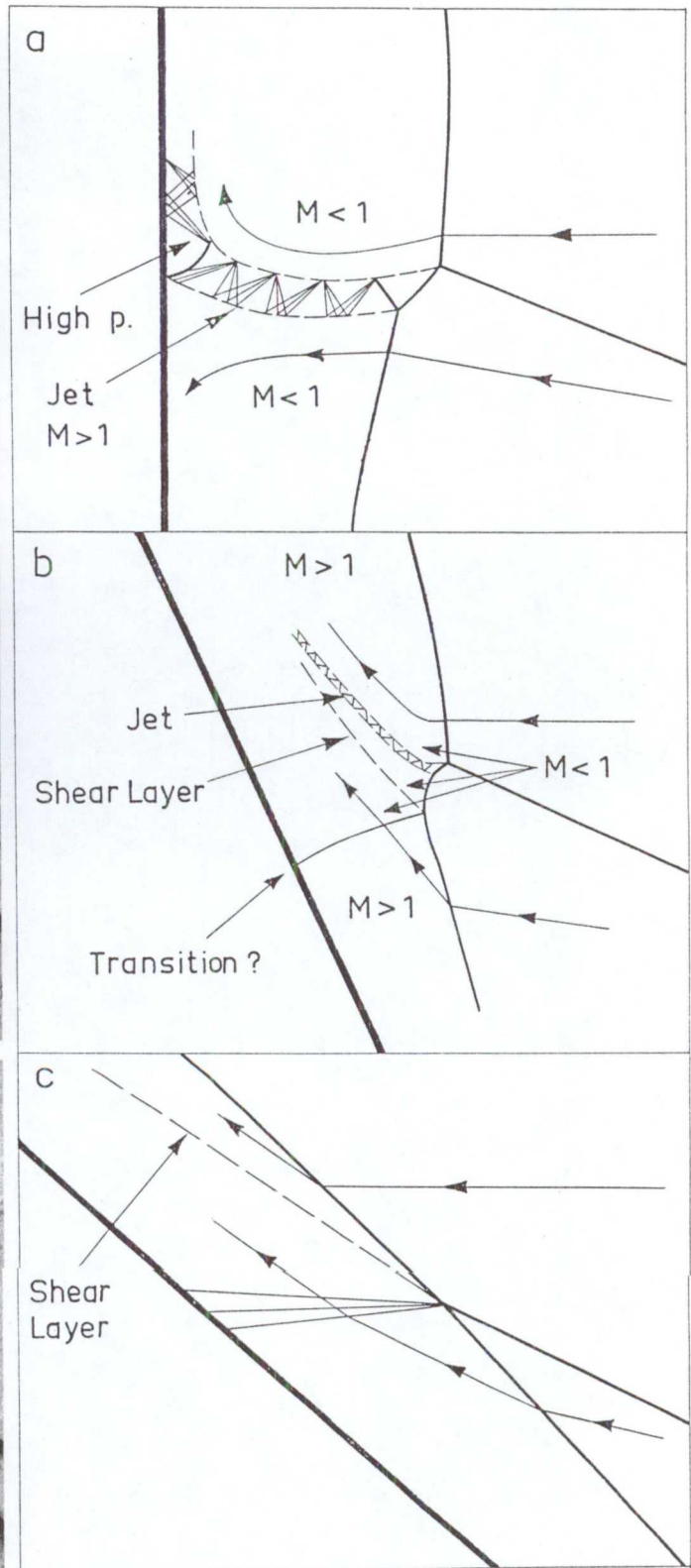
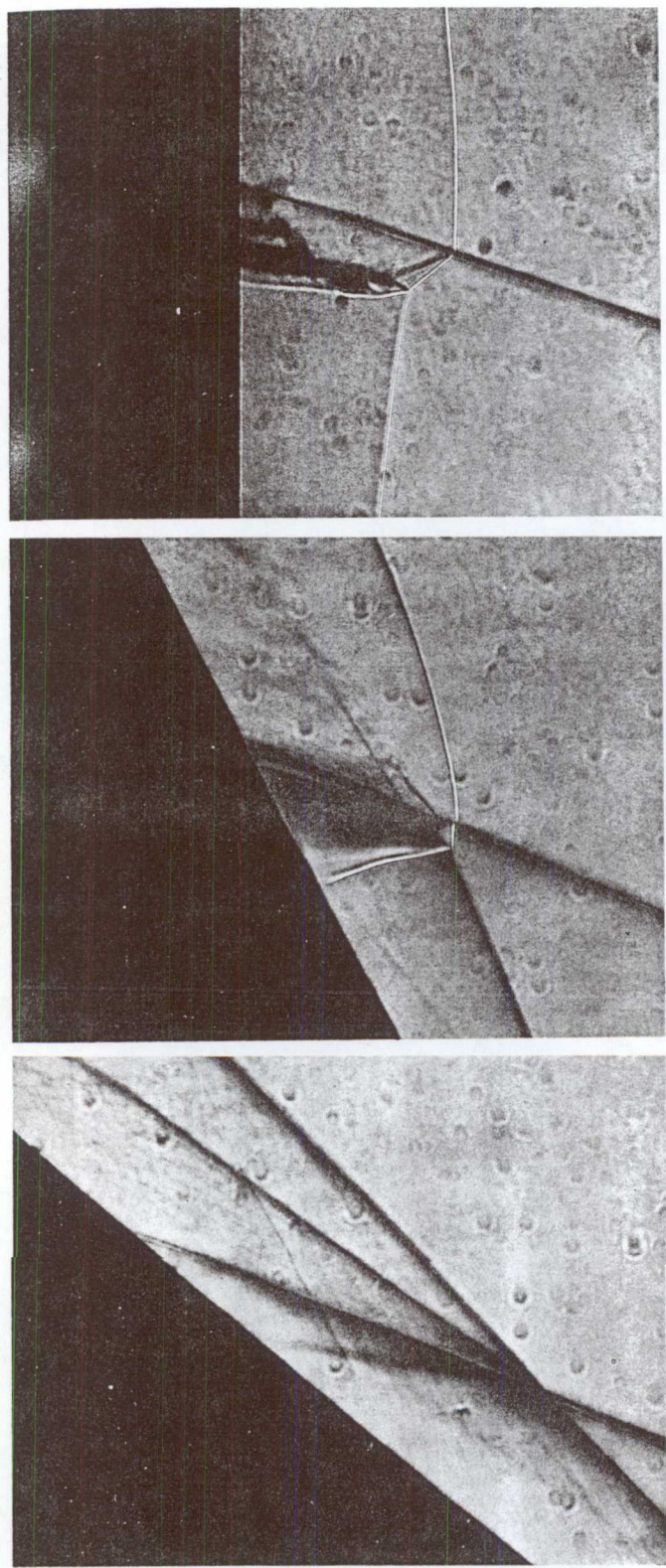


Fig. 6.18. Effect of varying sweep angle of cylindrical fin. a. Type IV interference. b. Type V interference. c. Type VI interference. $M = 4.6$, $\xi = 5^\circ$.

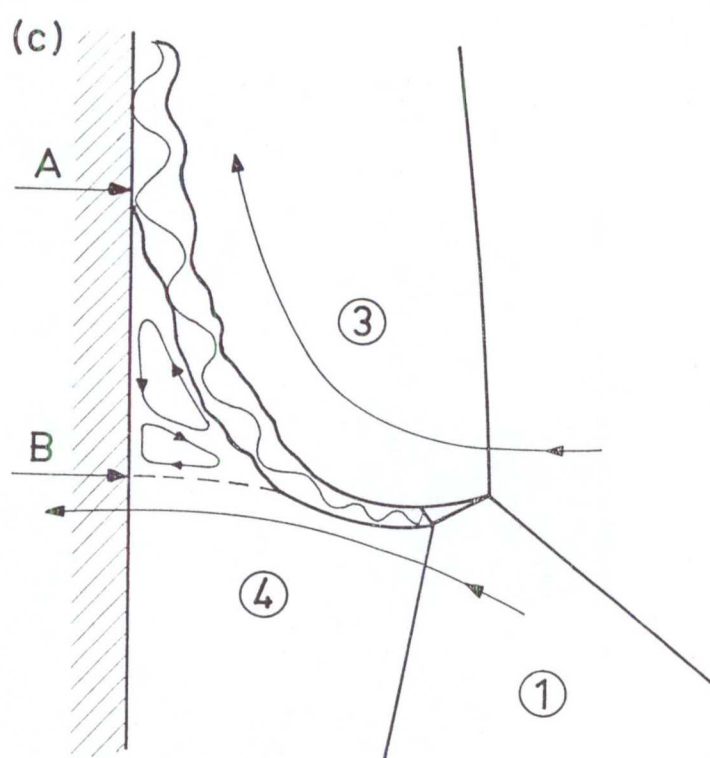
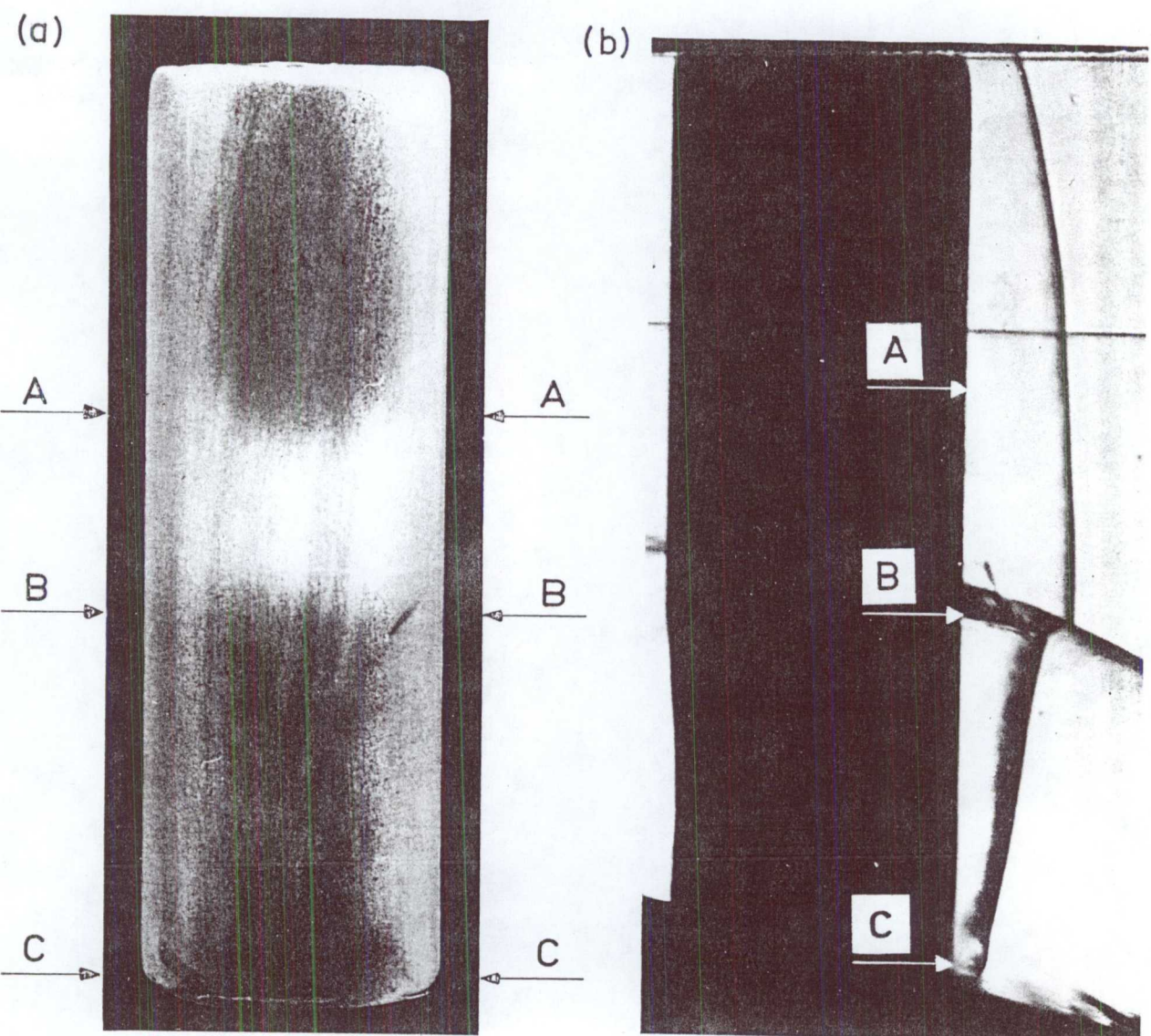


Fig. 8.12. a. Cylindrical fin coated with Detectotemp after 6 sec run at $M = 4.6$, $\xi = 15^\circ$. b. Corresponding schlieren photograph. c. Sketch of impingement region. Type IV interference.